UNIVERSITY OF RIJEKA
FACULTY OF PHYSICS

Željko Rapljenović

# Collective dynamics and correlation effects in M-type hexaferrites

DOCTORAL DISSERTATION

Rijeka, 2026.

UNIVERSITY OF RIJEKA
FACULTY OF PHYSICS

Željko Rapljenović

# Collective dynamics and correlation effects in M-type hexaferrites

DOCTORAL DISSERTATION

Supervisor: dr. sc. Tomislav Ivek
Co-supervisor: prof. dr. sc. Aleš Omerzu

Rijeka, 2026.

Mentor rada: dr.sc. Tomislav Ivek
Komentor rada: prof. dr. sc. Aleš Omerzu

Doktorski rad obranjen je dana _____ u/na _____
_____, pred povjerenstvom u sastavu:

1._____
2._____
3._____
4._____
5._____

I would like to express my gratitude to my mentor dr.sc. Tomislav Ivek and co-mentor prof. dr. sc. Aleš Omerzu for their guidance and supervision throughout this work. Their expertise and perspective have provided valuable direction during the course of my PhD, and I am thankful for their support.

For the many engaging and insightful scientific discussions, I am grateful to, in no particular order, Đuro Drobac, Mirta Herak, Matija Čulo, Silvija Tomić, Antonio Supina and Alessandro Nicolaou. Your ideas, patience, and readiness to share knowledge and most importantly discussion have enabled the existence of a finish-line.

I owe the deepest thanks to my wife and daughter. Their love, understanding, and above else patience have been the driving force for this goal.

Finally, I would like to thank all the crew from the office and everyone who felt part of it, especially, now in alphabetical order, Antonio, Blaž, Lovro and Martina. Pain metabolizes faster in company.

# Collective dynamics and correlation effects in M-type hexaferrites


## Abstract

This dissertation investigates the collective dynamics and correlation effects in single-crystalline M-type hexaferrites $Ba_xPb_{1-x}Fe_{12-y}Al_yO_{19}$, by combining macroscopic probes like AC susceptibility, dielectric spectroscopy, and DC transport with local spectroscopies like X-ray absorption (XAS) and resonant inelastic X-ray scattering (RIXS). The central finding is a robust correlation between the activation energies that govern magnetic relaxation, dielectric relaxation, and electrical transport across a controlled series of Al substitutions, revealing a shared underlying mechanism that links spin and charge dynamics. Building on these nonlocal responses, RIXS detects $Fe^{2+}$ related low-energy loss features that are not resolvable in XAS. This motivated a unified hypothesis of charged magnetic domain walls that pin to charged impurities and are progressively screened by thermally activated carriers. The hypothesis naturally explains the common activation scales and their evolution with disorder (Al). Overall, the work establishes a macroscopic correlation effect in M-type hexaferrites that spans radio-frequency relaxations to soft X-ray excitations.



**Keywords:** M-type hexaferrites, AC susceptibility, Dielectric spectroscopy, DC transport, XAS, RIXS, Charged domain walls, Activation energy.

# Kolektivna dinamika i korelacijski efekti u heksaferitima M-tipa

## Sažetak

Ova disertacija istražuje kolektivnu dinamiku i korelacijske efekte u heksaferritima M-tipa $Ba_xPb_{1-x}Fe_{12-y}Al_yO_{19}$, kombinirajući makroskopske eksperimentalne tehnike poput AC susceptibilnosti, dielektrične spektroskopije i DC transporta s lokalnim spektroskopijama poput rendgenske apsorpcijske spektroskopije (XAS) i rezonantnog neelastičnog rendgenskog raspršenja (RIXS). Glavni doprinos disertacije je robusna korelacija između aktivacijskih energija koje upravljaju magnetskom relaksacijom, dielektričnom relaksacijom i električnim transportom kroz seriju Al-supstitucija, što otkriva zajednički temeljni mehanizam koji povezuje dinamiku spina i naboja. Nadovezujući se na te nelokalne odazive, RIXS detektira niskoenergijska raspršenja povezana s $Fe^{2+}$ koje se u XAS-u ne mogu razlučiti. Navedena fenomenologija motivira hipotezu o nabijenim magnetskim domenskim zidovima koji zapinju na nabijene nečistoće i postupno se zasjenjuju termički aktiviranim nosiocima. Hipoteza objašnjava zajedničke aktivacijske energije i njihov razvoj s unosom nereda (Al). Ovaj rad predstavlja makroskopske korelacijske efekte u heksaferritima M-tipa, čiji zapis je vidljiv u radiofrekvencijskim relaksacijama i pobudama u spektru rendgenskih zraka.

**Ključne riječi:** Heksaferiti M-tipa, AC susceptibilnost, Dielektrična spektroskopija, DC transport, XAS, RIXS, Nabijeni domenski zidovi, Aktivacijska energija.

# Research and publications related to this thesis

The main part of the research presented in this thesis has been published in the following peer-reviewed article, in which I am the first author:

- **Ž. Rapljenović**, N. Novosel, D. Dominko, V. Kisiček, D. R. Góngora, Đ. Drobac, M. Prester, D. Vinnik, L. N. Alyabyeva, B. P. Gorshunov, and T. Ivek, "Persisting correlation between electrical transport and magnetic dynamics in M-type hexaferrites," *Journal of Alloys and Compounds* **895**, 162660 (2022), doi:10.1016/j.jallcom.2021.162660.

  This publication contains results directly related to the core topic of this thesis, namely the correlation between electrical transport, dielectric response, and magnetic dynamics in M-type hexaferrites.

Additional data on X-ray absorption and Resonant inelastic x-ray scattering presented in the thesis are currently unpublished.

In addition, I have co-authored the following publications, which are relevant to the present thesis through their scientific context, methodology, or experimental techniques:

- M. Dragičević, D. Rivas Góngora, **Ž. Rapljenović**, M. Herak, V. Brusar, D. Altus, M. Pregelj, A. Zorko, H. Berger, D. Arčon, and T. Ivek, "Control of a polar order via magnetic field in a vector-chiral magnet," *Physical Review B* **104**, L121107 (2021), doi:10.1103/PhysRevB.104.L121107.

  Relevance: related to multiferroic and magnetoelectric phenomena in magnetic oxide systems, which form an important broader context for this thesis.

- V. Kisiček, D. Dominko, M. Ćulo, **Ž. Rapljenović**, M. Kuveždić, M. Dragičević, H. Berger, X. Rocquefelte, M. Herak, and T. Ivek, "Spin-Reorientation-Driven Linear Magnetoelectric Effect in Topological Antiferromagnet $Cu_3TeO_6$," *Physical Review Letters* **132**, 096701 (2024), doi:10.1103/PhysRevLett.132.096701.

  Relevance: connected to magnetoelectric coupling in magnetic materials and therefore relevant to the wider scientific framework of this dissertation.

- J. Vukašinović, **Ž. Rapljenović**, M. Počuča-Nešić, T. Ivek, Z. Branković, and G. Branković, "The crucial role of defect structure in understanding the electrical properties of spark plasma sintered antimony doped barium stannate," *Materials Research Express* **10**, 015901 (2023), doi:10.1088/2053-1591/acb3b0.

  Relevance: related to defect-controlled electrical transport, which is conceptually relevant to the discussion of defects and pinning effects in this thesis.

- J. Vukašinović, M. Počuča-Nešić, D. Luković Golić, V. Ribić, Z. Branković, S. M. Savić, A. Dapčević, S. Bernik, M. Podlogar, M. Kocen, **Ž. Rapljenović**, T. Ivek, V. Lazović, B. Dojčinović, and G. Branković, "The structural, electrical and optical properties of spark plasma sintered $BaSn_{1-x}Sb_xO_3$ ceramics," *Journal of the European Ceramic Society* **40**, 5566–5575 (2020), doi:10.1016/j.jeurceramsoc.2020.06.062.

  Relevance: relevant through electrical characterization of oxide materials and analysis of transport-related properties.

- K. Juraić, D. Gracin, M. Ćulo, **Ž. Rapljenović**, J. R. Plaisier, A. Hodzic, Z. Siketić, L. Pavić, and M. Bohač, "Origin of Magnetotransport Properties in APCVD Deposited Tin Oxide Thin Films," *Materials* **13**, 5182 (2020), doi:10.3390/ma13225182.

  Relevance: related to transport and magnetotransport studies, which are methodologically close to parts of the present work.

- M. Pinterić, D. Rivas Góngora, **Ž. Rapljenović**, T. Ivek, M. Ćulo, B. Korin-Hamzić, O. Milat, B. Gumhalter, P. Lazić, et al., "Electrodynamics in Organic Dimer Insulators Close to Mott Critical Point," *Crystals* **8**, 190 (2018), doi:10.3390/cryst8050190.

  Relevance: relevant primarily through the use of electrical and dielectric measurements and data analysis techniques related to those employed in this thesis.

# Contents

# Introduction

Magnetism has been a fascinating natural phenomenon for centuries, attracting the attention of scientists and laypeople alike. It is not uncommon for theses or articles on magnetism to begin with a historical note on the discovery of lodestone and its use as a compass by ancient mariners. This thesis is no different, as it is important to appreciate the historical context of magnetism and the role it played in early human exploration and navigation. It could be said that the scientific study of magnetism began in the 19th century with the discovery of the relationship between electricity and magnetism, leading to the development of electromagnetism and the creation of many modern technological devices that rely on this phenomenon. Nonetheless, even today, the use of magnets continues to fascinate and inspire us in various ways, from the simple magnetic toys that entertain children to the complex magnetic fields that power our machines and devices. Among magnetic materials, hexaferrites are special. They exhibit a rich spectrum of magnetic structures and are indispensable in industrial applications ranging from permanent magnets to microwave devices [1].

In parallel with the study of magnetism, ferroelectricity has emerged as another fundamental phenomenon in condensed matter physics. Ferroelectric materials exhibit a spontaneous electric polarization that can be reversed by an external electric field, a property that underlies their importance in modern technologies such as nonvolatile memories, sensors, actuators, capacitors, and energy-harvesting devices. Of particular interest are systems in which electric and magnetic degrees of freedom are coupled. This magnetoelectric coupling enables the mutual control of magnetic and electric properties and is therefore not only of fundamental scientific relevance but also of technological interest for future multifunctional and low-power electronic devices. In materials where magnetic and ferroelectric order coexist, commonly referred to as multiferroics, such coupling can give rise to particularly rich physical behaviour [2–6].

To understand the scope and contribution of this thesis, it is important to define the central research question: Can magnetoelectric coupling be observed in hexaferrite single crystals? This initial question of the thesis evolved in response to experimental data that suggest a previously unreported macroscopic effect. It means that the original contribution of this thesis lies in the experimental observation of a macroscopic effect in hexaferrites that, to our knowledge, has not been

previously reported. This effect, which emerged unexpectedly during the investigation of magnetoelectric coupling, opens new directions for the study of complex magnetic interactions in hexaferrites and similar systems.

For this thesis, samples of $Ba_xPb_{1-x}Fe_{12-y}Al_yO_{19}$ were selected. The primary motivation for this choice is the isovalent substitution of Al, which, being non-magnetic, progressively disrupts the magnetic order of the system. Furthermore, several studies suggest that the presence of Al may induce a ferroelectric state in this material. In addition, Pb may act as a source of $Fe^{2+}$ ions, which will be important for the later discussion [7, 8].

**Structure of the Thesis**:

- **Chapter 1 – Theoretical background**
  Fundamental concepts needed to grasp both the intrinsic behaviour of magnetic materials and the experimental techniques employed throughout the thesis.

- **Chapter 2 – Hexagonal ferrites**
  A description of crystal chemistry, magnetic properties and prior research on hexaferrites, followed by details of the synthesis and characterization of the crystals investigated.

- **Chapter 3 – Experimental techniques**
  Description of the instrumentation and measurement protocols, with emphasis on the specific physical phenomena each technique probes.

- **Chapter 4 – Results**
  Presentation of the experimental data.

- **Chapter 5 – Discussion**
  Analysis of the results that introduces a new macroscopic effect in hexaferrites and an assessment of its broader implications.

- **Chapter A – Additional measurement**
  Additional measurements that, while are not directly connected to the central hypothesis, may guide future investigations.

In summary, this thesis aims not only to elucidate an intriguing magnetic phenomenon but also to serve as a guide for forthcoming experimental work on complex ferrite systems.

# Chapter 1

# Theoretical background

This chapter aims to provide an overview of magnetic interactions, with an emphasis on their fundamental mechanisms, manifestations, and the physical models that describe them. The primary focus is on the theoretical aspects behind these interactions, such as the nature of magnetic ordering, exchange mechanisms, domain dynamics, and the associated effects. Starting with foundations, including different types of magnetic order (ferromagnetic, antiferromagnetic, and ferrimagnetic), the chapter discusses the quantum mechanical origin of magnetism, emphasizing the Heisenberg exchange interaction and its extensions, such as superexchange and other exchange mechanisms. Weiss model of antiferromagnetic order is added due to it's specificity in the explanation of particular set of results.

The chapter also delves into magnetic domains and domain walls. A dedicated section addresses domain wall motion and phenomena like the Barkhausen effect. Furthermore, concepts related to spin-lattice interactions and relaxation mechanisms are explored, laying the groundwork for understanding material responses to external fields.

Complementing the discussion of magnetic phenomena, the chapter introduces ferroelectricity as a related topic, focusing on the coupling between electric and magnetic orders, which leads to the magnetoelectric effect. Different theoretical models, including phenomenological relaxation frameworks and crystal field theory, are presented for the basis of experimental data discussion.

While this chapter establishes the theoretical framework, it should be noted that additional theoretical considerations specific to the experiments conducted will be incorporated in the corresponding experimental sections.

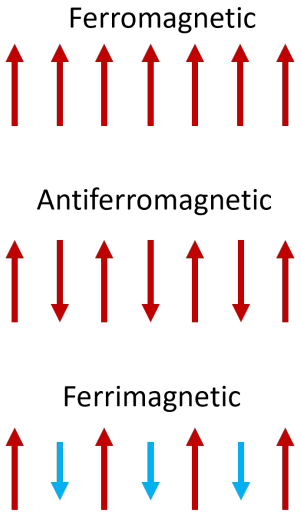


Figure 1.1: Schematic illustration of three elementary types of magnetic ordering. Ferromagnetic: all magnetic moments align in the same direction. Antiferromagnetic: magnetic moments alternate between up and down directions. Ferrimagnetic: opposing magnetic moments are unequal, resulting in a net magnetic moment.

## 1.1 Magnetic order and underlying interaction

Magnetism is intrinsically a quantum mechanical property. The phenomenon of magnetism is rooted in the spin degree of freedom of electrons (also orbital degrees of freedom without which there would be no diamagnetism), which can be considered as discrete and indivisible magnetic dipoles. Macroscopic magnetization emerges from the alignment and ordering of these microscopic magnetic moments.

There exist many magnetically ordered states. The most common are ferromagnetic, antiferromagnetic and ferrimagnetic. The ferromagnetic state is characterized by parallel alignment of neighboring magnetic moments. Antiferromagnetic state on the other hand is characterized by net zero macroscopic magnetic moment i.e. in a simple case that would mean that the neighboring magnetic moments are oriented antiparallel. The ferrimagnetic state is a state where neighboring magnetic moments do not cancel completely or there exist multiple sites where some magnetic moments are parallel and some are antiparallel so that there exists macroscopic magnetization. These types of elementary orders are displayed in Figure 1.1.

The order and alignment in a magnetic material must appear due to an interaction. Let us consider two magnetic moments in space. These magnetic moments interact via the dipolar interaction,

$$E = \frac{\mu_0}{4\pi r^3}\left[\mu_\mathbf{1}\cdot\mu_\mathbf{2} - \frac{3}{r^2}\left(\mu_\mathbf{1}\cdot\mathbf{r}\right)\left(\mu_\mathbf{2}\cdot\mathbf{r}\right)\right] \tag{1.1}$$

where $E$ is the interaction energy, $\mu_\mathbf{1}$ and $\mu_\mathbf{2}$ are magnetic dipoles and $\mathbf{r}$ is the separation vector. When considering only the first term ($E \propto \frac{1}{r^3}$, minimum of the

energy is achieved when the magnetic moments are antiparallel and maximum when magnetic moments are parallel. If we were to evaluate Equation 1.1 with common experimental values (e.g. $\mu = 1\mu_{\mathrm{B}}$, $r = 1\text{Å}$), we can assess the energy of interaction, which turn out to be on the order of 1 Kelvin. In this thesis, the materials investigated exhibit magnetic ordering at temperatures far above 1 Kelvin (approximately 1000 Kelvin). Thus, we can deduce that thermal energy at these higher temperatures would disrupt any magnetic order based only on dipolar interactions. It should be noted that dipolar interaction is relevant in magnets that order at temperatures comparable to the interaction strength [9]. This interaction is also one of the interactions that determine the magnetic domain formation[10], but it is not responsible for magnetic order in hexaferrites.

The foundation for establishing magnetic long-range order lies in the exchange interaction, a fundamental mechanism governing inter-particle behavior. This quantum mechanical interaction can be described by the Heisenberg Hamiltonian, a model that is central to understanding magnetic ordering:

$$\hat{\mathcal{H}}_{spin} = -\sum_{i,j} J_{ij}\, \mathbf{S}_i \cdot \mathbf{S}_j, \tag{1.2}$$

where $\mathbf{S}_i$ and $\mathbf{S}_j$ are the spin operators at sites $i$ and $j$, and $J_{ij}$ is the exchange integral, defining the interaction strength between these spins. The exchange integral $J_{ij}$ can be represented by:

$$J_{ij} = \int \psi_a^*(\mathbf{r}_1)\psi_b^*(\mathbf{r}_2)\hat{\mathcal{H}}\psi_a(\mathbf{r}_2)\psi_b(\mathbf{r}_1)\, \mathrm{d}\mathbf{r}_1\, \mathrm{d}\mathbf{r}_2, \tag{1.3}$$

where $\psi_a$ and $\psi_b$ are the single-particle wave functions of states $a$ and $b$, and $\hat{\mathcal{H}}$ represents the Hamiltonian of the system. The Hamiltonian contains the kinetic energy of the electrons, their attraction to the nucleus, and most importantly for this discussion, the Coulomb interaction between the two electrons [11]. The symmetry of the wave function under particle exchange implies that for two identical particles, the spatial part of the wave function must reflect the exchange symmetry (the requirement that the total wavefunction changes sign when two fermions are swapped), a result of Pauli's exclusion principle [9].

The summation $\sum_{i,j}$ in Equation 1.2 is taken over all spin pairs twice, capturing the interaction of every spin pair in the lattice. This interaction is a consequence of the quantum mechanical principle that requires the overall wave function to be either symmetric or antisymmetric under particle exchange, which ultimately leads to magnetic ordering effects like ferromagnetism and antiferromagnetism, depending on the sign of $J_{ij}$.

The Equation 1.2 defines the relative orientations of the spin pairs. In a solid, the sum must be done over all pairs of spins, meaning that the answer is not easily obtainable and it is computationally very expensive for almost all but the simplest

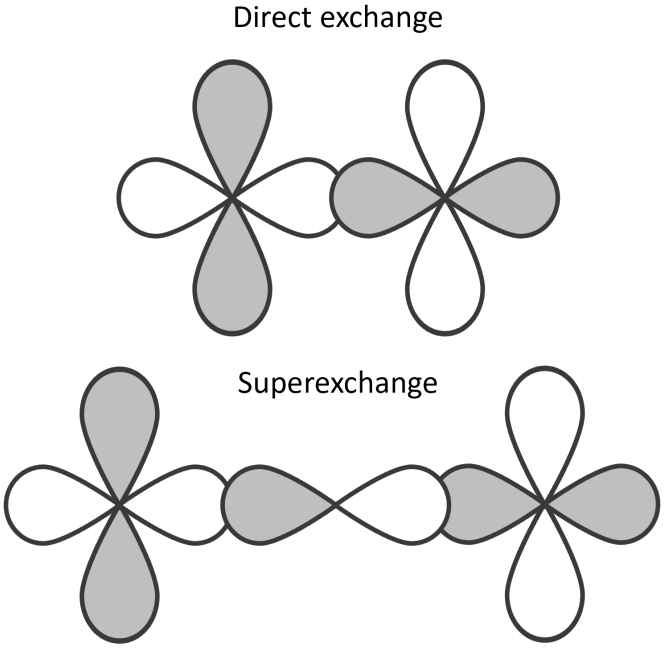


Figure 1.2: Schematic illustration of magnetic interactions via orbital overlap. (Top) Direct exchange, where magnetic coupling occurs through direct overlap of adjacent $d$-orbitals. (Bottom) Superexchange, an indirect interaction mediated by an intermediary atom ($p$-orbital), facilitating magnetic coupling through overlapping $d$-orbitals across the intermediary atom.

cases. The exchange interaction can be realized in multiple ways. The straightforward way is, if two neighboring magnetic atoms interact via exchange interaction directly, so called direct exchange (See Figure 1.2). Although conceptually the simplest, this is rarely the case due to strong localization of atomic orbitals. This exchange occurs in metals, however delocalized electrons introduce complications like spin polarized bands and non-discrete values of magnetic moment.[9].

The more common realization of magnetic interaction is the so called superexchange. In superexchange electrons of the magnetic ions interact via the orbitals of the non-magnetic ion which is placed between the atoms as shown in figure 1.2. In the figure we show $d$ and $p$ orbitals for magnetic and non-magnetic ions respectively as these are the orbitals responsible for superexchange between Fe ions in hexaferrites. Superexchange is influenced by the overlap and orientation of the M-L-M bonds (Metal-Ligand-Metal) within a crystal lattice. Superexchange delocalizes electrons through the non-magnetic ions. It is enabled through mixing of ground and excited states and Pauli exclusion principle, favoring an antiferromagnetic alignment[9, 12].

Other realization of exchange interactions is solids are: RKKY - where electron spins are mediated by conduction electrons, double exchange - essentially a mixed

valency superexchange interaction and Dzyaloshinsky-Moriya interaction - exchange interaction involving an excited state of a one ion and the ground state of another ion leading to an antisymmetric exchange term in the spin Hamiltonian ($\mathbf{D} * ij \cdot (\mathbf{S}_i \times \mathbf{S}_j)$). Among the listed exchange interactions superexchange is predominant mechanism for magnetic interaction in this thesis (hexaferrite materials), with a small contribution of direct exchange[13].

In this thesis a wide range of magnetic phenomenology and experiments was investigated. Usually when describing magnetic effects, we use parameters such as the Bohr magneton, Curie temperature, Néel temperature, Curie constant, and magnetic susceptibility.

The Bohr magneton ($\mu_\mathrm{B}$) is the unit of magnetic moment, commonly used to quantify the magnetic moments of electrons. The Curie temperature ($T_\mathrm{C}$) is the critical temperature above which a ferromagnetic material loses its magnetic order and becomes paramagnetic. The Néel temperature ($T_\mathrm{N}$) marks the transition of an antiferromagnetic or ferrimagnetic state to a paramagnetic state of a material. The Curie constant ($C$) appears in the Curie-Weiss law ($\chi = \frac{C}{T-T_\mathrm{C}}$) and describes the material's magnetic susceptibility and reflects the effective magnetic moment of its magnetic ions. Magnetic susceptibility ($\chi$) measures how much a material becomes magnetized in response to an applied magnetic field, providing insights into the magnetic interactions present. These parameters, together with the exchange interaction previously described are used in describing the magnetic states and the details about them can be found in most magnetic textbooks [9, 14, 15]. In future sections we will go into detail regarding some of these parameters.

### 1.1.1 Weiss model of uniaxial antiferromagnetism

Mean field theory is a theory that provides the framework to describe magnetically ordered states[1] by averaging the interactions of spins on a lattice, creating a mean or molecular field. In this thesis materials known as M-type hexaferrites have been investigated. These materials exhibit a ferrimagnetic ordered state. Although analogous mean-field calculations for ferrimagnets do exist (e.g., two-sublattice models with unequal moments [19]), for clarity and simplicity we adopt here the Weiss model formulated for antiferromagnets. We do this because qualitative conclusions remain applicable [9, 19, 20].

The derivation of this model for ferrimagnets is complicated due to non-compensation of the sublattices, but the results hold still qualitatively due to the presence of distinct magnetic sublattices with unequal magnetic moments. This non-compensation leads to a net magnetization in the ordered state, which

[1]Historically it was first used as tool in condensed matter physics [16]. In recent years it has found use beyond materials and into fields such as game theory[17] and epidemiology [18].

distinguishes ferrimagnets from antiferromagnets. Despite these differences, the qualitative insights provided by the Weiss model for antiferromagnets remain applicable, as they capture essential features of the temperature-dependent magnetic behavior and the transition to a ferrimagnetic state. We will use this model to interpret the obtained experimental data [9, 20].

The Weiss model starts with a statement that we have two distinct magnetization sublattices. Those two sublattices create molecular fields of the form,

$$\begin{aligned} \mathbf{B}_a &= \mathbf{H} - q_2\mathbf{M}_a - q_1\mathbf{M}_b \\ \mathbf{B}_b &= \mathbf{H} - q_2\mathbf{M}_b - q_1\mathbf{M}_a \end{aligned} \tag{1.4}$$

where $\mathbf{H}$ is the external magnetic field, $q_{1,2}$ is the Weiss constant, which quantifies the proportional relationship between the molecular field and the magnetization, $\mathbf{B}_{a,b}$ are molecular fields, and $\mathbf{M}_{a,b}$ are the magnetization of the sublattices $a$ and $b$. The molecular fields produce magnetization on each sublattice of the form,

$$M_{a,b} = \frac{1}{2} n g \mu_{\mathrm{B}} S B_S \left( g \mu_{\mathrm{B}} S B_{a,b} / kT \right) \tag{1.5}$$

where $B_S$ denotes Brillouin's function, $n$ represents the concentration of magnetic moments, $g$ signifies the electronic g-factor, $\mu_{\mathrm{B}}$ stands for the Bohr magneton, $S$ denotes spin, $k_{\mathrm{B}}$ represents Boltzmann's constant and $T$ stands for temperature. The equation (1.5) describes the magnetization $M$, arising solely from the contribution of a magnetic ion with spin $S$ in a magnetic field $B$. Condition for antiferromagnetic coupling is expressed as $M_a = -M_b$ which translates into $q_1 > q_2$ after a derivation shown in references [20, 21]. The expression $q_1 > q_2$ indicates that the spins experience a stronger interaction with the molecular field of the neighboring antiparallel sublattice than with the molecular field of their own sublattice.

The focus of thesis are the results connected to susceptibility. In this model the susceptibility depends on the orientation or direction of the applied field [9, 20]. At and below the ordering temperature $T_N$, so called Néel temperature, we can separate three important cases regarding to antiferromagnets response to magnetic field. Magnetic field oriented perpendicular to the spontaneous magnetization produces susceptibility $\chi_\perp$ independent of temperature with value

$$\chi_\perp = \frac{1}{q_1}. \tag{1.6}$$

Figure 1.3 shows how the magnetic field influences the magnetization. It should be noted that this is valid only if small magnetic fields are applied i.e. no reorientation effects are observed[9, 20].

When the magnetic field is aligned parallel to the spontaneous magnetization susceptibility $\chi_\parallel$ exhibits two distinct behaviors described by two limits. The first limit demonstrates the effects at temperatures well below the transition temperature,

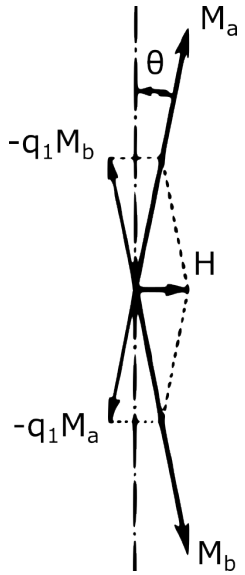


Figure 1.3: Representation of magnetization induced in antiferromagnet when field is applied perpendicular to spontaneous magnetization. Adapted from reference[20].

$\approx$ 0K. In this limit the susceptibility vanishes and further rise of magnetic field induces no magnetization. On the other hand, the second limit emerges as the temperature approaches the Néel temperature, where susceptibility reaches a defined value, specifically equal to

$$\chi_{\parallel}\left(T = T_N\right) = \frac{1}{q_1}. \tag{1.7}$$

Above Néel temperature, there is no spontaneous magnetization and susceptibility takes the form of the Curie-Weiss law

$$\chi = \frac{C}{T + \Theta} \tag{1.8}$$

where $C$ and $\Theta$ are Curie constant and Weiss temperature respectively. The temperature dependence of susceptibility of antiferromagnet is summarized in the Figure 1.4. This behaviour is characteristic for uniaxial antiferromagnets, and is readily observed experimentally in different systems [9, 20, 22]. The full derivation of the model can be found in included references [20, 21].

### 1.1.2 Magnetic domains

Magnetically ordered states (ferro- and ferrimagnets) are characterized by regions of uniform magnetization called magnetic domains. Magnetic domains form as a result of the competition between the various energy contributions in a magnetically ordered state. The formation of domains allows for a balance between these competing effects, with domain walls serving as regions of transition between different magnetization directions. The existence of domains is due to the minimization of the total

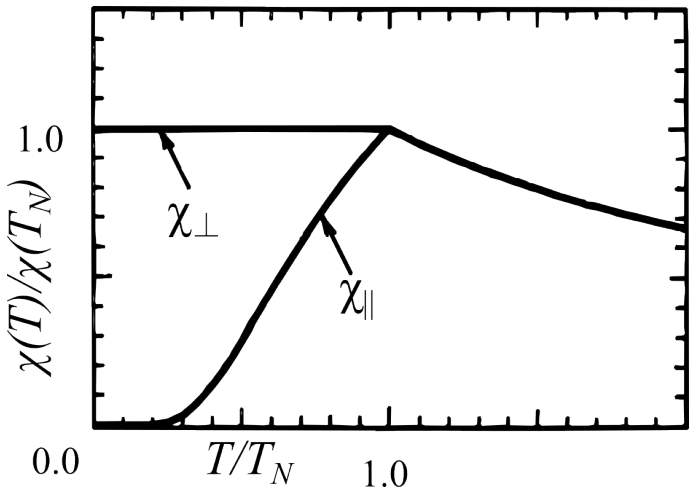


Figure 1.4: Temperature dependence of susceptibility for antiferromagnets. Adapted from reference[20].

energy of the system by reducing stray field energy, while allowing regions of uniform magnetization dictated by exchange interactions[23]. The total phenomenological energy of the magnetically ordered system is given by

$$E_{\text{tot}} = \int \Big[ A(\nabla \mathbf{m})^2 + F_{\text{an}}(\mathbf{m}) - \mathbf{H}_{\text{ex}} \cdot \mathbf{M} + \frac{1}{2}\mathbf{H}_{\text{d}} \cdot \mathbf{M} - \boldsymbol{\sigma}_{\text{ex}} \cdot \boldsymbol{\varepsilon}^0 + \frac{1}{2}(\mathbf{p}_{\text{e}} - \boldsymbol{\varepsilon}^0) \cdot \mathbf{c} \cdot (\mathbf{p}_{\text{e}} - \boldsymbol{\varepsilon}^0) \Big] \, dV \tag{1.9}$$

The first term in the Equation 1.9 the exchange energy, where $A$ is the exchange constant and $\mathbf{m} = \mathbf{M}/M_s$ is the normalized vector field of magnetization directions so called reduced magnetization. The exchange energy promotes a uniform alignment of neighboring spins. It arises from quantum mechanical exchange interactions, ensuring that magnetization vectors prefer parallel alignment. When neighboring spins deviate from perfect alignment, the system receives an energy penalty[23].

The second term of the Equation 1.9 is the anisotropy energy term where $F_{\text{an}}$ describes all contributions from crystal and structural magnetic anisotropies [2]. The anisotropy energy arises from the material's crystal structure, affecting how magnetization aligns relative to the crystallographic axes. This energy results from spin-orbit interaction. Intrinsic crystal anisotropies and those induced by deviations like lattice defects or atomic ordering are differentiated. Shape effects are not included in this term. It is crucial in determination the 'easy' and 'hard' axes of magnetization. Uniaxial anisotropy, relevant for this thesis, dictates that magnetization aligns along a single axis, with substantial energy cost for the case when the magnetization deviates from this axis[23].

[2]Here we differentiate anisotropy from unperturbed crystal structure and induced anisotropy i.e. deviations from ideal symmetry for example lattice defects [23]

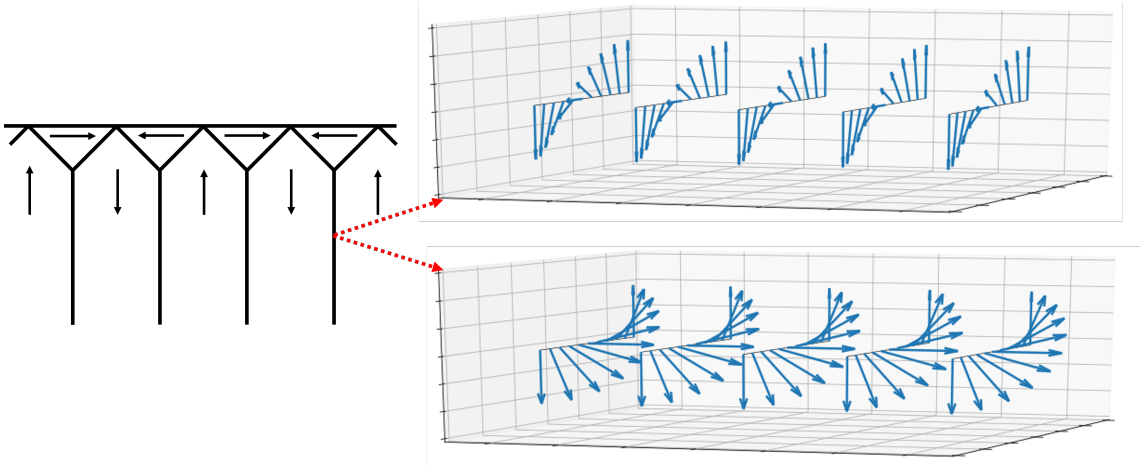

Figure 1.5: Representation of magnetic domains, magnetic moment spatial distribution and domain walls. On the left, a schematic representation of magnetic domains is displayed, adapted from references [24] and [23]. On the right, visualizations illustrate two primary types of magnetic domain walls: the Néel wall (top) and the Bloch wall (bottom).

The third term of the Equation 1.9 is the external field energy where $\mathbf{H}_{\text{ex}}$ is the external field and $\mathbf{M}$ is the magnetization. When an external magnetic field is applied to a ferromagnet, the system's energy changes according to the Zeeman energy term. The system minimizes this energy when the magnetization aligns with the external field, which can lead to domain realignment or reconfiguration[23].

The fourth term of the Equation 1.9 is the stray field energy term, where $\mathbf{H}_{\text{d}}$ is the stray field defined as the field generated as the divergence of the magnetization $\nabla \cdot \mathbf{H}_d = -\frac{1}{\mu_0}(\nabla \cdot \mathbf{M})$. Stray field energy arises from the stray magnetic fields generated by the ferromagnet itself, particularly in regions where the magnetization has a nonzero divergence, such as at surfaces and domain walls. This energy is always positive, meaning it tends to oppose the formation of stray fields by favoring internal domain configurations that minimize these fields. The calculation of stray field energy involves complex integrals over the volume and surface of the magnetic body, making it a key factor in domain structure formation[23].

Fifth and the sixth term are external stress energy and magnetostricitve energy, where $\boldsymbol{\sigma}_{\text{ex}}$ is the symmetric tensor that collects all stresses of non-magnetic origin, $\boldsymbol{\varepsilon}^0(\mathbf{m})$ is the free magneto-elastic deformation, $\mathbf{c}$ is the elastic constant tensor and $\mathbf{p}_{\text{e}}$ is the actual distortion, the compatible deviation from the initial state [23].

### 1.1.3 Domain walls and domain wall dynamics

Magnetic domains can be arranged in numerous configurations, varying significantly in size due to the complexity of the total energy Equation 1.9 that governs their

behavior. Within a material, the orientation of magnetization transitions gradually between domains. These transitional regions, where the magnetization shifts orientation progressively, are known as domain walls. Two primary types of domain walls in ferromagnetic materials are Bloch walls and Néel walls, each with distinct structures and behaviors[23]. Illustration of Bloch and Néel wall is shown on Figure 1.5.

In a Bloch wall, the magnetization rotates within the plane of the wall meaning that the direction of the magnetization gradually changes from one domain to the next, maintaining the magnetization parallel to the plane of the domain wall. This structure is effective at reducing the exchange energy, as it minimizes abrupt changes in the magnetization direction. Bloch walls are especially prevalent in thick magnetic samples, where the energy associated with the magnetic stray field is less critical due to the large volume of a material[23].

Néel walls, on the other hand, are more common in thin films and near the surface of ferromagnetic materials. In a Néel wall, the magnetization rotates in a plane perpendicular to the wall. This type of wall minimizes the stray field energy, making it more favorable in situations where the surface area of the material is large compared to its volume. Because stray field energy plays a more significant role in thin films, Néel walls help to reduce this energy contribution by confining the magnetic field lines within the material, rather than allowing them to extend into the surrounding space[23].

In this thesis, we investigated the dynamics of magnetic domain walls across various regimes. Several models describe magnetic domain wall motion, including one that characterizes the theoretical velocity variation of a one-dimensional (1D) interface, or domain wall, in a two-dimensional (2D) weakly disordered medium under low-force conditions, referred to as the creep model [25]. The domain wall motion regimes include creep, depinning, and flow. The creep regime is characterized by thermally activated motion, typically occurring at low magnetic fields, with velocity increasing exponentially as the field increases. As the field reaches a critical depinning threshold, domain walls enter the depinning regime, facing less resistance from disorder. At higher fields, the system transitions into the flow regime, where disorder becomes less relevant, allowing for more fluid, viscous motion. Additionally, in an ideal ferromagnetic film without pinning effects, the flow regime may involve both steady and precessional linear motions. The transition from steady to precessional flow occurs beyond the Walker field — the critical magnetic field that separates these two regimes of domain wall motion — indicating distinct changes in the internal wall dynamics [25].

In the part of the thesis, magnetic measurements were conducted at low magnetic fields, corresponding to steady or creep motion within the context of the models discussed. Since the primary focus of this thesis is not on the specific types of domain

walls or their motion, further analysis of this aspect will not be pursued. This choice is influenced by the selection of experimental techniques employed. Instead, the relevant focus for this study is on the dynamic response of the system—specifically, how the system behaves after the driving field is turned off. This dynamic response will be examined in detail in the following subsection.

### 1.1.4 Spin-lattice relaxation

Magnetic relaxation is a common name for phenomena where after a change in magnetic field $\Delta H$ the magnetization $M$ reaches a new equilibrium state after some characteristic time $\tau$. In ferro- and ferrimagnets domain wall motion is a significant contributor to magnetic relaxation, as spins within the walls can easily follow an oscillating magnetic field.

The Casimir–du Pré theory[26] of relaxation is a phenomenological theory that describes the behavior of magnetic susceptibility under a varying magnetic field. According to this model, energy exchange between spins and the lattice occurs through the spin-lattice interaction, characterized by distinct time scales for spin-spin and spin-lattice relaxation. The complex susceptibility $\chi(\omega)$ is expressed as:

$$\chi(\omega) = \chi_S + \frac{\chi_T - \chi_S}{1 + i\omega\tau}, \tag{1.10}$$

where $\chi_T$ and $\chi_S$ represent the isothermal and adiabatic susceptibilities, respectively, and $\tau$ is the relaxation time. The real part of the susceptibility, $\chi'(\omega)$, is associated with reversible processes, while the imaginary part, $\chi''(\omega)$, corresponds to energy dissipation due to irreversible processes. Equation 1.10 has the Debye relaxation form and describes a response governed by a single characteristic time. In magnetically ordered systems, this approximation is most appropriate for the linear regime of damped oscillations about an equilibrium configuration, as discussed in section 1.4.

The temperature dependence of relaxation time $\tau(T)$ is crucial for understanding magnetic systems. One common form is the Arrhenius law:

$$\tau(T) = \tau_0 \exp\left(\frac{\Delta E}{k_\mathrm{B} T}\right), \tag{1.11}$$

where $\Delta E$ is the activation energy, $k_\mathrm{B}$ is Boltzmann's constant, and $\tau_0$ is the characteristic time.

In ferro- and ferrimagnets, the response to a varying magnetic field may remain finite even in the absence of a dc magnetic field because the multidomain state contains domain walls whose displacement changes the net magnetization. In weak AC fields, the high-frequency response can arise from reversible damped oscillations of domain walls around their equilibrium positions, which may be approximated by

a Debye-like relaxation. This contribution should be distinguished from irreversible domain-wall displacement and creep, which become important at lower frequencies or under larger driving fields and generally lead to non-Debye behavior. The domain wall susceptibility, $\chi_w$, is given by:

$$\chi_w = \frac{2M_s^2 d_w}{KL}, \tag{1.12}$$

where $M_s$ is the saturation magnetization, $d_w$ is the domain wall width, $K$ is the anisotropy constant, and $L$ is the distance between two domains. The domain wall relaxation plays a key role in ferromagnets (ferri-), with irreversible wall displacements contributing to energy loss and relaxation time $\tau$ [26–29]. This result will be discussed in more detail in the subsection 3.1.3.

### 1.1.5 Barkhausen effect

The motion of domain walls in ferromagnetic (ferri-) materials can be influenced by the material's metallurgical properties. Domain walls can be pinned by imperfections like strains, surfaces, and impurities due to magnetoelastic coupling, which increases coercivity. As domain boundaries shift, the magnetization of the material changes discontinuously, a phenomenon known as the Barkhausen effect, first discovered by Heinrich Barkhausen in 1919. This effect which is closely tied to domain wall observation, provides valuable insights into the magnetization process, with each discontinuous step corresponding to domain wall movement. Additionally, these abrupt shifts sometimes produce magnetoacoustic emissions due to their coupling with the material's elastic modes [9, 30]. The effect is depicted in Figure 1.6.

The experimental results presented in this thesis do not include direct magnetization measurements; instead, the focus was on AC susceptibility measurements. The Barkhausen effect, typically characterized by discrete jumps in magnetization due to domain wall movements, is expected to introduce noise in the frequency regime of these measurements. The frequency of Barkhausen emissions typically spans from a few kilohertz to a few hundred kilohertz, although there are no strict upper or lower frequency limits[31], which is a domain of AC susceptibility measurements. Barkhausen noise produces a signal that is several orders of magnitude stronger than the inherent noise of the measurement apparatus. Measurements containing Barkhausen noise will be discussed in Appendix section.

## 1.2 Ferroelectricity

Ferroelectricity, the electrical dipole analogue to ferromagnetism, gives rise to materials that exhibit phenomena resembling those found in ferromagnetic materials.

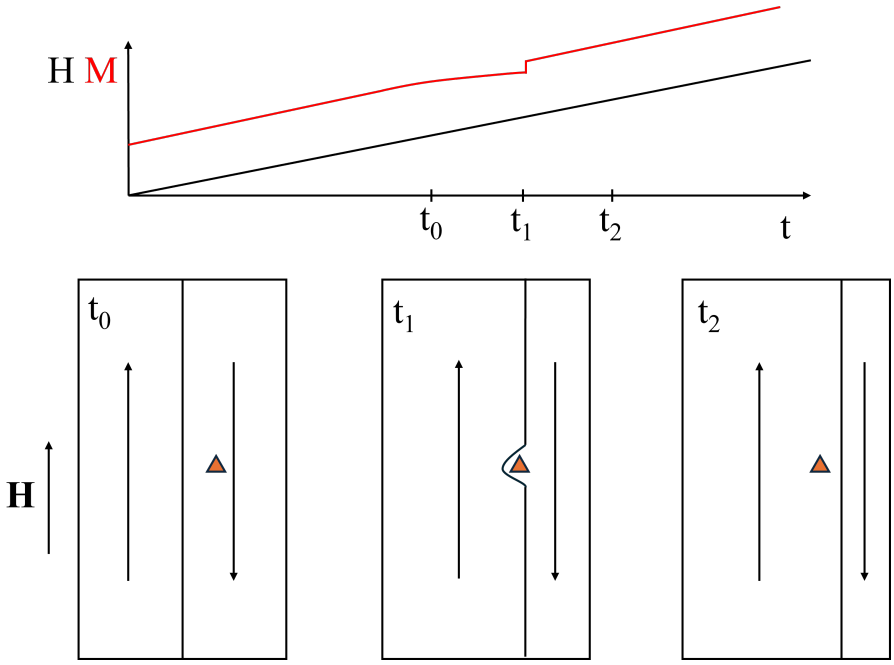


Figure 1.6: Illustration of the Barkhausen Effect. Top Panel: Relationship between the applied magnetic field $H$ (black line) and magnetization $M$ (red line) over time $t$. Bottom Panels (from left to right): Panel at $t_0$: Magnetic domain wall moves from left to right unencumbered. The triangular marker indicates a pinning center. Panel at $t_1$: At time $t_1$, the applied magnetic field $H$ reaches a pinning center, and further increase of the field induces domain wall "jump" over the pinning center. Panel at $t_2$: By $t_2$, further increase in $H$ has caused additional domain wall movement, with no influence from the pinning center.

An electric dipole consists of two equal and opposite charges separated by a finite distance, creating a dipole moment, which is a vector quantity describing the separation of charges within a system. In ferroelectric materials, the alignment of these dipole moments generates spontaneous polarization, even in the absence of an external electric field. This polarization can be reversed by applying an external field, a characteristic that leads to hysteresis similar to that seen in ferromagnets.

Symmetry plays a pivotal role in the existence of electric dipoles and, by extension, ferroelectricity. For a crystal to exhibit ferroelectricity, it must possess a non-centrosymmetric structure. A structure is centrosymmetric if it has an inversion center: a point $O$ such that for every atom at position $\mathbf{r}$ relative to $O$, there is an equivalent atom at $-\mathbf{r}$. In centrosymmetric crystals, dipoles cannot exist because any dipole moment formed in one direction is cancelled by an equivalent dipole moment in the opposite direction. Therefore, a necessary condition for ferroelectricity is that the crystal structure be polar, meaning it lacks a center of inversion. However, non-centrosymmetry alone is not sufficient for ferroelectricity; the crystal must also have spontaneous polarization that can be reversed under an external electric

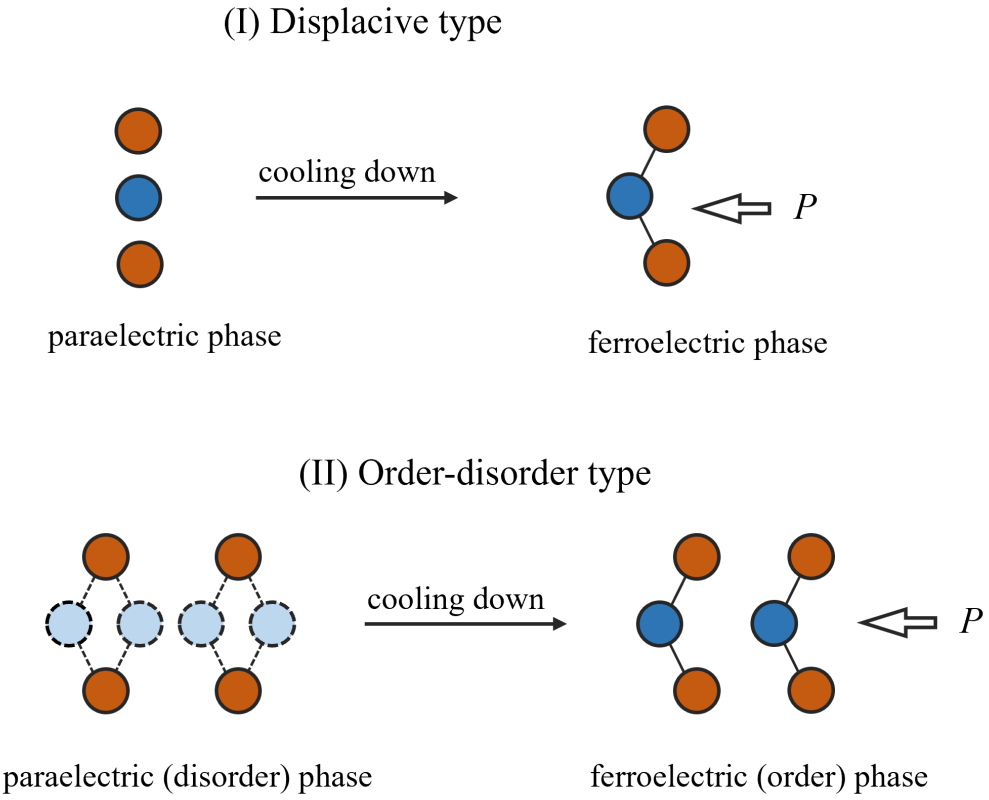


Figure 1.7: Two different types of ferroelectric transition. (I) Displacive type where a non-polar structure upon cooling enters a polar ordered structure. (II) Order-disorder type where a disordered polar phase orders. Adapted from [2].

field, distinguishing ferroelectric materials from other polar materials, for example pyroelectrics.

Two primary types of ferroelectric transitions exist: displacive and order-disorder transitions. In a displacive transition, ferroelectricity arises when certain ions in the crystal lattice shift from their equilibrium positions, leading to spontaneous polarization. This is typically described by the "soft mode theory," where a specific vibrational mode (phonon) of the crystal lattice becomes unstable as the material approaches the Curie temperature, causing the transition to a ferroelectric phase. This vibrational mode, known as the soft mode, is characterized by a frequency that decreases to zero at the phase transition, thereby driving the structural change.

In contrast, order-disorder transitions involve the reorientation of existing dipoles. Above the Curie temperature, the dipoles are randomly oriented due to thermal agitation, but as the temperature decreases, they align in a coherent direction, producing macroscopic polarization. The order-disorder model can be described using a pseudo-spin framework, where the dipole moments behave analogously to spins in a ferromagnetic system, ordering as the material cools. In Figure 1.7 displacive and order-disorder ferroelectrics are shown.

The exploration of ferroelectricity is not only significant for understanding the electric dipole behavior but also crucial when considering the potential coupling between electric and magnetic orders in materials, especially in the context of magnetoelectrics. Such materials, exhibiting both electric and magnetic order parameters, are promising candidates for novel functionalities in spintronics and memory devices, where electric fields can control magnetization, or vice versa. Understanding the fundamental physics of these transitions and couplings can offer new avenues for designing materials with enhanced magnetoelectric responses.

## 1.3 Magnetoelectric effect

In its most general form, the magnetoelectric effect denotes any coupling between the magnetic and electric properties of a material. This phenomenon encompasses a wide range of interactions where the magnetic state of a material can influence its electric properties, and vice versa. Typically, the magnetoelectric effect is presented in the context of the linear magnetoelectric effect[3]. The relationship between the electric and magnetic properties of a material can be described by a response function. Mathematically, this effect is characterized by a tensor quantity, which relates the induced polarization $P_i$ in a material to an applied magnetic field $H_k$ by

$$P_i = \alpha_{ik} H_k \tag{1.13}$$

where $\alpha$ is the linear magnetoelectric tensor and $i, k$ are respective directions of the induced polarization and magnetic field, with summation over repeated indices implied (Einstein summation convention).

The origin of the magnetoelectric effect is rooted in the interplay between electric and magnetic orders within a material. This effect arises from the coupling mechanisms that allow the magnetic field to induce electric polarization and the electric field to induce magnetization. For example in materials like $Cr_2O_3$, the magnetoelectric effect can be attributed to the shifts in electronic states caused by external electric fields, affecting the magnetic exchange interactions between ions[32, 33]. This is an example of a coupling mechanism that resides on a molecular level. On the other hand the coupling mechanism in magnetoelectric composites is achieved through the interaction between piezoelectric and magnetostrictive phases. The magnetostrictive component deforms in response to a magnetic field, inducing a strain that is transferred to the piezoelectric phase, which in turn generates an electric polarization, thus linking magnetic and electric properties through mechanical deformation[5].

[3]Beyond the linear magnetoelectric effect, higher-order effects also exist. The next significant term is the bilinear magnetoelectric effect, often referred to as the induced magnetoelectric effect. This phenomenon provides an intuitive explanation: a magnetoelectric effect that arises in the presence of a bias field [5].

Magnetoelectric effect in hexaferrites has mostly been found in complex hexaferrites like Y-type [4]. There are some proposed substitutions that could produce magnetoelectric effect in simpler M-type hexaferrites [8]. In this thesis, evidence will be presented on the coupling between magnetic and electric properties of the studied materials. The proposed origin of this coupling is complex, and it is not immediately evident whether the standard linear magnetoelectric effect is present. Although the linear magnetoelectric tensor was not measured, several attempts were made to investigate its properties and potential manifestations.

## 1.4 Phenomenological models of relaxation

The exploration of materials under the influence of external electric or magnetic fields enables us to investigate their response. The response in itself reveals the underlying dynamics and interactions that give rise to macroscopic phenomena. Within the response we can distinguish two distinct behaviors: resonance and relaxation. The resonating response is an under-damped solution modeled by damped harmonic oscillator, while the relaxation response mirrors an over-damped solution within the same model. The focus of the thesis lies predominantly on the exploration and analysis of a few phenomenological relaxation models, as they hold more relevance and offer an insight into the nature of material behavior under external field.The resonance models are implicitly connected to X-ray spectroscopies, in which resonances arise when the incident photon energy coincides with the energy difference between core and unoccupied electronic states, leading to a pronounced enhancement in absorption or scattering. However, our focus there is on the conditions under which those resonances appear as in Section 1.6, rather than on the resonance models themselves.

### 1.4.1 Debye relaxation model

The Debye relaxation model is an elementary model which is used in studying the response of a material to an applied electric or magnetic field [34]. It was formulated by Peter Debye in the early 20th century. The model describes the delay between the material's polarization (general polarization electric or magnetic, usually called magnetization) as a response to the external field. The property that is generally common to relaxation models is the distribution of relaxation times, which for the Debye relaxation is single valued. This means that there is no underlying distribution of intrinsic physical property that causes relaxation such as size or interaction of the particles.

Mathematically the model is represented by the following equation for complex

susceptibility

$$\chi^*(\omega) = \chi_\infty + \frac{\chi_0 - \chi_\infty}{1 + i\omega\tau} \tag{1.14}$$

where $\chi_\infty$ is susceptibility at high frequencies, $\chi_0$ is the at low frequency, $i$ is the imaginary unit, $\omega$ is the angular frequency and $\tau$ is the relaxation time. At low frequencies ($\omega \to 0$), susceptibility has value $\chi_0$ while at the opposing limit ($\omega \to \infty$) it has value of $\chi_\infty$. Between those limiting values a sigmoidal change in susceptibility is occurring, where its shape is defined by relaxation time $\tau$ and the numerator which can be redefined as the strength of relaxation $\Delta\chi$ to support an interpretation.

### 1.4.2 Cole-Cole model of relaxation

When describing AC susceptibility and dielectric spectroscopy results, the Cole-Cole model is a conventional framework following almost the same physical meaning as the Debye Model. Historically, the Cole-Cole model was used in the description of charge density wave relaxation [35, 36] and glassy dynamics [34]. The Cole-Cole model distinguishes itself from the Debye model through the introduction of a broadening parameter $\alpha$, which introduces an exponent $1 - \alpha$ in its equation:

$$\chi(\omega) = \chi_\infty + \frac{\chi_0 - \chi_\infty}{1 + (i\omega\tau)^{1-\alpha}} \tag{1.15}$$

This modification assumes a distribution of relaxation times for a given process compared to the single relaxation time of the Debye model.

To visualize the distribution of relaxation times a following approach can be employed. Let us consider a scenario where multiple discrete Debye relaxation processes coexist with similar-valued relaxation times. Total susceptibility is the sum of all relaxation process and it equates to

$$\chi(\omega) = \chi_\infty + (\chi_0 - \chi_\infty) \sum_n \frac{\eta_n}{1 + i\omega\tau_n} \tag{1.16}$$

where $\eta_n$ is the statistical weight of relaxation process $n$ with relaxation time $\tau_n$, with $\sum \eta_n = 1$. If the number of relaxation processes is large enough weights can be represented by a distribution and sum can be replaced by an integral. This way Equation 1.16 is transformed into

$$\chi(\omega) = \chi_\infty + (\chi_0 - \chi_\infty) \int_{\tau_{\min}}^{\tau_{\max}} \frac{g(\tau)}{1 + i\omega\tau} d\tau \tag{1.17}$$

where $g(\tau)$ is the distribution of relaxation times. Equation 1.17 enables us in principle to construct a susceptibility response for a distribution of relaxation times with arbitrary shape.

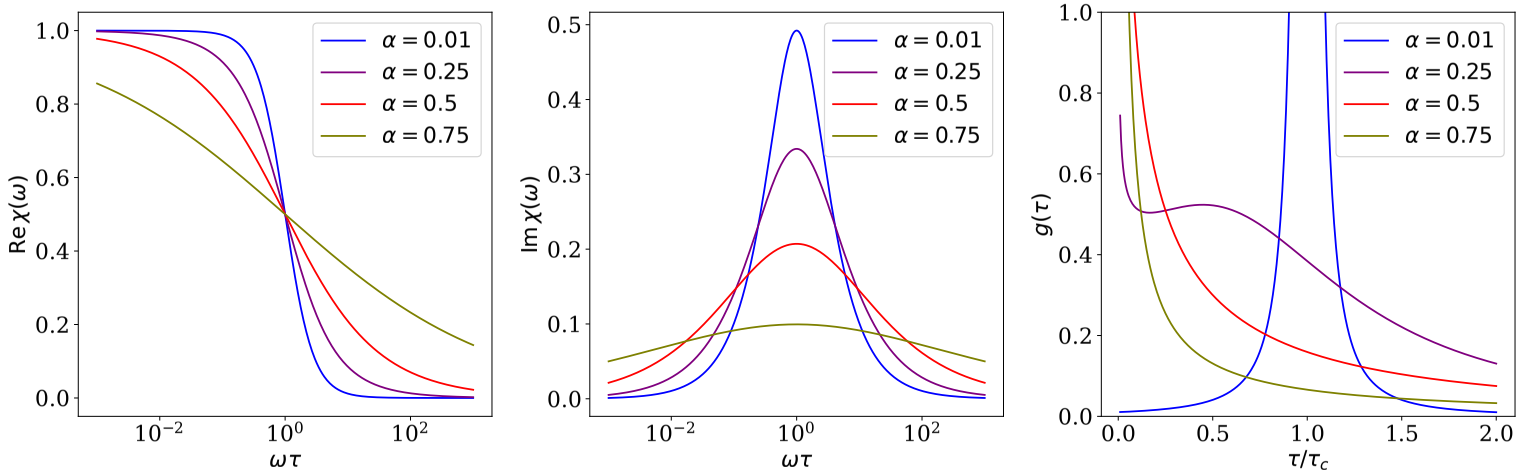


Figure 1.8: Illustration of the dependence of three different complex susceptibility and distribution functions on the broadening parameter $\alpha$. The left panel shows the real part of the susceptibility, $\mathrm{Re}[\chi(\omega)]$, as a function of the dimensionless frequency $\omega\tau$, for various values of $\alpha$. The middle panel presents the imaginary part of the susceptibility, $\mathrm{Im}[\chi(\omega)]$, over the same dimensionless frequency range. The right panel depicts the correlation function $g(\tau)$, Equation 1.18, as a function of normalized time $\tau/\tau_c$.

Cole-Cole model is enough to describe all of the relaxational phenomena relevant for this thesis[4]. In that model the distribution has shape

$$g(\tau) = \frac{1}{2\pi\tau} \frac{\sin \alpha\pi}{\cosh\left[(1-\alpha)\ln\left(\frac{\tau}{\tau_c}\right)\right] - \cos\alpha\pi}. \tag{1.18}$$

The function $g(\tau)$ has a pronounced peak at $\tau = \tau_c$, that is equal to $\delta(\tau - \tau_c)$ when $\alpha = 0$, producing a Debye relaxational model as a check of validity. Figure 1.8 shows the real and imaginary part of the susceptibility obtained from Cole Cole model as well as the distribution of relaxation times for few values of broadening parameter $\alpha$.

For this thesis measurements of both AC susceptibility and dielectric spectroscopy are modeled through Cole-Cole model. The specifics of the experimental techniques will be discussed in chapters 3.1 and 3.3.

## 1.5 Maxwell/Wagner and Electrode Polarization

In dielectric materials, polarization phenomena can occur at various internal and external boundaries, leading to significant contributions to the dielectric response. Two primary types of polarization that arise in such systems are Maxwell/Wagner interfacial polarization and electrode polarization. These phenomena can be modeled using a series of RC circuits, as shown in Figure 1.9, and are described using similar mathematical frameworks despite their different origins [34, 38]. In the context of this thesis, both phenomena are considered undesirable as they can obscure the response under investigation.

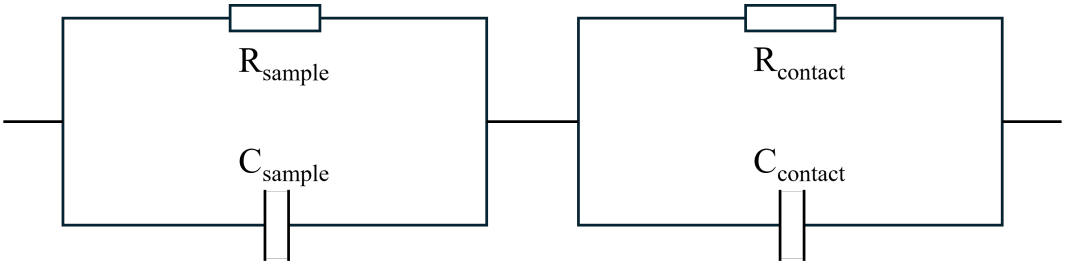


Figure 1.9: Equivalent circuit representation of Maxwell/Wagner and electrode polarization using a series of RC circuits. Each RC pair corresponds to a region with distinct permittivity and conductivity.

Maxwell/Wagner polarization is an interfacial phenomenon that occurs due to charge carrier blocking at boundaries between regions with different permittivity or

[4]There is no need for further complications of the model, for example Havriliak–Negami relaxation, see papers [28, 37] for other models and their properties [28, 37]. Other models introduce spectral features not visible in our experiments.

conductivity within a material. This is typically observed in heterogeneous systems, including colloids, suspensions, phase-separated polymers, and liquid crystals. In such systems, polarization arises from the accumulation of charges at the phase boundaries due to differences in electrical properties across the interfaces. This results in frequency-dependent changes in both the real ($\varepsilon'$) and imaginary ($\varepsilon''$) components of the dielectric function. The characteristic relaxation behavior of Maxwell/Wagner polarization can be described by the Debye model:

$$\varepsilon^*(\omega) = \varepsilon_\infty + \frac{\Delta\varepsilon}{1 + i\omega\tau_{\mathrm{MW}}}, \tag{1.19}$$

where $\varepsilon_\infty$ is the permittivity at high frequencies, $\Delta\varepsilon$ represents the change in permittivity, and $\tau_{\mathrm{MW}}$ is the relaxation time, given by:

$$\tau_{\mathrm{MW}} = \varepsilon_0 \frac{\varepsilon_1 + \varepsilon_2}{\sigma_{r1} + \sigma_{r2}}, \tag{1.20}$$

with $\varepsilon_0$ being the permittivity of free space, $\varepsilon_1$ and $\varepsilon_2$ the permittivity of the individual layers, and $\sigma_{r1}$ and $\sigma_{r2}$ their relative conductivities [34, 38].

Electrode polarization, on the other hand, arises at the interface between the sample and the measurement electrodes. This occurs due to the formation of interfacial layers of reduced conductivity, such as depletion layers or Schottky barriers, which contribute to the dielectric response. The dielectric effects of these interfacial layers are also frequency-dependent and can obscure the intrinsic dielectric behavior of the material. Such effects have been observed in materials, such as doped semiconductors, where it contributes (and is also partially identified by it) to apparent colossal dielectric constants [39]. These effects emphasize the importance of careful experimental design and interpretation, for example considerations of contact materials[34, 38].

Both Maxwell/Wagner and electrode polarization display dielectric dispersion, characterized by a step in $\epsilon'$ and a peak in $\epsilon''$. However, they differ in their dependence on material parameters. Maxwell/Wagner polarization is governed by the heterogeneity of the sample, while electrode polarization depends on the contact material and the interface geometry. The presence of contacts can induce dielectric relaxation in a sample that would otherwise exhibit no relaxation,[5] and, as shown by Equation 1.20, the mean relaxation time depends on the sum of the conductivities of the sample and the contact. In addition, the sample's conductivity may vary with temperature, which can generate processes that mimic slowing down phenomena and complicate interpretation of the dielectric response. This interaction between sample and electrode requires distinguishing relaxation in the sample from that arising at the contacts when analyzing experimental data. The procedures for separation are discussed and illustrated in references [34] and [40].

[5] A single RC circuit (sample only) shows no relaxation, but introducing another RC circuit in series (sample + contact) produces dispersion in the dielectric function.

The relevance of electrode polarization in this thesis lies in its potential to obscure (or create artificial) the dielectric behavior of hexaferrite crystals, a phenomenon that has also been reported in similar materials [38, 39]. Accurate identification and mitigation of electrode polarization effects are therefore essential for the correct interpretation of dielectric spectra [34, 38, 40].

## 1.6 Crystal field theory

The role of this section is to present crystal field theory. In this thesis, two experimental techniques performed, X-ray Absorption Spectroscopy (XAS) and Resonant Inelastic X-ray Scattering (RIXS), rely on an understanding of crystal field effects. While crystal field splitting is directly observable in XAS and RIXS spectra, it also indirectly influences material properties such as electrical transport and magnetic behavior. Thus understanding crystal field theory is essential for connecting these measurements to the broader physical phenomena under investigation [41, 42].

The behavior of an isolated atom can be described using the atomic Hamiltonian, which accounts for several fundamental interactions. In the absence of a crystal field, the initial, intermediate, and final states ($|i\rangle$, $|n\rangle$, and $|f\rangle$, respectively) of an electron are each described by the atomic Hamiltonian $H_{\text{atomic}}$:

$$H_{\text{atomic}} = H_{\text{kin}} + H_{e/N} + H_{e/e} + H_{\text{SO}}. \tag{1.21}$$

where $H_{\text{kin}} = \sum_{i=1}^{N} \frac{p_i^2}{2m}$ represents the kinetic energy of the electrons, with momentum $p_i$ and mass $m$. $H_{e/N} = \sum_{i=1}^{N} \frac{-Ze^2}{r_i}$ is the electrostatic interaction between electron $i$ (with charge $e$ at radius $r_i$) and the nucleus (with charge $Ze$). $H_{e/e} = \sum_{\text{pairs}} \frac{e^2}{r_{ij}}$ denotes the electron-electron Coulomb interaction, determined by both direct Coulomb repulsion and Coulomb exchange interaction. $H_{\text{SO}} = \sum_{i=1}^{N} \zeta(r_i) l_i \cdot s_i$ is the spin-orbit interaction for each electron in an open shell where $l_i$ is orbital angular momentum quantum number, $s_i$ spin angular momentum quantum number and $\zeta(r_i)$ is a constant. These four terms of the atomic Hamiltonian $H_{\text{atomic}}$, along with a given ground state $|\Psi\rangle$ , describe the isolated atom in each state.

The crystal field multiplet Hamiltonian $H_{\text{CF}}$ enhances the atomic Hamiltonian $H_{\text{atomic}}$ by incorporating the electrostatic influence exerted by adjacent atoms within a solid:

$$H = H_{\text{atomic}} + H_{\text{CF}}. \tag{1.22}$$

The crystal field Hamiltonian $H_{\text{CF}} = -e\phi(r)$ integrates the electronic charge $e$ with the potential $\phi(r)$ surrounding it. This potential $\phi(r)$ can be depicted as an expansion series involving spherical harmonics $Y_{LM}$:

$$\phi(r) = \sum_{L=0}^{\infty} \sum_{M=-L}^{L} r^L A_{LM} Y_{LM}(\theta, \phi) \tag{1.23}$$

In summary, the crystal field perturbs the atomic Hamiltonian and is expressed through a sum of spherical harmonics $Y_{LM}$ with coefficients $A_{LM}$, which are derived from the matrix elements $\langle 3d| \phi(r) |3d\rangle$. Here, the $3d$ orbitals are simply the atomic $3d$ eigenfunctions of the isolated ion, which we use as a basis to project the crystal-field potential.

Given the frequent occurrence of transition metal ions surrounded by six atoms forming an octahedral arrangement, we concentrate on the cubic crystal field case. These neighbors create an octahedral field, associated with the $O_h$ point group. In this thesis, within the unit cell, 18 out of 24 sites adopt an octahedral coordination environment. The remaining sites consist of 4 tetrahedral and 2 trigonal bipyramidal coordination environments. The tetrahedral and trigonal bipyramidal environments can be derived using the same procedure applied to the octahedral environment. More on the crystal structure will be discussed in the next chapter.

In a single-electron model within a spherical setting ($O3$), the $3d$ orbitals ($l = 3$) are five-fold degenerate ($2l + 1 = 5$). In an octahedral ($O_h$) crystal field five $3d$ orbitals split into two distinct symmetry groups:

- The doubly degenerate $e_g$ orbitals ($z^2$ and $x^2 - y^2$), oriented along the metal-ligand bonds and associated with $\sigma$-bonding.

- The triply degenerate $t_{2g}$ orbitals ( $xy, xz, yz$), positioned between the metal-ligand bonds and involved in $\pi$-bonding.

This splitting between the $e_g$ and $t_{2g}$ orbitals, is depicted in Figure 1.10. The Figure depicts splitting of the tetrahedral ($T_d$) and trigonal bi-pyramidal ($D_{3h}$) sites which are relevant for this PhD thesis[42, 43].

Having provided an overview of the key theoretical concepts in this chapter, we now able to introduce hexaferrite materials, which are the main topic of this thesis. These materials and their properties will be the focus of the next chapter.

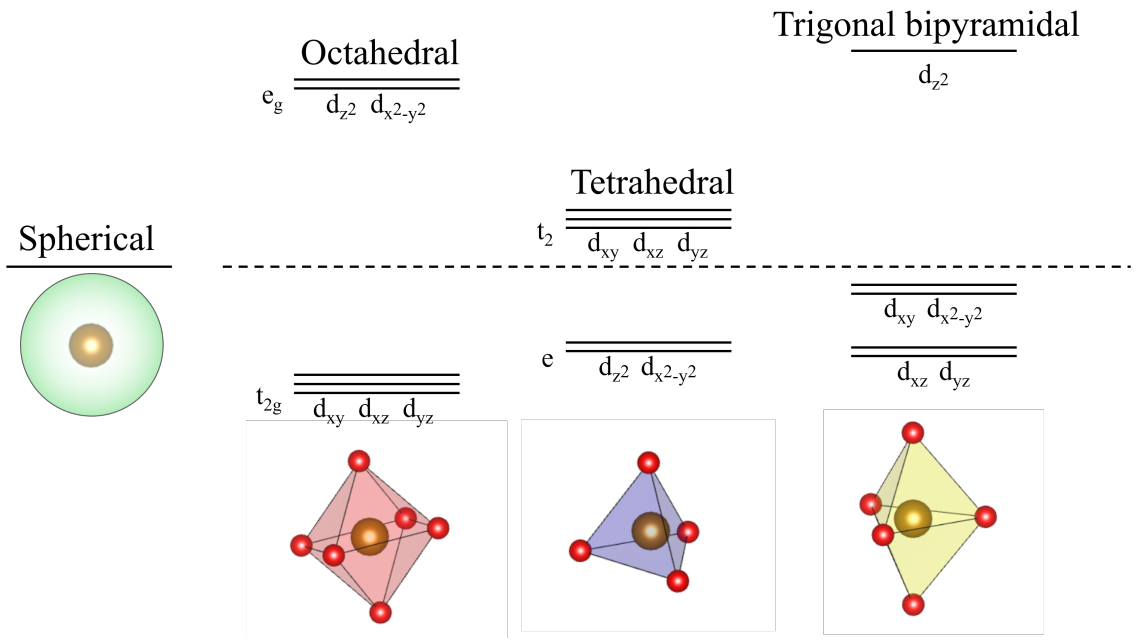


Figure 1.10: Illustration of crystal field splitting of $d$-orbitals for ions in spherical, octahedral, tetrahedral, and trigonal bi-pyramidal ligand field geometries. The spherical configuration, where charge is uniformly distributed over a sphere, shows degenerate $d$-orbitals. In the octahedral field, the $d$-orbitals split into two sets: the lower energy $t_{2g}$ set $(d_{xy}, d_{xz}, d_{yz})$ and the higher energy $e_g$ set $(d_{z^2}, d_{x^2-y^2})$. The tetrahedral field results in the opposite splitting pattern, with the lower energy $e$ set $(d_{z^2}, d_{x^2-y^2})$ and the higher energy $t_2$ set $(d_{xy}, d_{xz}, d_{yz})$. The trigonal bi-pyramidal field results in a unique splitting where $d_{xz}, d_{yz}$ are lowest in energy, while $d_{z^2}$ is the orbital with highest energy, and $d_{xy}$ and $d_{x^2-y^2}$ occupy intermediate energy levels. Each geometry is represented with a corresponding coordination structure where the central metal ion is surrounded by ligand ions or a distribution as in the case of spherical symmetry.

# Chapter 2

# Hexagonal ferrites

This chapter provides an overview of M-type hexaferrites, focusing on their structure, physical properties, associated phenomena, and synthesis method used for this thesis. This chapter is divided into 5 sections. The first section is dedicated to brief overview of the whole class of hexaferrites. The second section describes the crystal structure of the M-type hexaferrites and the relevant concepts like space group and coordination environments. Third section is dedicated to elementary magnetic and electric properties. Fourth section "Phenomena Concerning Hexaferrites" is the section where unique physical phenomena and properties are reviewed which are connected to the topic of this thesis. This section also encompasses other ongoing research that is indirectly associated with this thesis. Finally, the last section is dedicated to hexaferrite crystal synthesis.

Because this class of iron oxide-based materials have gathered a lot of interest since their discovery, an abundance of different topics regarding hexaferrites exist. In this thesis we touch on general topics but most of the topic are related to this thesis. For a more general and detailed view of these materials, reviews are recommended [1, 4, 44].

## 2.1 Types of hexaferrites

Hexaferrites, a class of iron oxide-based materials, have been extensively studied since their discovery in the 1950s [45] for their magnetic properties and structural characteristics. These materials can be categorized into six main types based on the crystal structure: M-type, W-type, X-type, Y-type, Z-type, and U-type, each with their own general formula. The hexaferrite crystal structures can be viewed as being composed from simpler blocks, which are stacked uniquely for a particular hexaferrite type [1, 4].

The primary structural characteristic shared by this class of materials is the pronounced anisotropy of their crystal structure, wherein the c-axis is significantly larger than the other crystallographic directions. From a magnetic perspective, these materials are typically ferrimagnets, finding notable applications in the permanent magnet industry [1, 4]. In recent years, research has increasingly focused on the magnetoelectric properties of hexaferrites, particularly within the Y- and Z-type varieties [4]. These complex hexaferrites exhibit promising multiferroic behavior, positioning them as strong candidates for next-generation electronic devices. Of particular interest, Z-type hexaferrites, such as $Sr_3Co_2Fe_{24}O_{41}$, have demonstrated room-temperature magnetoelectric effects, representing a significant breakthrough in the practical applications of these materials [1, 4].

In this thesis, we investigate the magnetic and electric properties of M-type hexaferrites with chemical formula $(Ba,Pb)(Fe,Al)_{12}O_{19}$. Although this type represents the simplest form of hexaferrites, it still features a highly complex unit cell. The following sections will delve into the peculiarities of their crystal structure and explore their intriguing physical properties.

## 2.2 Crystal structure of M-type hexaferrites

M-type hexaferrites have a general formula unit $AB_{12}O_{19}$, where A are usually earth-alkali metals, B are usually trivalent transition metals while O is oxygen. Crystal structure of M-type hexaferrites is predictably hexagonal isostructural with magnetoplumbite (the first discovered and naturally found mineral which is a hexagonal ferrite). It is agreed upon that the average representative space group is P6/mmc containing two formula units. The c-axis of this space group contains a mirror plane located at A atom and a 6 fold rotational symmetry.

The crystal structure of hexagonal ferrites is shown on the left part of Figure 2.1. Here the red spheres represent oxygen atoms, green spheres represent earth-alkali metals while all other spheres are iron atoms in $3^+$ oxidation state. Different colors of polyhedra represent crystallographically non-equivalent sites. These sites are extracted on right part of the Figure 2.1. In these five non-equivalent sites

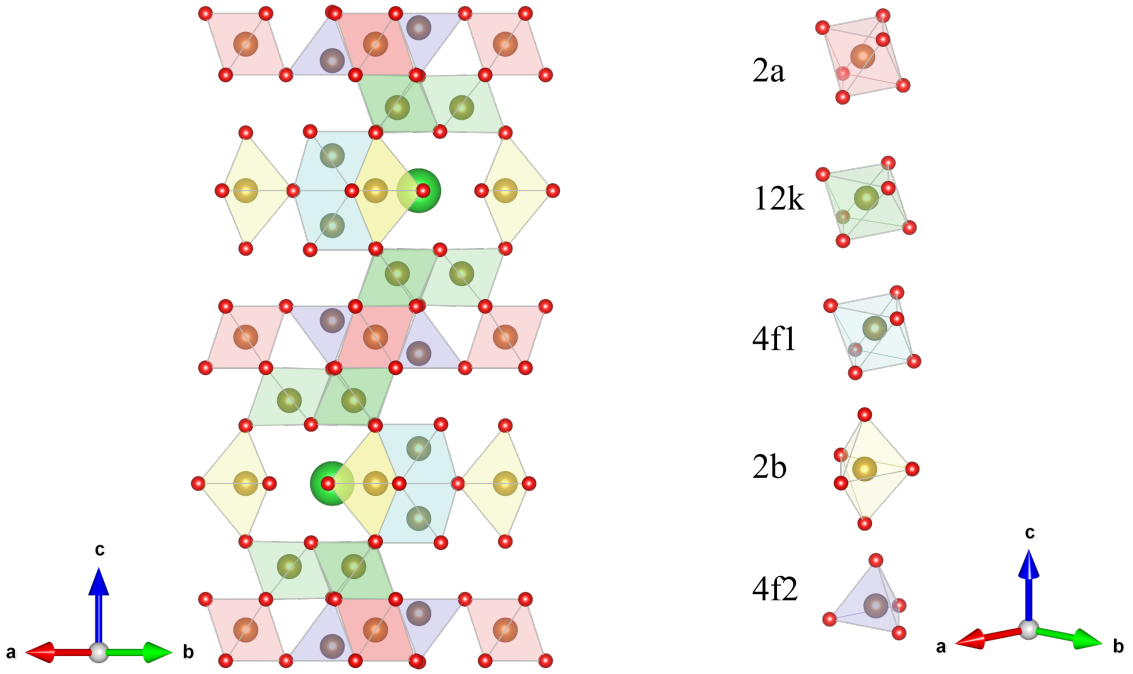


Figure 2.1: Left: Crystal structure as viewed from $[\bar{1}, \bar{1}, 0]$ direction. Right: Five unique iron coordinations. Red spheres represent oxygen atoms, green spheres represent earth-alkali metal, while all other color spheres are iron atoms in different coordinations. Crystallographic information file obtained from [46, 47].

there are 3 different coordinations. These are octahedral $O_h$ (2a,12k and 4f1 sites), bi-pyramidal $C_{3v}$ (2b) and tetrahedral $T_d$ (4f2).

## 2.3 Physical properties

The most common magnetic structure of M-type hexaferrites is ferrimagnetic. The $T_c$ of the $BaFe_{12}O_{19}$ (BaM), an elementary M-type hexaferrite, is around 720 K. Magnetic moment per iron atom is calculated by considering $Fe^{3+}$ in high-spin configuration, which has a spin state $S = 5/2$ due to the quenching of orbital angular momentum. Equation for magnetic moment calculation of a magnetic ion is $\sqrt{g^2 S(S+1)}$ where $g$ is the spin $g$-factor which has value $\approx 2$. This evaluates to 5.92 $\mu_B$ per iron atom. Some text books use a rule of thumb 1 $\mu_B$ per unpaired electron [1], which will adopt for the description of the properties.

Magnetic interaction stabilizes a collinear structure where out of the 24 available magnetic moments(iron sites), 16 are oriented in parallel configuration while the remaining 8 magnetic moments are in antiparallel configuration, resulting in $5 \cdot (16-8)$=40 $\mu_B$ per unit cell. Magnetic structure with crystal structure for reference is shown in Figure 2.2. From the figure we can determine which iron sites are parallel (2a, 12k and 2b) and which are antiparallel (4f1, 4f2).

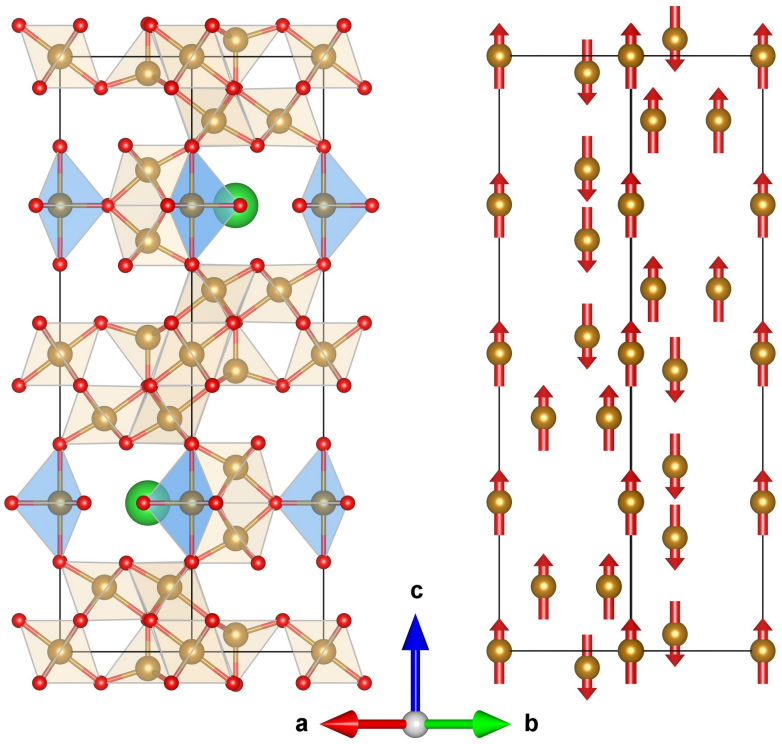


Figure 2.2: Left: Crystal structure of M-type hexaferrite $BaFe_{12}O_{19}$ (BaM) as viewed along $[\bar{1}, \bar{1}, 0]$ direction. Green spheres represent barium atoms, red represent oxygen, while gold spheres and polyhedra represent iron atoms and their coordinations. Blue hexahedrons mark trigonal by-pyramidal sites. Right: Magnetic structure of M-type hexaferrite $BaFe_{12}O_{19}$ (BaM) as viewed along the same direction. Red arrows represent local iron magnetic moments.

Magnetic anisotropy of the structure is uniaxial, where for most of the M-type hexaferrites have easy-axis anisotropy with notable exceptions where magnetic anisotropy has easy-plane shape [1]. The magnitude of the magnetocrystalline anisotropy is large (It is this property to which hexaferrites owe their industrial adoption), and it was calculated that surprisingly the largest contribution comes from the bi-pyramidal site ([48] and references therein).

From an electrical point of view, these materials are considered semiconductors. The primary activated carriers have been attributed to $Fe^{2+}$ [49]. While the exact source of $Fe^{2+}$ ions is not extensively discussed, it is linked to oxygen deficiency. However, as this thesis will demonstrate, this explanation might not fully apply, given the strong correlations observed between electric and magnetic transport that challenge interpretations based solely on oxygen deficiencies.

## 2.4 Phenomena concerning hexaferrites

Most prominent physical properties and behaviors of M-type hexaferrites originate from the geometry of the bi-pyramidal (2b) sites (Figure 2.1). The bond lengths within these sites are non-uniform. Table 2.1 lists two unique bond lengths in

| | Bond Length / Å |
|---|---|
| Fe-O in plane | 1.9 |
| Fe-O apical | 2.3 |

Table 2.1: Bond lengths in bi-pyramidal iron site (2b) for the same structure as in Figure 2.1

$BaFe_{12}O_{19}$ 2b site[1], where we can see the difference between two characteristic Fe-O bonds. This anisotropy can in principle induce iron distortion, primarily in apical direction. The position of iron in these sites is crucial, as it can affect the overall symmetry of the hexaferrite structure. When the symmetry is reduced, as in the case of the apical distortion, it provides an opportunity for a permanent dipole moment to form. This dipole moment arises due to the displacement of charged ions from their equilibrium positions, creating a separation of positive and negative charges, leading to an electrical polarization. Generally, interaction of permanent dipoles with each other can produce ferroelectricity or even more exotic states, such as multiferroicity, where the material exhibits both ferromagnetism and ferroelectricity[2]. As mentioned before, M-type hexaferrites are a type of magnetic material that exhibits high $T_C$ ferromagnetism, which is why they are widely used in various industrial applications[3] such as magnetic recording media and microwave devices. The synthesis of hexaferrites has been thoroughly documented, making them easy to produce and modify, with various atomic substitutions being possible due to their large unit cell and the presence of many atoms in the hexaferrite unit cell [1]. The possibility of ferroelectricity in hexaferrites and their easy synthesis have made them a hot topic of research. The ultimate goal is to develop a high $T_C$ multiferroic material that can exhibit both ferromagnetism and ferroelectricity at a high temperature, which would be useful in various technological applications. However, achieving high $T_C$ multiferroicity is a challenging task due to the complexity of the underlying physics and materials synthesis. Nevertheless, the potential for achieving high $T_C$ multiferroicity is further boosted by the fact that the large unit cell and the presence of many atoms in hexaferrite structures provide a rich playground for

[1]Other sites have similar bond lengths to Fe-O in-plane, differing up to 0.1 Angstroms.

[2]General definition is any, two or more, simultaneous ferroic orders, not necessarily the two mentioned.

[3]Not just because of high $T_C$ but some other factors such as high magnetocrystalline anisotropy.

the exploration of various atomic substitutions that could potentially yield a high $T_C$ multiferroic material.

Independently from topic of multiferroicity, the position of iron atoms in $BaFe_{12}O_{19}$ 2b site has been a topic of research. Historically, Neutron diffraction revealed that the iron atoms in $BaFe_{12}O_{19}$ shift towards one of the apical oxygen atoms at room temperature by 0.26 Å and freeze in the equatorial plane at 4.2 K [50]. This finding was supported by phonon spectrum calculations [51]. Dielectric measurements showed that the dielectric function of $BaFe_{12}O_{19}$ follows the Barrett formula, indicating quantum paraelectric behavior from room temperature down to 2 K, which is possibly due to the polar distortion of the bi-pyramidal sites [52, 53]. However, this contradicts the neutron diffraction results, suggesting antiferroelectric interactions. The triangular structure of the bi-pyramidal sites fulfills the conditions for the electric dipole liquid. A recent study on (Ba,Pb)Fe12O19 with (Ba, Pb) partial chemical substitution found slow relaxational excitations in both dielectric and magnetic behavior, with shared mean relaxation times and activation energy. This behavior suggests a magnetoelectric effect in M-type hexaferrites, where bi-pyramidal iron sites may couple spin and electric dipoles. It remains unclear whether this behavior is specific to a certain composition or can be generalized to a wider range of substitutions. Nevertheless, subsequent work on Pb-substituted $Ba_{1-x}Pbx Fe_{12}O_{19}$ showed that Pb incorporation has a pronounced impact on the broadband dielectric and terahertz response and pointed to an important role of $Fe^{2+}$-related electronic excitations in this modified electrodynamics. These results suggest that Pb substitution may influence M-type hexaferrites on several interconnected levels, affecting not only relaxational and magnetoelectric behavior but also the balance of Fe valence states that participate in the low-energy response [7, 54].

## 2.5 Crystal and synthesis description

In order to ensure the reliability of experimental results, it is essential to minimize the effects of extrinsic factors that can influence the behavior of materials. In the case of polycrystalline samples, the presence of grain boundaries, defects, impurities, and other non-uniformities can introduce variability in measurements, making it difficult to draw meaningful conclusions about the intrinsic properties of the material [55].

To overcome this limitation, single crystals of barium hexaferrite with high structural and chemical homogeneity were employed in this study [7, 56, 57]. By using single crystals, the effects of grain boundaries and other micro-structural features were eliminated, allowing for a more precise characterization of the intrinsic properties of the material. The specific compounds used in this study, $Ba_{0.3}Pb_{0.7}Fe_{12}O_{19}$, $Ba_{0.2}Pb_{0.8}Fe_{10.8}Al_{1.2}O_{19}$, and $Ba_{0.2}Pb_{0.8}Fe_{8.7}Al_{3.3}O_{19}$ (from now on Al0,Al1 and Al3 respectively), were selected based on their relevance to the research question and

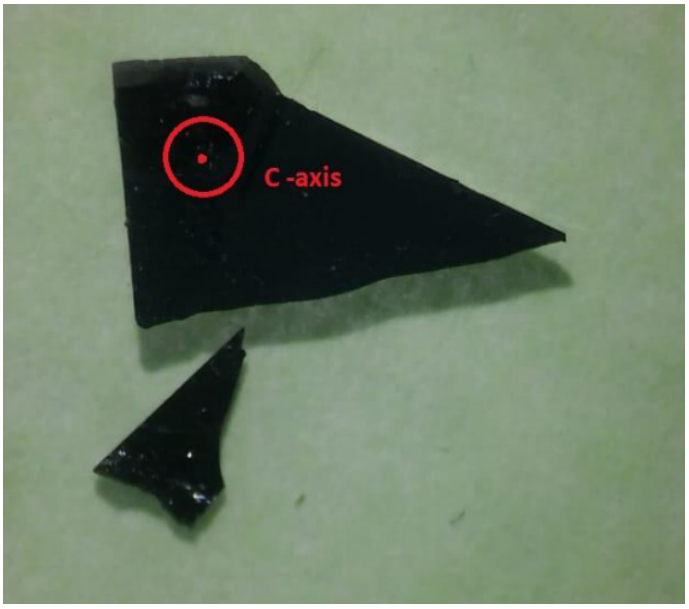


Figure 2.3: Hexaferrite samples under microscope with crystallographic c direction indicated.

their known properties [7, 56, 57]. The crystals were grown using a flux technique, which involves the use of a molten salt as a medium for crystal growth. This method allows for a controlled and gradual cooling of the melt, which promotes the formation of large and well-defined crystals [55]. The temperature of the resistive furnace was precisely controlled to ensure that the crystals were grown under optimal conditions. The starting materials for crystal growth, including iron, aluminum, lead oxides, and barium carbonate, were carefully selected to ensure their purity and homogeneity. We did not synthesize these crystals ourselves, they were grown by our collaborators and obtained through that collaboration, with details provided in Refs. [7, 55–57].

Overall, the use of high-quality single crystals grown under controlled conditions represents a critical step towards achieving a more accurate understanding of the intrinsic properties of complex materials such as barium hexaferrite own properties [55–57]. Above mentioned three different materials (Al0,Al1,Al3) with varying concentrations of aluminum were used to investigate the effects of aluminum substitution on the ferrimagnetic order. The results of the study showed that the introduction of aluminum gradually destroys the ferrimagnetic order in the materials. Interestingly, separate publication [8] suggests that the use of the aluminum substitution could enable the creation of a true ferroelectric state. As a result, the three different concentrations of aluminum were selected for use in this study to further explore the potential for the creation of a ferroelectric state.

Figure 2.3 displays a typical crystal. All of the samples are black, opaque crystals. Crystallographic directions were determined by single crystal X-ray diffraction.

In the previous chapter the theoretical basis was established. Building on it, the present chapter has defined the crystal structure, physical properties, and synthesis of (Ba,Pb)(Fe,Al)$_{12}$O$_{19}$ single crystals, which were investigated in this thesis. To finalize the framework of this thesis, in the next chapter experimental methods used to characterize these samples and to test the predictions drawn from the theory are described in detail.

# Chapter 3

# Experimental techniques

This chapter provides an overview of the experimental techniques employed to study the magnetic, electronic, and structural properties of materials. AC susceptibility is introduced as a tool to probe magnetic relaxation and dynamic phenomena by applying oscillating fields and analyzing the material's frequency-dependent response. DC resistivity measurements are discussed for their role in characterizing the electronic transport properties and temperature-dependent resistivity of materials. Dielectric spectroscopy was employed as a method to investigate electric susceptibility and dynamic charge ordering. Finally, X-ray absorption spectroscopy (XAS) and resonant inelastic X-ray scattering (RIXS) are described as synchrotron-based techniques that reveal microscopic electronic and magnetic structures through the interaction of X-rays with core-level electrons. These techniques collectively provide a comprehensive approach to understanding the multifaceted properties of materials.

Alongside the description of these techniques, the chapter discusses the underlying physical principles they detect, such as magnetic relaxation, charge ordering, and electronic transitions, highlighting their associated phenomenology. The advantages and limitations of each technique are discussed, providing insight into their optimal applications and constraints. Additionally, the experimental realizations of these methods, including the commercial and custom-built setups available in the lab, are detailed for completeness.

## 3.1 AC susceptibility

### 3.1.1 Theory of operation

In investigations of magnetism, direct-current (DC) and alternating-current (AC) susceptibility measurements are used to characterize the response of materials under different conditions. In DC susceptibility measurements, a constant field is applied while magnetization is recorded as a function of field strength and other parameters, such as temperature. These measurements provide key magnetic quantities, including phase-transition temperatures, magnetization values, and coercivity. In contrast, AC susceptibility measurements introduce a time-dependent field at various frequencies, providing access to relaxation processes and spin dynamics. DC methods probe materials in equilibrium, whereas AC methods investigate deviations from equilibrium, thus producing complementary information that is used in the analysis of magnetic systems. In this thesis, we used AC susceptibility as a probe of relaxation phenomena in M-type hexaferrites[27, 28].

Magnetic susceptibility can be defined in several ways. One common definition is given by the ratio of magnetization $M(H, T, \ldots)$ to the applied magnetic field $H$:

$$\chi = \frac{M(H, T, \ldots)}{H}, \tag{3.1}$$

where $M$ is the magnetization, $H$ is the applied field, and $T$ is the temperature [28]. Sometimes, a so-called differential susceptibility is more useful:

$$\chi_{\text{diff}} = \frac{\partial M}{\partial H}. \tag{3.2}$$

These two definitions are relevant for both DC and AC measurements, though practical factors must be considered in real-world experiments [9, 28].

DC susceptibility experiments typically measure the linear response, where magnetization $M$ is proportional to the applied field $H$. As the field amplitude increases, the system can enter a non-linear regime in which $M$ is no longer proportional to $H$, and higher-order susceptibilities contribute ( $M = \chi H + \chi_3 H^3 + \ldots$ ). This transition complicates data interpretation because measurements no longer isolate the linear response. Under sufficiently large fields, magnetization may approach saturation and show little further increase with $H$. Additionally, DC susceptibility is not sensitive to phenomena occurring on short timescales, since it primarily probes the equilibrium state of the system [26–28].

In contrast, AC susceptibility measurements use a small oscillating AC field superimposed on a constant DC field. The small AC field serves as a probe to evaluate the susceptibility at specific points along the magnetization versus applied field curve. By varying the DC field, one can effectively "explore" different regions of the magnetization curve, as illustrated in Figure 3.1. This method provides assessment

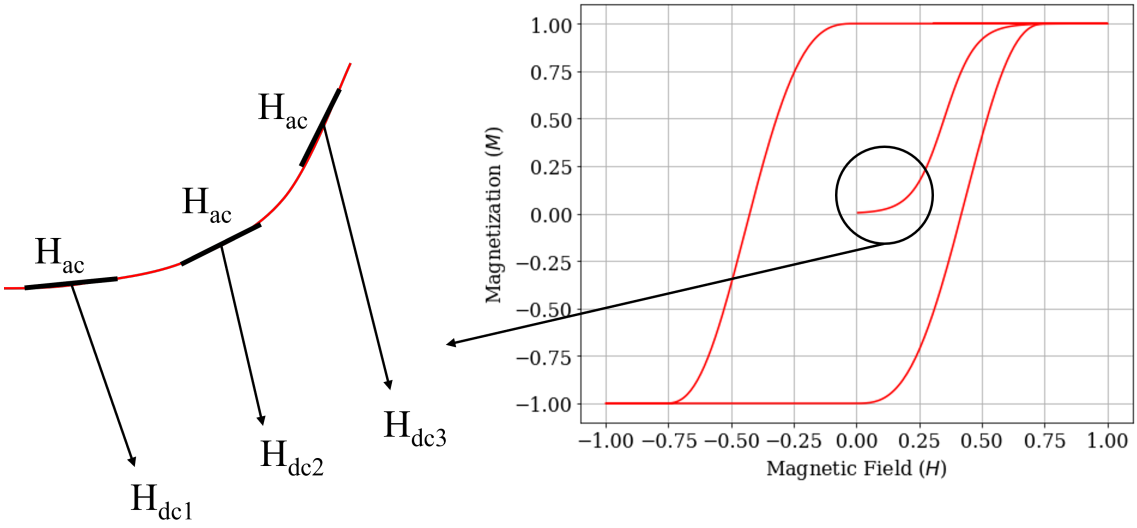


Figure 3.1: Illustration of the magnetization $M$ versus magnetic field $H$ loop ($M$-$H$ loop). The diagram shows how does the interplay between small AC fields $H_{\mathrm{AC}}$ and different DC bias fields ($H_{\mathrm{DC1}}$, $H_{\mathrm{DC2}}$, $H_{\mathrm{DC3}}$) determine AC susceptibility, slope of the black line, at specific points on the M-H curve.

of the magnetic response at a particular bias field, making it particularly suitable for studying systems where susceptibility depends on the applied field strength[27, 28]. The slope of the magnetization curve provides an approximate but incomplete representation of the AC susceptibility and serves primarily as a demonstrative tool. The accurate determination of AC susceptibility at a given point involves the Fourier transform of the response, which can be visualized as an ellipse, where the slope corresponds to the real part of the transform and the openness of the ellipse represents the imaginary part. For a more in-depth discussion on the AC susceptibility refer to the paper [58].

The expression for AC susceptibility is obtained in the following way. Time dependent magnetic field is applied of the form

$$H(t) = H_{\mathrm{DC}} + H_{\mathrm{AC}} \cos \omega t \tag{3.3}$$

where $H_{\mathrm{DC}}$ and $H_{\mathrm{AC}}$ are amplitudes of the static and alternating magnetic field respectively while $\omega$ is the angular frequency and $t$ is the time. The response and the applied field (Equation 3.3) generally does not need to be in phase. This argument in linear approximation produces time dependent response of the magnetization of the following form,

$$\begin{aligned} M(t) &= M_{\mathrm{DC}} + M_{\mathrm{AC}} \cos\left(\omega t + \theta\right) \\ &= M_{\mathrm{DC}} + M_{\mathrm{AC}} \cos(\omega t) \cos\left(\theta\right) + M_{\mathrm{AC}} \sin(\omega t) \sin\left(\theta\right) \end{aligned} \tag{3.4}$$

where $M_{\mathrm{DC}}$ and $M_{\mathrm{AC}}$ are amplitudes of the static and alternating magnetization respectively while the $\theta$ is the phase lag between applied field and the response.

The definition of the AC susceptibility follows

$$M(t) = M_{\mathrm{DC}} + \chi' H_{\mathrm{AC}} \cos(\omega t) + \chi'' H_{\mathrm{AC}} \sin(\omega t) \tag{3.5}$$

where the in-phase part $\chi'$ and out-of-phase part $\chi''$ of AC susceptibility by Equation 3.4 are equal to

$$\chi' = \frac{M_{\mathrm{AC}} \cos(\theta)}{H_{\mathrm{AC}}} \qquad\qquad \chi'' = \frac{M_{\mathrm{AC}} \sin(\theta)}{H_{\mathrm{AC}}}. \tag{3.6}$$

The in-phase part of AC susceptibility is also called the real part while the out-of-phase part is usually called the imaginary part. The conventional way of defining AC susceptibility is the

$$\chi_{\mathrm{AC}}(\omega) = \chi'(\omega) - i\chi''(\omega) \tag{3.7}$$

where $\chi_{\mathrm{AC}}$ is the AC susceptibility, with explicit dependence on frequency.

It is worth noting a few things about the AC susceptibility and the derivation above. First is that the $\chi''$ is sometimes called magnetic absorption, which is because the only energy absorption is happening when the $\chi''$ is non-zero (this follows from the equation for the energy density absorbed per time given by $W \propto \int\limits_{cycle} H dM$ ) [26]. Second is the assumed linear response in the Equation 3.4 which is special case in materials. A more general type of response (which includes the nonlinear response) is of the form

$$M(t) = M_{\mathrm{DC}} + H_{\mathrm{AC}} \sum_n \left(\chi'_n \cos(n\omega t) + \chi''_n \sin(n\omega t)\right) \tag{3.8}$$

where $n$ is the $n$-th harmonic of the magnetization with respect to the driving harmonic (oscillatory part of the applied magnetic field in Equation 3.7). These harmonics are experimentally available by direct measurements of AC susceptibility. The direct measurement of AC susceptibility is typically performed as follows: the measurement point is first selected on the magnetization versus applied field curve by applying an appropriate DC bias field, as previously discussed and shown in Figure 3.1. Once positioned, the AC susceptibility is measured using an oscillatory magnetic field. However, if the amplitude of the applied AC field is not sufficiently small—such as in the non-linear regime near a phase transition where the correlation length diverges—the assumption of linear response may no longer hold. In such cases, the linear response can still be extracted, but this requires additional analysis. Extracting the linear response from experimental data involves processing the Fourier components obtained through measurements of higher harmonics, as described in Equation 3.8. These Fourier components must be converted into the Taylor expansion components $M(H) = \sum\limits_n \chi_n H_{\mathrm{AC}}^n$. Although this process is not used in this thesis the reader is pointed to reference [58], which discusses these techniques along with other aspects of AC susceptibility measurements. For a broader overview of these challenges and methods, see also [26–28].

### 3.1.2 Experimental setup

Conventional way of AC susceptibility experimental design is shown on Figure 3.2. There are 4 distinct sets of coils[1]. First we have DC and AC coil which excite the sample. The DC coil can be separated into two separate coils for precise field adjustments e.g. superconducting coil for large field and a normal non-superconducting coil for small precise field production. Then there are measuring coils (pick-up coils) which are used to detect the magnetic signal generated by the sample in response to the applied oscillating magnetic field. The sample's response induces a voltage in the measuring coil. This induced voltage is directly related to the sample's magnetic susceptibility and can be analyzed to extract the real and imaginary components of the AC susceptibility. However, background signals often generate significant bias, which can either mask the sample's signal within the measuring range or reduce the precision of the measurement. To address this issue, a second coil, referred to as the compensating coil, is introduced. The compensating coil is positioned such that it experiences the same background[2] as the measuring coil, allowing it to effectively cancel out the background signal and isolate the response from the sample.

Mathematically this can be expressed in the following way: On the coils electromotive force (EMF) is measured which generally equates to

$$\begin{aligned} \xi_1 &= -\frac{d\phi_{B1}}{dt} \propto \frac{dB}{dt} \propto \frac{d(H+M)}{dt} \\ \xi_2 &= -\frac{d\phi_{B2}}{dt} \propto \frac{dH}{dt} \end{aligned} \tag{3.9}$$

where $\xi_1$ and $\xi_2$ are the EMFs from the measuring and compensating coil respectively, $\phi_B$ is the magnetic flux, $B$ is the magnetic field density (better to call it magnetic field inside the sample), $H$ the applied magnetic field (if we call $B$ the magnetic field then $H$ is the auxiliary field as per reference [59]) of the form Equation 3.3 and $M$ is magnetization of the sample, and finally $t$ is time. The proportionalities in Equation 3.9 highlight the specific dependencies of each EMF. Without these proportionalities, both EMFs would share the same area factor. Measuring the difference of the EMFs one obtains the following expression

$$\xi_1 - \xi_2 = V \propto \frac{dM}{dt} \tag{3.10}$$

where $V$ now indicates the measured voltage. This expression equates to

$$V \propto \frac{dM}{dt} = \frac{dM}{dH}\frac{dH}{dt} \propto \chi_{\mathrm{AC}}(\omega)\omega \tag{3.11}$$

[1]The system of coils can be conceptually visualized as resembling the layers of an onion, with each layer serving a distinct function.

[2]The background refers to the response of all components other than the sample itself. These components typically include the sample holder, wiring, heater, and any other materials or elements present within the experimental setup that may contribute to the measured signal.

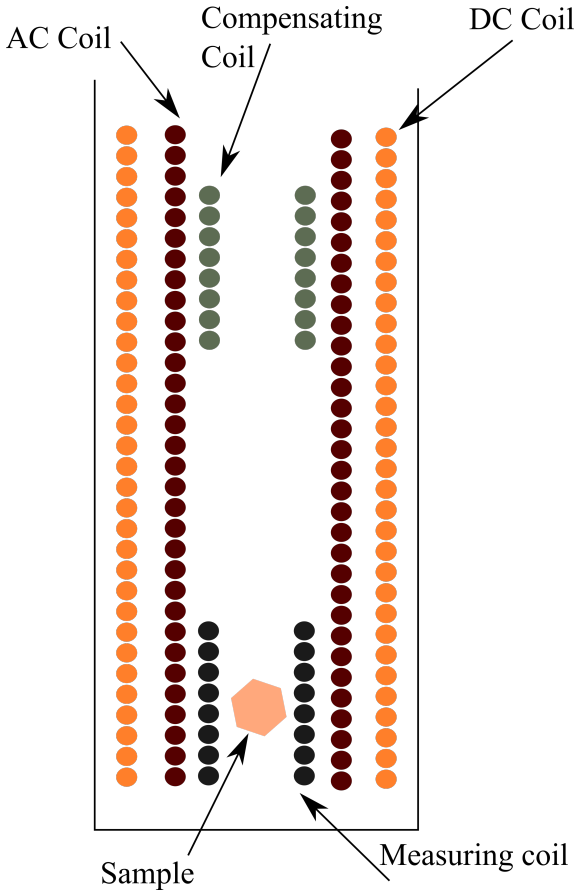


Figure 3.2: Experimental design / coil configuration of the AC susceptometer. In practice sample is in thermally and atmospherically isolated from the coils so that temperature control of the sample does not disturb the coils.

where the last proportionality is just the amplitude of the measured signal (time dependence is not measured, but rather just the amplitudes of the harmonics), the $\omega$ is the angular frequency of the driving field and $\chi_{\mathrm{AC}}(\omega)$ is the AC susceptibility which is obtained using Equation 3.2. As a final note on this derivation: we can have more than one magnetization contribution, for example the sample holder can also produce magnetization. Contribution from this non-sample magnetization (sample holder) should be homogeneous through both measuring and compensating coil, as much as possible, for the reasons of compensation, so that this magnetization part appears in both EMFs with same value/time dependence and therefore cancels out.

For this dissertation two different setups for AC measurements were used. First is a commercially available CryoBIND susceptometer [60] (left panel in Figure 3.3) and a homemade version of susceptometer (right panel in Figure 3.3). These two measuring systems are similar, the differences lie in the cryostat, the overall shape and probably most important the homemade setup has superconducting coil which can produce DC fields up to 9 T. On the instrument rack (Cabinets with instruments on Figure 3.3), two arguably most important pieces of electronic equipment in this


Figure 3.3: AC susceptibility measuring systems. Left is the CryoBIND, while right is the homemade system.

type of measurement are the current source that drives the small AC coil and the lock-in amplifier. The current source is important because it sets the current, which needs to be low-noise and stable. Additionally the current source needs to have the ability to produce oscillating signals in frequency domain which need to be large enough to see the effect. Lock-in amplifier on the other hand is the instrument which reads the small induced voltage on the sample, and for this reason in needs to be very precise and not noisy. One of the most important parameters in the lock-in amplifier is the phase resolution, which is a measure of the lowest detectable phase difference, which is used to separate real and imaginary part of AC susceptibility. Current source used was the Keithley K6221 [61] while the lock-in amplifier is the Signal Recovery 7265 [62] in both AC susceptibility measuring systems.

### 3.1.3 AC susceptibility and relevant physical phenomena

In the preceding sections, we briefly discussed the physical phenomena detectable through AC susceptibility measurements. AC susceptibility provides valuable insights into a variety of (primarily) magnetic systems and can yield information for understanding specific properties of these systems. Notable examples include studies of single-molecule magnets and quasi-low-dimensional magnets. However, the focus of this thesis is on two specific phenomena: superparamagnetic relaxation and domain wall dynamics. Accordingly, the following subsections will explore how AC susceptibility can be used to investigate these phenomena. For a comprehensive overview of the range of physical phenomena detectable by AC susceptibility, references [26–28] are recommended.

#### Domain Wall Dynamics

The separating region between two differently oriented domains (e.g., neighboring domains with opposite directions of magnetization) is referred to as a domain wall. Domain walls are transitional regions where the magnetization gradually shifts orientation from one domain to the next, as discussed in Section 1.1.3.

The dynamics of domain walls in ferro- and ferrimagnets are closely tied to magnetic relaxation processes, where the spin system exchanges energy with the lattice via spin-lattice relaxation. This relaxation mechanism, mediated by spin-orbit interactions, allows energy transfer between the magnetic spins and the lattice vibrations (Section 1.1.4). When a magnetic field is applied, it promotes the growth of domains aligned with the field at the expense of others, leading to domain wall displacement. An oscillating (AC) magnetic field further induces oscillatory motion of the domain wall, which can be modeled as a damped harmonic oscillator:

$$m\ddot{x} + \beta\dot{x} + \alpha x = 2M_{\mathrm{S}}He^{i\omega t} \tag{3.12}$$

Here, $m$ represents the effective mass of the wall, $x$ is the domain wall displacement, $\beta$ is the damping parameter, $\alpha$ is the stiffness parameter, $M_{\mathrm{S}}$ is the saturation magnetization, and $He^{i\omega t}$ is the oscillating magnetic field. Depending on the relationship between these parameters, the system exhibits either resonant behavior (underdamped motion, $\beta < 2\sqrt{\alpha m}$) or relaxational behavior (overdamped motion, $\beta > 2\sqrt{\alpha m}$). The relaxation time $\tau = \frac{\beta}{\alpha}$, which is often temperature-dependent, plays a key role in the relaxation processes explored in Section 1.1.4. The stiffness parameter, $\alpha = 2K/d$, depends on the anisotropy constant $K$ and the domain wall width $d$, which is given by:

$$d = \left(\frac{2JS^2}{Ka}\right)^{\frac{1}{2}} \tag{3.13}$$

where $J$ is the exchange interaction constant, $S$ is the spin, and $a$ is the lattice parameter (assuming a simple cubic lattice) [27, 29]. Experimentally, the dynam-

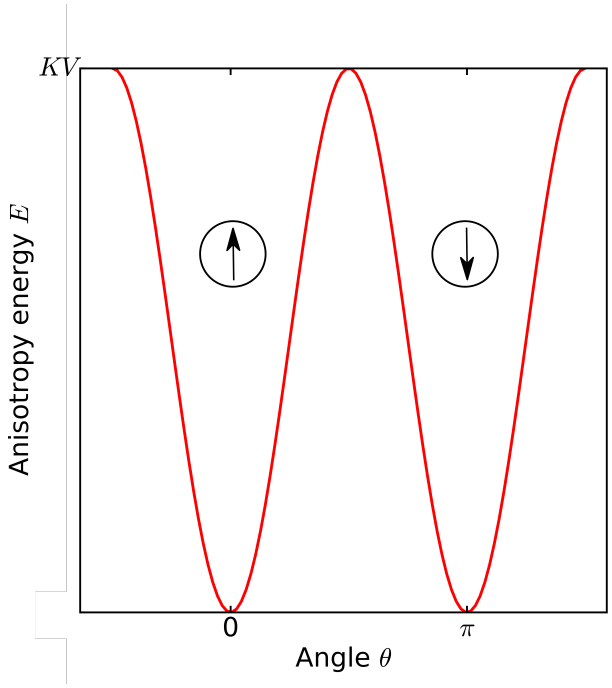


Figure 3.4: Anisotropy energy $E$ as a function of angle $\theta$ with respect to uniaxial direction.

ics of domain walls are often characterized through their contribution to magnetic susceptibility. The domain wall susceptibility, $\chi_{\mathrm{w}}$, is expressed as:

$$\chi_w = \frac{2M_s^2 d_w}{KL}, \tag{3.14}$$

where $M_s$ is the saturation magnetization, $d_w$ is the domain wall width, $K$ is the anisotropy constant, and $L$ is the distance between two domains. This equation connects microscopic properties, such as the domain wall width and anisotropy constant, with macroscopic measurements of frequency-dependent susceptibility. Specifically, $\chi_{\mathrm{w}}$ corresponds to the relaxation strength ($\Delta\chi$) described in the Cole-Cole model (Section 1.4.2) and is given by $\chi_{\mathrm{w}} = \chi_T - \chi_S$, where $\chi_T$ and $\chi_S$ are the isothermal and adiabatic susceptibilities, respectively [10, 26–28, 63, 64].

In this thesis, we observed behavior consistent with the slowing down of domain wall dynamics. This phenomenon, characterized by an increase in the relaxation time $\tau$ as described by the Cole-Cole model, was observed with decreasing temperature. The temperature dependence of this slowing down followed an Arrhenius behavior $\tau(T) \propto e^{\frac{E_{\mathrm{a}}}{kT}}$, enabling the determination of the energy scale $E_{\mathrm{a}}$ associated with the process.

### Single domain system

Single-domain particles are magnetic particles in which the entire volume is uniformly magnetized, with no internal domain structure. The dynamics of these sys-

tems are governed by the interplay between thermal energy and anisotropy energy, which determines the direction and stability of their magnetization. For a particle with uniaxial anisotropy, the energy governing the direction of magnetization takes the following form:

$$E = KV \sin^2 \theta, \tag{3.15}$$

where $K$ is the anisotropy energy density, $V$ is the volume of the particle, and $\theta$ is the angle between the magnetization vector and the uniaxial anisotropy axis, as illustrated in Figure 3.4. From this relationship, it is evident that there are two energy minima ($\theta = 0$ and $\theta = \pi$), separated by an energy barrier $KV$. The height of this barrier plays a crucial role in the magnetic behavior of the system [27, 28].

For temperatures where the thermal energy $k_B T$ is much greater than the anisotropy barrier ($k_B T \gg KV$), the magnetization can overcome the energy barrier easily, leading to equal occupancy of all angles, regardless of the initial orientation. In contrast, when $k_B T \ll KV$, the system becomes trapped in one of the energy minima, and transitions between them are highly unlikely. At intermediate temperatures, where $k_B T$ is comparable to $KV$, the magnetization alternates between the minima, with a switching frequency that depends exponentially on the ratio of the barrier height to the thermal energy. This behavior can be described using the Arrhenius law:

$$\frac{1}{f}(T) = \frac{1}{f_0} e^{\frac{E_a}{kT}} = \tau(T), \tag{3.16}$$

where $f$ is the frequency of magnetization switching, $f_0$ (or $\tau_0$ in its reciprocal form, so called attempt time or inverse attempt frequency) represents the attempt frequency, and $E_a = KV$ is the energy barrier. The relaxation time $\tau(T)$ provides a convenient measure of the system's response to temperature changes and external fields [9, 27, 28, 65].

This theoretical framework is essential for understanding superparamagnetism, a phenomenon observed in single domain particles such as nanoparticles and molecular magnets. In these systems, the energy barrier originates from either shape anisotropy, magnetocrystalline anisotropy, or spin-orbit coupling effects. For single molecule magnets, the anisotropy stems from quantum mechanical interactions described by effective spin Hamiltonians [27, 28].

As a final note on the superparamagnetic behavior/phenomenology, relevant for this thesis, and its measurement through AC susceptibility, the frequency dependence of susceptibility follows relaxational dynamics, often modeled by the Debye or Cole-Cole models. These models capture the dispersive nature of susceptibility and its connection to the magnetization dynamics (refer to Section 1.4.2) [27, 28].

## 3.2 DC Resistivity

Direct current (DC) resistivity measurements are governed by Ohm's law, expressed as:

$$\mathbf{J} = \sigma \mathbf{E} \tag{3.17}$$

where $\mathbf{J}$ is the current density, $\sigma$ is the conductivity, and $\mathbf{E}$ is the electric field. The conductivity, $\sigma$, is a tensor that, according to Neumann's principle, adheres to the symmetry properties of the crystal structure [59, 66]. In experimental practice, measurements do not directly involve electric fields and current densities. Instead, voltage ($U$) and current ($I$) are measured, relating to resistance ($R$) through the macroscopic Ohm's law $I = U/R$. The connection between Equation 3.17 and the macroscopic form of Ohm's law incorporates geometry of the sample. By introducing the sample length ($l$) and cross-sectional area ($A$), the resistance can be expressed as:

$$R = \frac{\rho l}{A} \tag{3.18}$$

where resistivity, $\rho$, is defined as the reciprocal of conductivity ($\rho = 1/\sigma$). The resistivity is an intrinsic property of the material, and it is generally dependent on external parameters such as temperature and pressure. When measuring the resistance of anisotropic materials, one must carefully consider the alignment of electrodes and sample geometry, as inaccuracies in these can significantly affect the calculated resistivity components, especially in highly anisotropic systems [67].

Resistance and resistivity measurements are typically conducted using either the four-point or two-point configurations, illustrated in Figure 3.5. In the four-point configuration, a current source is used alongside a voltmeter. This method is preferred when the resistance of the sample between the inner contacts is significantly lower than the input resistance of the voltmeter, ensuring accurate measurement of the sample voltage. If the sample resistance approaches the input resistance of the voltmeter, measurement accuracy decreases as the voltmeter interacts with its own circuitry rather than the sample. In cases where the sample resistance is high, the two-point configuration is used. Here, the current is measured while the voltage is applied across the entire circuit. This approach includes contributions from contact and circuit resistances, which in the high resistance regime of the sample should be negligible. The two-point technique yields reliable data only when the sample resistance is much larger than all other resistances in the circuit.

In this study, resistivity was measured using several experimental systems, all adhering to the principles described above. The primary setup consisted of a stainless steel cryostat, depicted in Figure 3.6. The cryostat, equipped with a superconducting magnet capable of generating magnetic fields up to 5 Tesla, enabled precise temperature control using vacuum spaces and integrated heaters. Electrical connections to the sample were established using coaxial cables terminated in BNC inputs,

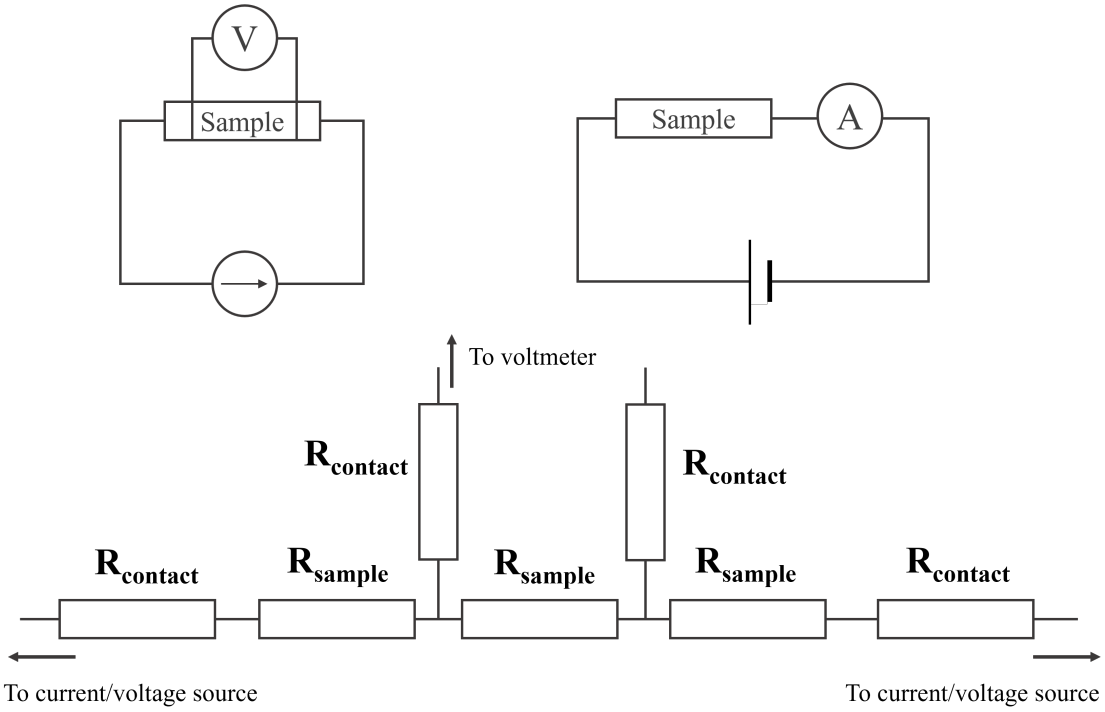


Figure 3.5: Schematic representation of electrical measurement setups and equivalent circuit model. The top panels depict voltage/4-point (left) and current/2-point (right) measurement configurations for a sample. The bottom panel shows the equivalent circuit model for 4-point technique, including contact resistances ($R_{\text{contact}}$) and sample resistances ($R_{\text{sample}}$) in the system.

as shown in Figure 3.6b.

The studied samples exhibited relatively high resistance values ($\sim 1\,\text{M}\Omega\,\text{cm}$). The temperature dependence of resistivity indicated behavior characteristic of semiconducting materials. In a conventional semiconductor, resistivity follows an exponential dependence on temperature as described by the Arrhenius equation:

$$\rho(T) \propto \exp\left(\frac{\Delta}{2kT}\right) \tag{3.19}$$

where $\rho$ is the resistivity, $\Delta$ is the energy gap, $k$ is the Boltzmann constant, and $T$ is the temperature[63]. In addition to conventional thermally activated semiconducting behavior, alternative insulating behaviors were considered. For example, Mott variable-range hopping (VRH) conduction is used at low temperatures where the resistances between neighboring impurities exceed those between distant impurities with energy levels near the Fermi level, resulting in conduction governed by hopping to more distant sites. Mott variable-range hopping in $d$ dimensions (where $d <= 3$) is described by:

$$\rho(T) \propto \exp\left[\left(\frac{T_0}{T}\right)^{1/(d+1)}\right] \tag{3.20}$$

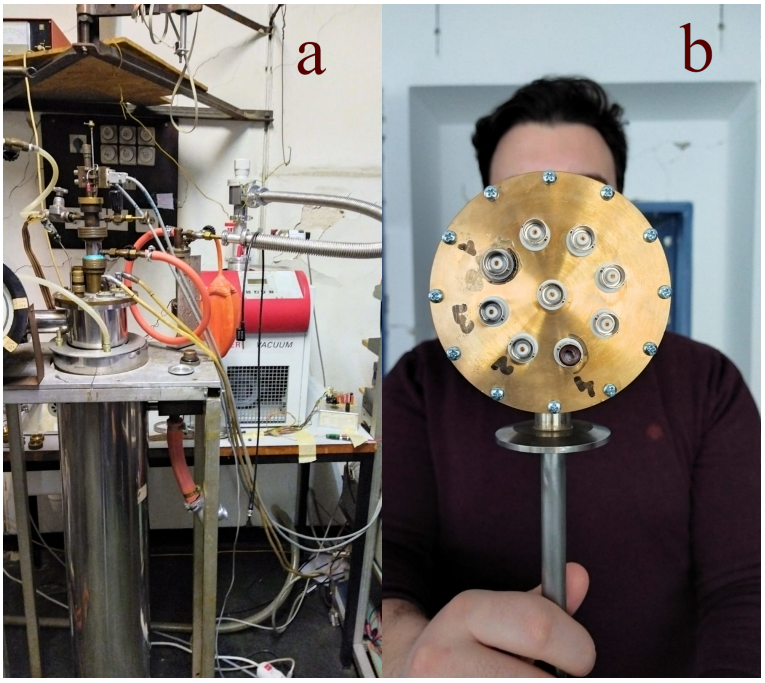


Figure 3.6: Experimental setup: (a) Cryostat environment. (b) Sample holder with BNC inputs.

where $T_0$ is the characteristic temperature determined by the material properties and dimensionality [63, 66, 68, 69].

## 3.3 Dielectric spectroscopy

### 3.3.1 Introduction

Dielectric spectroscopy, often referred to as impedance spectroscopy by electrical engineers[3], is closely analogous to AC magnetic susceptibility. This analogy arises not only from the common frequency dependence of the measured response, but also from the similarity in fundamental electrodynamics, in AC magnetic susceptibility the magnetization responds to a driving magnetic field $M \sim H$, while in dielectric spectroscopy the electric polarization responds to a driving electric field $P \sim E$. The technical methodology also parallels that of AC magnetic susceptibility, utilizing a lock-in amplifier (in an elementary setup) to measure signals at a specific frequency.

Dielectric spectroscopy is a technique employed to measure the dielectric constant or electric susceptibility of a material. The method involves applying a sinusoidal voltage signal and measuring the resulting current through the sample. This approach may appear analogous to the two-point direct current (DC) transport

[3]Electrical engineers call it impedance spectroscopy because they need measurements of impedance while physicists measure dielectric constant/function of a material.

technique; however, the distinction arises from the focus on frequency dependence. This additional parameter enables the investigation of material properties related to dynamic behavior.

To derive the total current through a sample, we begin with the fourth Maxwell equation:

$$\nabla \times \mathbf{H} = \mathbf{J}_{\text{free}} + \frac{\partial \mathbf{D}}{\partial t} \tag{3.21}$$

where $\mathbf{H}$ represents the magnetic field, $\mathbf{J}_{\text{free}}$ is the current density associated with free charge carriers, and $\frac{\partial \mathbf{D}}{\partial t}$ is the time derivative of the displacement field $\mathbf{D}$. By applying Ohm's law,

$$\mathbf{J}_{\text{free}} = \sigma \mathbf{E} \tag{3.22}$$

and the linear response relationship

$$\mathbf{D} = \varepsilon \mathbf{E} \tag{3.23}$$

Equation (3.21) becomes:

$$\nabla \times \mathbf{H} = \sigma \mathbf{E} + \varepsilon \frac{\partial \mathbf{E}}{\partial t} \tag{3.24}$$

where $\varepsilon$ is the absolute permittivity, expressed as:

$$\varepsilon = \varepsilon_0 \varepsilon_r = \varepsilon_0 (1 + \chi_E) \tag{3.25}$$

with $\varepsilon_0$ being the permittivity of free space, $\varepsilon_r$ the relative permittivity (or dielectric function), and $\chi_E$ the electric susceptibility. In the context of dielectric spectroscopy, the electric field is considered to have a periodic dependence, expressed as:

$$\mathbf{E} \propto e^{i\omega t} \tag{3.26}$$

Substituting this into Equation (3.24) results in:

$$\nabla \times \mathbf{H} = (\sigma(\omega) + i\omega \varepsilon_0 \varepsilon_r(\omega))\mathbf{E} \tag{3.27}$$

The expression 3.27 is a generalization of Ohm's law, where the conductivity is now a complex quantity. At zero angular frequency ($\omega = 0$), the equation reduces to the familiar form of Ohm's law used in DC transport measurements. The dielectric function $\varepsilon_r$ is measured through the out-of-phase response of the system to a periodic perturbation.

### 3.3.2 Experimental realization

Impedance analyzers such as the ones used in this thesis (Keysight E4980AL, Agilent 4294A, and HP 4284A [71–73]) follow the measurement principle illustrated in Figure 3.7. The sinusoidal voltage delivered at HCUR (High CURrent) excites the DUT (Device Under Test). The auto-balance loop simultaneously keeps the LCUR (Low

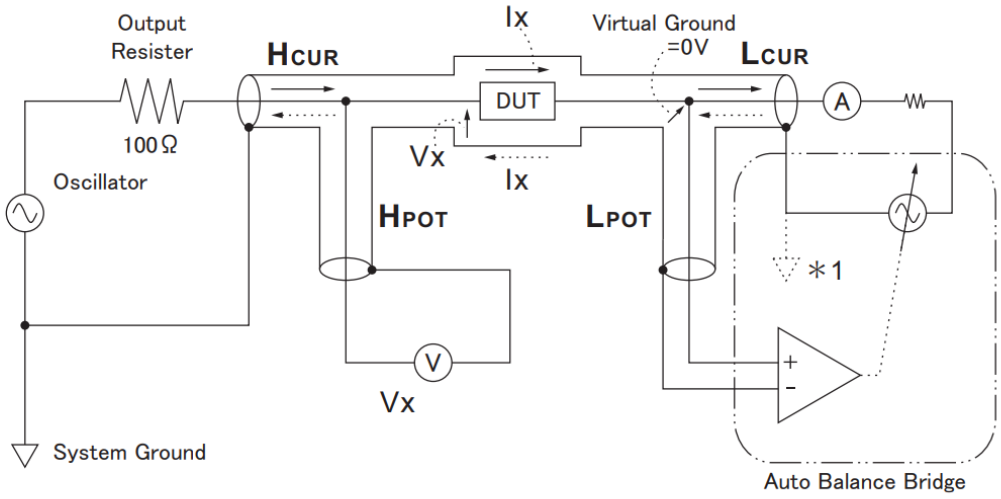


Figure 3.7: Four-terminal-pair auto-balance bridge used in modern impedance analyzers. A sinusoidal source excites the device under test (DUT) through HCUR–LCUR pair inducing current $I_x$. The differential potential across the DUT, $V_x$, is sensed on the high- and low-potential leads (HPOT–LPOT). A feedback amplifier maintains the LCUR node at the reference potential, giving the loop a unity gain over the instrument bandwidth. Adapted from [70].

CURrent) node fixed at the reference potential, ensuring that the measured current is $I_x$ and also it enables for the lock-in detector to sample the differential potential $V_x$ between HPOT (High POTential) and LPOT (Low POTential).

Measured impedance $Z_x$ is calculated by the following equation

$$Z_x(\omega) = \frac{V_x}{I_x} \tag{3.28}$$

where $\omega$ is angular frequency defined by $2\pi f$. Separating the voltage excitation (HCUR–LCUR) from the voltage sensing path (HPOT–LPOT, measuring $V_x$) reduces lead inductance, cable resistance, and connector capacitance to second-order error terms. This is done by virtual ground at LCUR which minimizes parasitic coupling to the shield that could effectively obscure DUT response when long cryostat cables are present, as they were in measurements for this thesis.

There are several complications with this experimental technique with regards to topic of this thesis. Single crystals grown for fundamental solid state physics/material science rarely offer ideal plate geometries. Electrode area is small compared with the separation between contacts, so the intrinsic capacitive component of the DUT is small [74]. Under such circumstances the unavoidable stray capacitance of coaxial leads and connectors may approach or even exceed the specimen value, reducing the signal to background ratio in both $V_x$ and $I_x$. A second

complication originates from the simultaneous detection of DUT's in-phase and out-of phase components. When the real (in-phase) component of the admittance becomes large relative to the out-of-phase component, the fixed phase resolution can be insufficient: the dominant in-phase part of $I_x$ limits the range available for the much smaller out-of-phase part that carries the dielectric response [74].

To mitigate some of the complications few measurement principles are employed. First, the shielded four-terminal leads are kept at the shortest practical length, to keep the stray capacitance as low as possible. Secondly, open/short/load compensations are performed, and all measurements are corrected by them. In the case of measurement where we change the temperature, as in this thesis, the compensations are additionally recorded as a function of temperature. Information on measurement principles can be found in reference [75]. More general treatment of the impedance spectroscopy, its error mechanisms, and interpretation of the measurements may be found in the following references [34, 74].

### 3.3.3 Dielectric spectroscopy data analysis

In dielectric measurements, background effects are inherent to the experimental setup. The background capacitance arises from the physical structure of the setup, including the wiring and sample holder. These elements introduce parasitic capacitances due to their geometric configuration and intrinsic dielectric properties, which remain present even in the absence of a sample. Such effects are an intrinsic characteristic of the apparatus and must be corrected to accurately determine the dielectric properties of the sample.

In order to correct for background effects, the open-circuit admittance, denoted as $Y_{\text{open}}(\omega)$, is subtracted from all measured admittance values $Y(\omega)$[4]. This subtraction eliminates stray capacitances associated with the sample holder construction and cabling.

The dielectric function $\varepsilon(\omega)$, expressed as $\varepsilon'(\omega) - i\varepsilon''(\omega)$, is calculated from the real and imaginary components of the corrected conductivity $Y(\omega) - Y(\omega)_{\text{open}} = G(\omega) + iB(\omega)$. The relations used for this calculation are given as:

$$\varepsilon'(\omega) = 1 + \frac{l}{S}\frac{B(\omega)}{\varepsilon_0 \omega}, \quad \varepsilon''(\omega) = \frac{l}{S}\frac{G(\omega)}{\varepsilon_0 \omega}, \tag{3.29}$$

where $l$ is the sample length, $S$ is the sample cross-sectional area, and $\varepsilon_0$ is the permittivity of free space [40, 76]. Once the dielectric function is obtained, the data is either displayed as a function of temperature to observe its variation or further analyzed through modeling.

[4]One could also perform measurements of closed/short circuit admittance but for this thesis it is not relevant. The procedure is described in Keysight E4980AL manual [76].

Dielectric relaxation for the systems analyzed in this thesis is modeled using a Cole-Cole function, which we described in section 1.4.2:

$$\varepsilon(\omega) - \varepsilon_\infty = \frac{\Delta\varepsilon}{1 + (i\omega\tau)^{1-\alpha}}. \tag{3.30}$$

where $\Delta\varepsilon = \varepsilon(0) - \varepsilon(\infty)$ represents the dielectric relaxation strength, $\tau$ is the mean relaxation time, and $1 - \alpha$ characterizes the broadening of the relaxation time distribution.

As discussed in Section 1.5, dielectric measurements can be affected by extrinsic effects such as Maxwell-Wagner polarization or electrode polarization. Several strategies have been proposed to address these issues [34, 38, 40]. One common approach for single crystal samples involves altering the sample geometry or the electrode contact chemistry and repeating the measurements. Since intrinsic dielectric properties should remain unaffected by these changes, while extrinsic contributions are likely to change, this method enables the separation of intrinsic and extrinsic effects. This approach was employed in the measurements presented in this thesis.

### 3.3.4 Dielectric spectroscopy and phenomenology of charge orderings

Dielectric spectroscopy is a widely utilized technique with applications across different fields, including biological systems, battery technology, device characterization, and the study of glasses, among others [34, 74]. In the context of the phenomena investigated in this thesis, dielectric spectroscopy has two relevant themes. The first is the detection of ordering phenomena of dielectric nature. The second is the investigation of "slowing down" processes, which are indicative of dynamic changes within the system[5].

In charge order, dielectric spectroscopy identifies three elementary types of phase transitions, as illustrated in Figure 3.8 [3]. The first type, the displacive ferroelectric transition (Figure 3.8a), is characterized by a dielectric function with a sharp, non-dispersive peak occurring precisely at the ordering temperature. This peak adheres to the Curie-Weiss law ($\varepsilon \propto (T - T_C)^{-1}$). A notable example of this behavior is observed in the $BaTiO_3$ and multiferroic material $LiCuVO_4$ [63, 77]. Importantly, the peak does not exhibit frequency dependence [3].

The second type, referred to as the order-disorder transition (Figure 3.8b), is marked by a dispersive peak with a single relaxation time. This type of behavior is observed in materials such as organic charge-transfer salts, notably represented by the compound $\kappa$-(BEDT-TTF)$_2$Cu[N(CN)$_2$]Cl [3, 78].

[5]These two themes are interconnected, as they both relate to the phenomenon of charge ordering paired with a slowing down of dynamic processes, commonly referred to as relaxors.

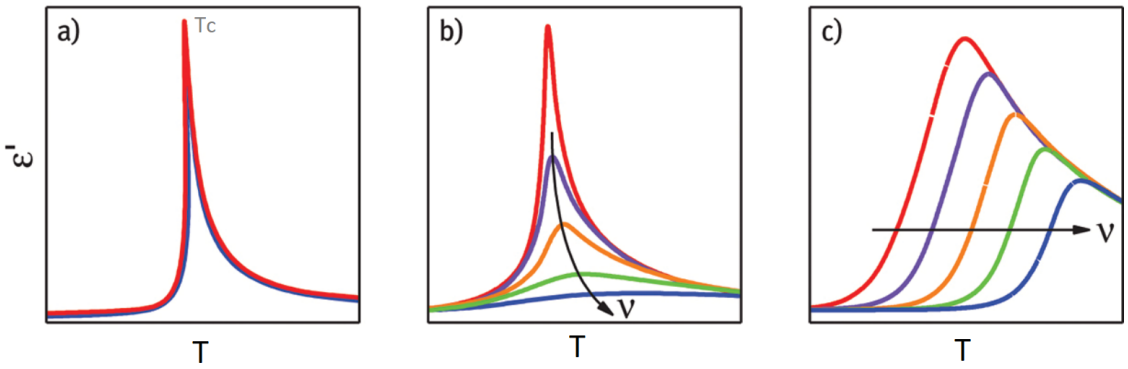


Figure 3.8: Dielectric permittivity as a function of temperature for three types of ferroelectric materials. (a) Displacive ferroelectric with a pronounced peak at the Curie temperature ($T_c$). (b) Order-disorder ferroelectric exhibiting frequency-dependent behavior and a peak at $T_c$. (c) Relaxor ferroelectric characterized by broad peaks that shift with increasing frequency. The curves represent different frequencies, where higher frequencies correspond to higher peak temperatures. Adapted from [3].

The third type of transition, the relaxor ferroelectric (Figure 3.8c), is distinguished by a broad, temperature-dependent relaxation in the dielectric function. In these materials, the peak shifts to higher temperatures as the frequency increases, reflecting the dynamic properties of these materials. Examples of relaxor ferroelectrics include piezoelectric ceramics, which are widely used in industrial applications [79], as well as magnetite ($Fe_3O_4$), which is unexpectedly found to exhibit relaxor-like behavior [80].

Most directly connected to this thesis is the topic of relaxors. The activation phenomena discussed in previous section 2.4 was attributed to relaxor-like behavior. This interpretation will be reexamined in the results section.

## 3.4 X-ray absorption and resonant inelastic X-ray scattering

X-ray absorption spectroscopy (XAS) and resonant inelastic X-ray scattering (RIXS) are synchrotron-based experimental techniques that provide valuable physical and chemical information about materials, such as crystal and electronic structures, magnetism, and more. Experimental methods discussed in earlier sections can be considered "macroscopic" because they measure properties averaged over the entire sample and cannot distinguish contributions from different chemical species, orbitals, or domains of varying orientations. In contrast, XAS and RIXS can resolve many of these microscopic details. Furthermore, the combination of focused X-ray beams, capable

of scanning across the sample surface, and the short wavelength of the photons allows for imaging of multiple physical layers, such as magnetic domains and distinct chemical species [43, 81].

For these techniques, separate sections detailing the relevant physical phenomena and how they appear in XAS and RIXS are not included. This choice is due to the fact that the distortions appear as change of the measured spectra, which is not necessarily unique to a specific phase or phase transition, at least regarding this thesis. Rather than discussing each physical effect separately, focus is given on how these distortions can be modeled and understood through simulation. Specifically, we use crystal field theory (as discussed in Section 1.6) to predict how the XAS or RIXS spectrum responds to different types of structural perturbations. By simulating spectra under varying conditions (e.g. magnetic fields, beam direction ...), we can link particular features in the measured spectra to underlying physical distortions of the sample.

### 3.4.1 X-ray absorption spectroscopy - XAS

In the X-ray absorption process, a core electron[6] is excited by means of highly energetic X-ray photon and is sent to the unoccupied states. The process is shown in Figure 3.9.

The intensity of XAS process is determined by the Fermi's golden rule [41]

$$I_{\mathrm{XAS}} \sim \left|\langle \Phi_{\mathrm{f}} | \hat{e} \cdot r | \Phi_{\mathrm{i}} \rangle\right|^2 \delta_{E_{\mathrm{f}} - E_{\mathrm{i}} - \hbar\omega} \tag{3.31}$$

where $\Phi_{\mathrm{i,f}}$ are the inital and final wave functions, $\hat{e} \cdot r$ is the dipole operator and $\delta_{E_{\mathrm{f}} - E_{\mathrm{i}} - \hbar\omega}$ is the delta function that ensures the conservation of energy in the process. Final state is characterized by a core electron in the excited state, description of which can be viewed as an initial state with continuum electron added ($\epsilon$ - continuum electron creation operator) and core electron removed ($\underline{c}$ - core electron annihilation operator) transforming the equation 3.31 into

$$I_{\mathrm{XAS}} \sim \left|\langle \Phi_{\mathrm{i}} \underline{c} \epsilon | \hat{e} \cdot r | \Phi_{\mathrm{i}} \rangle\right|^2 \delta_{E_{\mathrm{f}} - E_{\mathrm{i}} - \hbar\omega}. \tag{3.32}$$

An important approximation can be made that removes all the electrons that are inactive in the transition. This, together with the summation of different unoccupied state produces

$$I_{\mathrm{XAS}} \sim \left|\langle \epsilon | \hat{e} \cdot r | c \rangle\right|^2 \cdot \rho \tag{3.33}$$

where $\rho$ is the partial density of unoccupied states. According to the dipole selection rules, the density of states must involve a transition with a change in orbital angular momentum ($\Delta L = \pm 1$) while conserving spin ($\Delta S = 0$), as these rules arise from

[6] A electron that occupies low lying energy level e.g. 1s electrons of Oxygen.

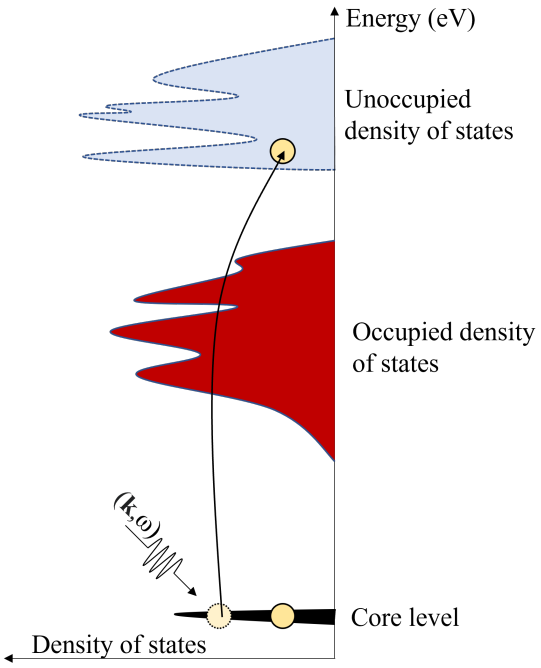


Figure 3.9: Schematic representation of the X-ray absorption spectroscopy (XAS) process. The diagram illustrates the electronic density of states, divided into occupied and unoccupied regions. An incident photon with momentum $\hbar\boldsymbol{k}$ and energy $\hbar\omega$ excites an electron from a core level to an unoccupied state above the Fermi level, leaving a core-level hole behind. This process provides insight into the electronic structure and unoccupied density of states.

the angular momentum carried by the x-ray photon. Higher order transitions are sometimes ignored due to their relatively low intensity [43].

For this thesis measurements of XAS were performed in photon energy range from 690 eV to 730 eV, which corresponds to transitions from core 2p states to 3d continuum states in iron atoms. Measurements were performed at inelastic scattering branch of SEXTANTS beamline in synchrotron SOLEIL [82, 83].

The X-ray photons that illuminate the sample are created in the undulator and subsequently focused and monochromatized using different optical elements. The description and visualisation of the beamline is presented in the reference [83]. The vacuum chamber with the sample is equipped with motors which introduce one rotational and three translational degrees of freedom, which enables measurements of absorption on different position of the sample i.e. make images of samples. Detection of X-ray absorption can then be achieved using two different methods as depicted by Figure 3.10.

Total electron yield is the detection of electrons that are coming from ground that neutralize the sample. The sample is charged due to interaction between X-rays and near-surface electrons, which ejects electrons away from the material. This

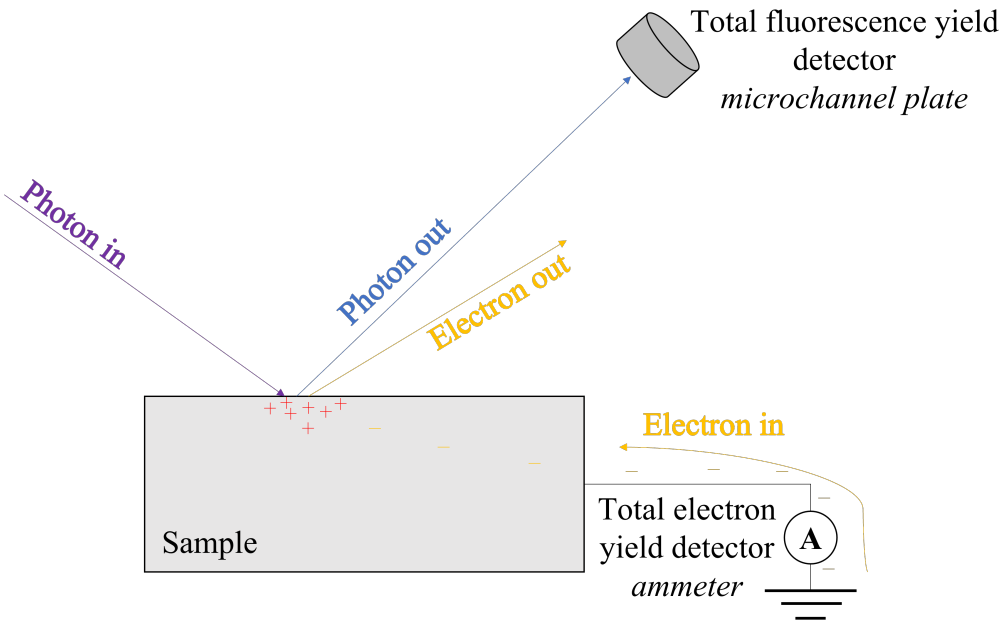


Figure 3.10: Schematic representation of X-ray Absorption Spectroscopy (XAS) measurements utilizing two detection techniques: Total Electron Yield (TEY) and Total Fluorescence Yield (TFY). In the TEY method, the sample absorbs incoming X-ray photons, leading to the emission of electrons. The departure of these electrons leaves the surface positively charged, which is neutralized by an incoming electric current. This current is measured using an ammeter, providing a surface-sensitive signal. In the TFY method, the X-ray photons absorbed by the sample lead to the emission of fluorescent photons, which are detected by a microchannel plate detector, offering a more bulk-sensitive information about the sample than TEY method.

process is surface sensitive (mean probing depth is less then 10 nm) and it depends on the inelastic scattering of Auger electrons [84]. Total fluorescence yield (TFY) on the other hand measures photons that are absorbed and subsequently reemited from the material. Effectively measured photons are created by relaxation of the core hole by an electron (see Figure 3.9). In the soft X-ray region[7], it has been shown that these methods of measuring absorption are not identical (not just by the probing depth which is larger for TFY), for more information check reference [85].

[7]There is no universal boundary between "soft" and "hard" X-rays. In this work we use "soft X-rays" to denote photon energies around the transition-metal $L_{2,3}$ (2p $\rightarrow$ 3d) absorption edges—approximately 400–1000 eV (3d metals). By contrast, "hard X-rays" refers to multi-keV photon energies (e.g. $K$ edges of the 3d metals).

### 3.4.2 Resonant inelastic X-ray scattering - RIXS

The XAS process, which we discussed in the previous section, is a single step process where we indirectly measure the number of events which lead to creation of a core hole. RIXS process on the other hand is at least a two step process. First we create

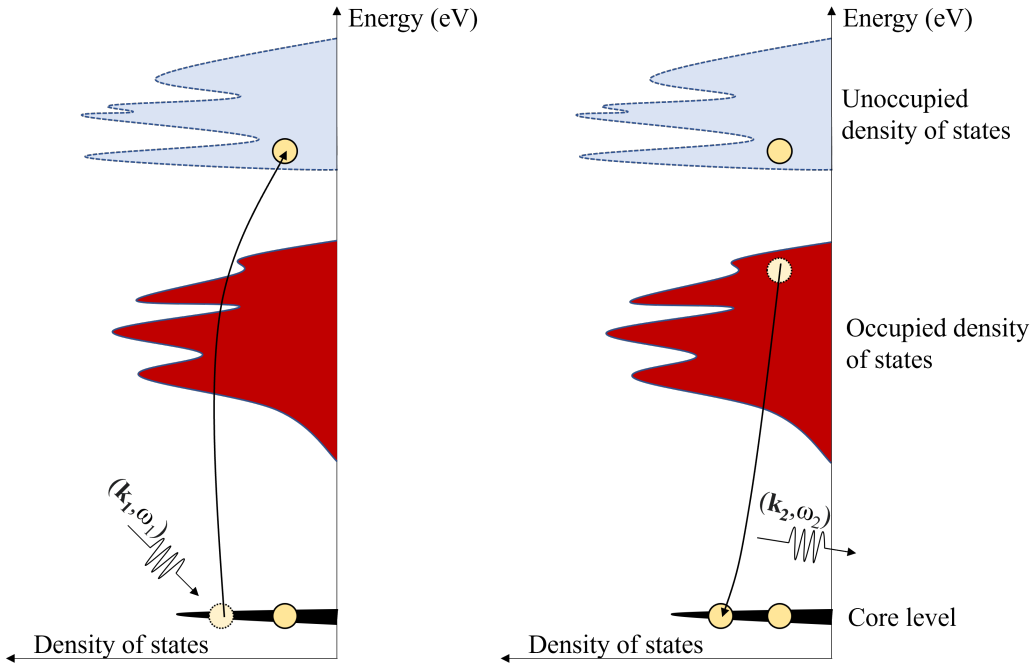


Figure 3.11: Schematic illustration of the direct resonant inelastic X-ray scattering (RIXS) process. In the first step (left), an incident photon with momentum $\hbar\boldsymbol{k}_1$ and energy $\hbar\omega_1$ excites an electron from a core level to an unoccupied electronic state above the Fermi level, creating a core hole. In the second step (right), the electron decays to a lower energy occupied state, emitting a photon with momentum $\hbar\boldsymbol{k}_2$ and energy $\hbar\omega_2$. The energy and momentum differences between the incident and emitted photons provide information about the electronic excitations and density of states in the material.

a core hole, and then we are measuring all the different ways electron can relax[8] this core hole. The RIXS process is shown on Figure 3.11. There are two types of process one direct and one indirect [86, 87]. The direct process is a process when a core hole is filled by the electron from the valence band, leaving behind a electron-hole excitation. The electron hole excitation should have momentum and energy equal to difference between that of initial photon that creates a core-hole and the one that fluoresces due to its annihilation (see Figure 3.11). The indirect process on the other hand is influenced by the intermediate state. The core hole intermediate

[8]Relaxation in a sense that electron fills this empty core state. Not too be confused with relaxations in AC susceptibility or dielectric spectroscopy!

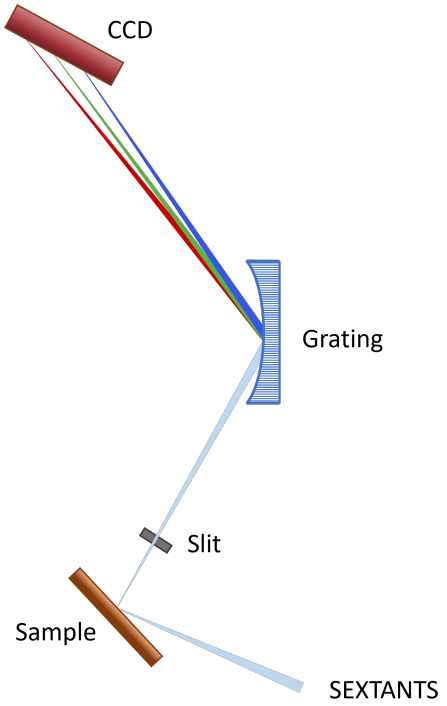


Figure 3.12: Schematic illustration of the Resonant Inelastic X-ray Scattering (RIXS) experimental setup. The incident X-ray beam from SEXTANTS beamline interacts with the sample, and the scattered photons are collected and directed through a slit. The scattered photons are dispersed by a diffraction grating, before being detected by a Charge-Coupled Device (CCD) detector.

state influences valence electrons by a strong potential which then screen the core hole, and in turn get scattered by the potential, creating electron-hole excitations in the valence band which take momentum and energy from the initial excitation.

The experimental environment for XAS and RIXS differ only in the final detector. The final detector is liquid nitrogen cooled CCD which collects photons that are coming from sample which are diffracted by a diffraction grating midway to the CCD. The simplified schematic is shown on Figure 3.12. The exact design and specifications of the spectrometer are published in the reference [88].

### 3.4.3 Simulation of XAS and RIXS intensity

The interpretation of experimental data of XAS and RIXS spectra is done primarily by simulations. These simulations provide insight into the electronic structure and dynamic processes underlying the observed features.

One of the available tools for simulation is Crispy, a graphical user interface for calculation of core-level spectra using the semi-empirical multiplet approaches implemented in Quanty [89, 90]. It is applicable for both XAS and RIXS. Using ligand-field theory and atomic multiplet calculations, Crispy enables modelling of

how the electronic environment, such as ligand coordination and crystal-field splitting, influences the X-ray spectra. Additionally, Crispy supports advanced features, such as spin-orbit coupling and magnetic interactions, allowing for a detailed understanding of magnetic and electronic phenomena in materials. By combining these simulations with experimental data, one can extract detailed information about the material's electronic structure, including orbital occupancy, valence states, and spin configurations [89].

Another approach in modeling is by using tools like FDMNES (Finite Difference Method Near Edge Structure). This is an *ab initio* program which calculates X-ray absorption spectroscopy. FDMNES uses a combination of finite-difference methods and multiple-scattering theory to simulate the interaction of X-rays with the electronic structure of materials. The software allows for the incorporation of various experimental conditions, such as polarization, temperature, and magnetic fields, making it highly versatile for studying complex materials. Furthermore, FDMNES supports calculations for crystalline, amorphous, and disordered systems, providing flexibility for a wide range of research applications [91, 92].

In this thesis, Crispy was primarily used for XAS and RIXS simulations due to its ability to seamlessly simulate both types of data within the same framework. Its integration of ligand field theory and multiplet effects allowed for modeling of the experimental spectra. While FDMNES was also employed to cross-verify the results using its *ab initio* approach, its simulations did not yield results significantly different or noteworthy enough to be included in this thesis.

# Chapter 4

# Results

In this chapter, we explore the magnetic, dielectric, and electronic transport properties, as well as the local electronic structure of Al-substituted M-type hexaferrites. Beginning with AC susceptibility measurements (Section 4.1), we investigate how temperature, frequency and direction of the magnetic field influence relaxation processes, capturing both real and imaginary components of the susceptibility and interpreting them through established theoretical models. Magnetic analysis is complemented by Dielectric Spectroscopy (Section 4.2), where the complex dielectric function is similarly examined to investigate frequency dependent relaxation phenomena and their underlying mechanisms, now in the electric subsystem. Subsequently, we present dc transport measurements (Section 4.3), which offer additional insights into conduction processes.

The last two sections investigate the local structure. X-ray Absorption Spectroscopy (XAS, Section 4.4) provides insights into the local environment and electronic states. Resonant Inelastic X-ray Spectroscopy (RIXS, Section 4.5) then offers a more detailed view of the low-energy excitations and orbital configurations, providing more insights into subtleties not fully captured by XAS alone. Data for both techniques are analyzed using ligand field simulations. The simulations were done using Crispy[89], while the simulation parameters were taken/adapted from [93, 94]. Taken together these techniques reveal a complex behavior of hexaferrite samples across various energy scales and subsystems.

## 4.1 AC Susceptibility

AC susceptibility measurements were performed on three samples with varying aluminum compositions: $Ba_{0.3}Pb_{0.7}Fe_{12}O_{19}$ (Al0), $Ba_{0.2}Pb_{0.8}Fe_{10.8}Al_{1.2}O_{19}$ (Al1), and $Ba_{0.2}Pb_{0.8}Fe_{8.7}Al_{3.3}O_{19}$ (Al3). Measurements were performed at AC magnetic field amplitudes of 25 and 100 mOe, temperatures from 4.2 K to 400 K, and frequencies ranging from 11 Hz to 11,111 Hz. Data reveal temperature and frequency dependent susceptibility changes characteristic of relaxation processes. Amplitudes of magnetic field have been chosen in such a way to avoid the non-linear response observed above about 100 mOe while maximizing the signal-to-noise ratio (See Appendix A.1).

The real and imaginary components of AC susceptibility for the samples are shown in Figure 4.1. Columns represent Al0, Al1, and Al3 (left to right), with real (top row) and imaginary (bottom row) components of susceptibility. Different colors represent different frequencies with arrows displaying the direction of increasing frequency. Temperature dependent dispersion in AC susceptibility was observed:

- **Al0:** Dispersion occurs between 20 K and 120 K. Both real and imaginary parts exhibit a dispersion. Real part of susceptibility, displays step-like behavior from low-temperature low susceptibility value to high temperature high susceptibility value. Imaginary part of susceptibility has a maxima that shift toward higher temperatures with increasing frequency.

- **Al1:** Similar trends to Al0, but shifted to higher temperatures, with dispersive features occurring between 50 K and 220 K.

- **Al3:** Displays frequency dispersion but with pronounced maxima in both real and imaginary parts. The frequency dispersion is narrow compared to the first two samples. The peaks of both real and imaginary part of susceptibility shift toward high temperatures with increasing frequency.

To quantify these observations, frequency spectra were analyzed at fixed temperatures. Figure 4.2 presents frequency-dependent susceptibility for sample Al1 at temperatures of 110 K, 120 K, and 130 K, modeled using the Cole-Cole expression:

$$\chi(\omega) = \chi_\infty + \frac{\chi_0 - \chi_\infty}{1 + (i\omega\tau)^{1-\alpha}}, \tag{4.1}$$

where $\tau$ is the mean relaxation time, $\alpha$ is the broadening parameter[1], and $\Delta\chi = \chi_0 - \chi_\infty$ (Section 1.4.2). The real and imaginary parts of the model closely match the experimental data, confirming the presence of a relaxation process, with a distribution of relaxation times. This model was applied to the temperature range of the dispersion for samples Al0 and Al1.

[1]The $1 - \alpha$ parameter we dub broadening as in Figure 4.3.

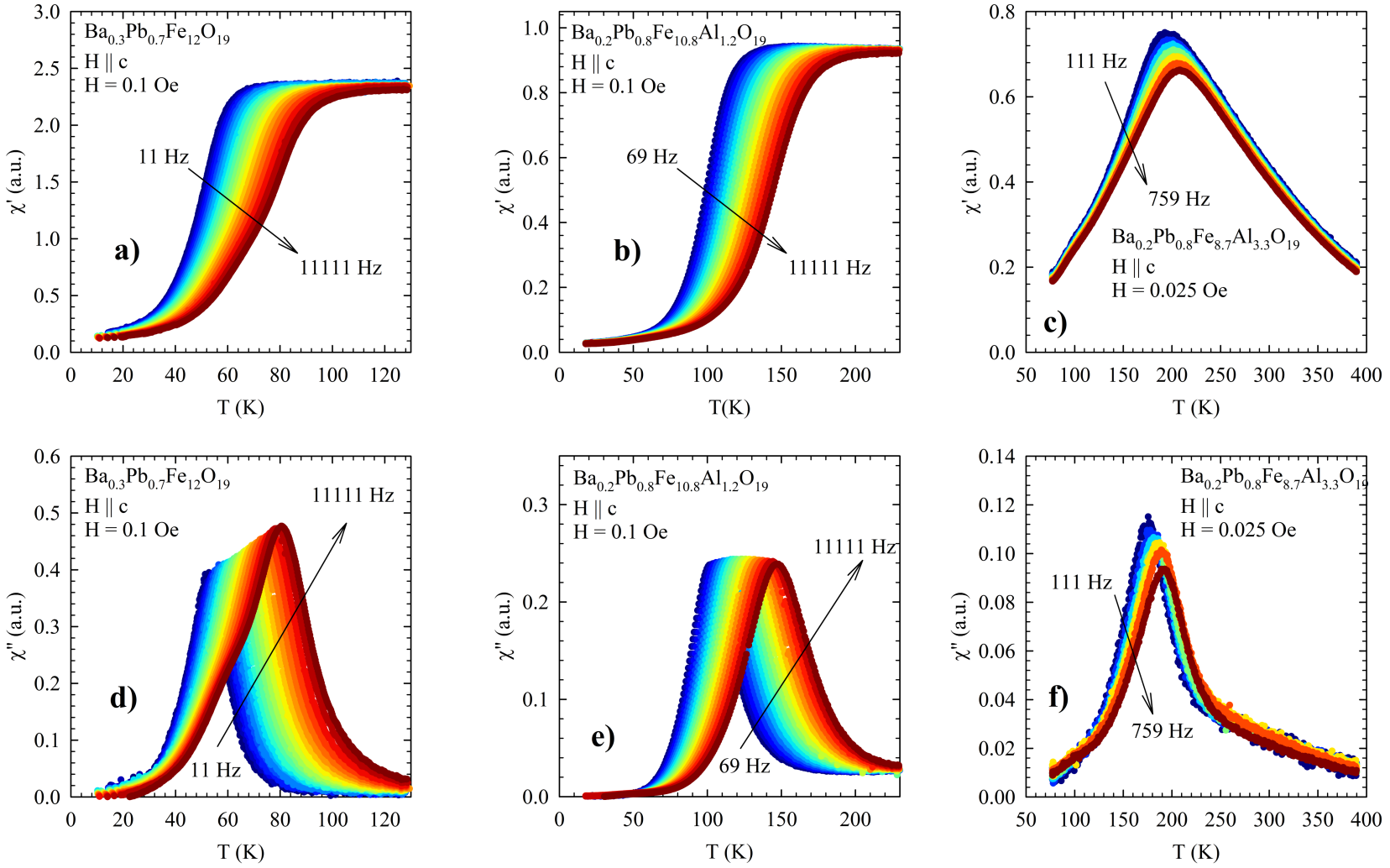


Figure 4.1: AC susceptibility measurements as a function of temperature and frequency for (Ba,Pb)(Fe,Al)$_{12}$O$_{19}$ M-type hexaferrites. Rows represent real (top) and imaginary (bottom) susceptibility, while columns represent samples Al0, Al1, and Al3 (left to right). Different colors represent different frequencies, with arrow pointing in the direction of increasing frequency with regards to color pallette.

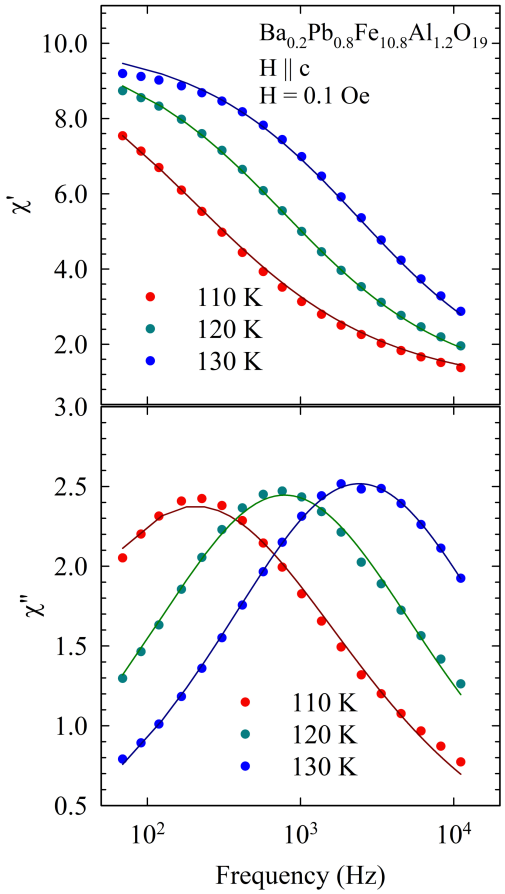


Figure 4.2: Frequency dependence of AC susceptibility for sample Al1 at 110 K, 120 K, and 130 K. Dots represent experimental data, while lines represent Cole-Cole model fits.

Parameters derived from the Cole-Cole model, including relaxation strength ($\Delta\chi$), mean relaxation time ($\tau$), and broadening parameter ($\alpha$), are shown in Figure 4.3. Key observations are:

- **Relaxation Strength ($\Delta\chi$):** Parameter is nearly constant for both samples. The values for different samples differ by almost order of magnitude.
- **Mean relaxation time ($\tau$):** Follows an exponential behaviour for both samples. This exponential behavior with Arrhenius-type temperature dependence: $\tau(T) = \tau_0 e^{E_a/kT}$, gives rise to activation energies of $E_a = 1100 \pm 100$ K for Al0 and $E_a = 1700 \pm 100$ K for Al1.
- **Broadening Parameter ($\alpha$):** Temperature-independent, with values of $1 - \alpha = 0.61 \pm 0.05$ for Al0 and Al1.

Sample Al3 exhibits a different relaxation process from Al0 and Al1, as shown in the last column in Figure 4.1, panels c) and f). A relaxation peak in $\chi''$ as a function

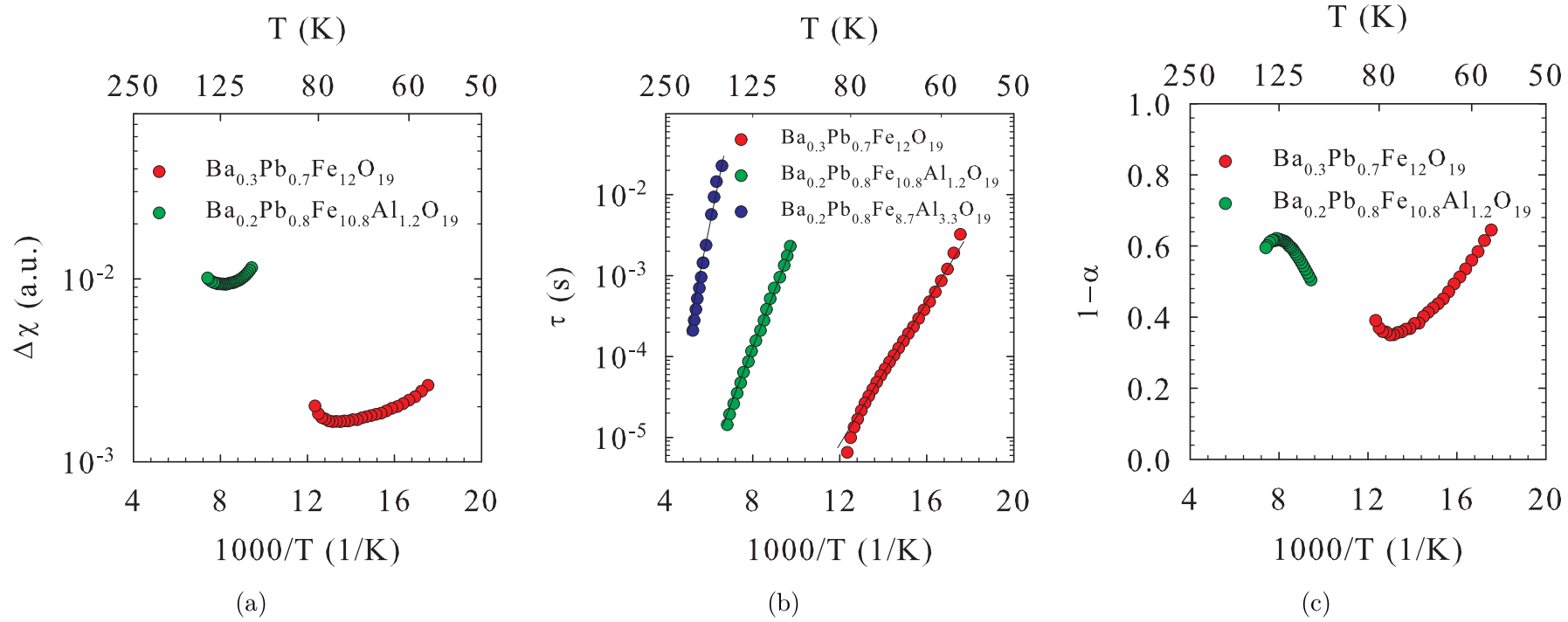


Figure 4.3: Temperature dependence of Cole–Cole model parameters: (a) $\Delta\chi$, (b) $\tau$, (c) $1-\alpha$. Inverse temperature (lower $x$-axis) and corresponding temperature (upper $x$-axis) are shown. In panel (b), lines indicate guides for the eye showing Arrhenius behavior. The absence of Al3 sample on panels (a) and (c) is explained in text.

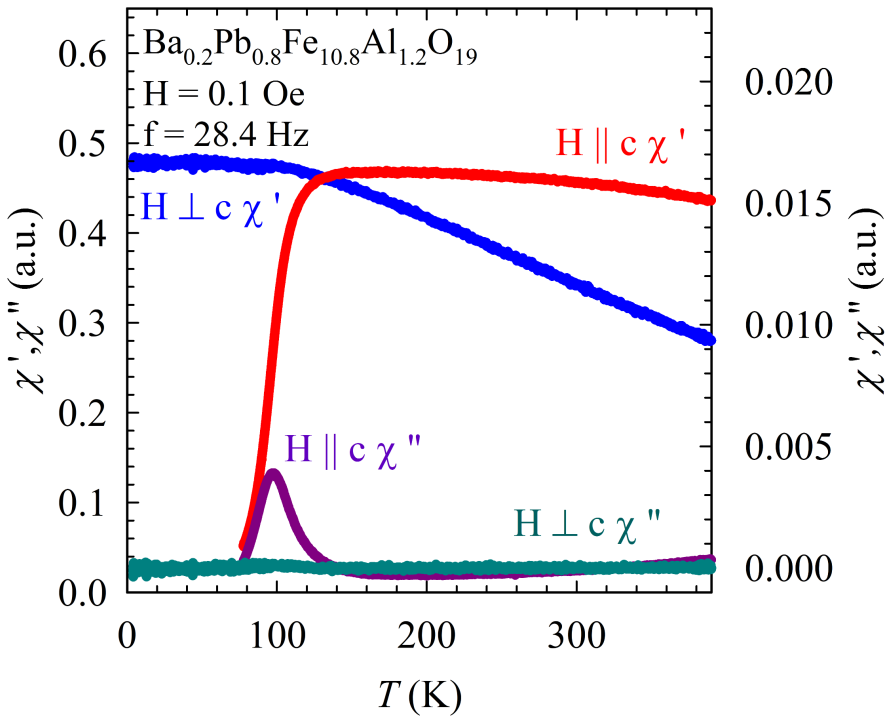


Figure 4.4: Anisotropy of AC susceptibility of Al1 sample measured with AC field of 0.1 Oe and frequency of 28.4 Hz. Red and purple curve are AC susceptibility measurements in $c$ direction, with red being real and purple being the imaginary part of AC susceptibility, while blue and green are real and imaginary part of AC susceptibility measured in direction perpendicular to $c$.

of $\omega$ is observed within a narrow temperature range[2], indicating a higher activation energy for $\tau_0$. Additionally, the peak-like behavior of $\chi'$ as a function of temperature is analogous to the response of superparamagnetic systems, which we described in subsection 3.1.3. Modeling of superparamagnetic data typically involves determining the mean relaxation time $\tau_0$, which corresponds to the maximum susceptibility in the temperature domain for each frequency due to the limited frequency dispersion. The mean relaxation time of Al3 follows an Arrhenius-type dependence as shown in Figure 4.3b, alongside samples Al0 and Al1 for comparison. Activation energy $E_a = 3700 \pm 100\,\mathrm{K}$ has been obtained for sample Al3 [27, 28].

### 4.1.1 Anisotropy of AC susceptibility

To further investigate the magnetic properties of the sample, we conducted measurements of the anisotropy of the AC susceptibility. The results are presented in

[2]This can also be expressed the following way: Peak traverses the experimental frequency window within a narrow temperature range.

Figure 4.4. These measurements were carried out within a plane perpendicular to the crystallographic $c$-axis, with an excitation frequency of 28.4 Hz and an applied AC field of 0.1 Oe.

For the susceptibility measured along the $c$-axis (red and purple points in Figure 4.4), the temperature dependence closely matches the behavior observed in previous measurements shown in Figure 4.1. However, the susceptibility measured in the plane perpendicular to the $c$-axis reveals distinct temperature dependent characteristics.

The real part of the susceptibility (blue points in Figure 4.4) increases with decreasing temperature, reaching a plateau at approximately 100 K, below which it remains constant. In contrast, the imaginary part of the susceptibility (green points in Figure 4.4) remains negligible across the entire measured temperature range.

This behavior is qualitatively very similar to Weiss model of uniaxial antiferromagnetism (equivalent model for ferrimagnetism is described in reference [19]) described in subsection 1.1.1. All of the phenomenological results can be described by the following sentence. Slowing down of domain wall dynamics behaves qualitatively like a phase transition to a ordered state with uniaxial symmetry.

## 4.2 Dielectric Spectroscopy

Dielectric spectroscopy measurements were conducted on the Al0, Al1, and Al3 samples using a Keysight 4980AL instrument with an excitation voltage of 50 mV. Measurements were taken over a temperature range of 4.2 K to 300 K and frequencies between 100 Hz and 1 MHz. The real part of the dielectric function is shown in Figure 4.5. The panels represent the samples Al0, Al1, and Al3 (left to right), where different colors are different frequencies. Temperature range that is shown is the one that is relevant for the dispersion.

Temperature-dependent dispersion in the dielectric function was observed:

- **Al0:** The dielectric response exhibits a gradual change with temperature, showing a broad dispersion over the measured range. No pronounced peaks in $\varepsilon'$ are evident. The dispersion separates the low temperature, low value dielectric function from high temperature high value dielectric function[3].

- **Al1:** Similar trends to Al0 are observed, but with the dispersive features shifted toward higher temperatures. The frequency dependence remains consistent to the Al0, across the measurement range.

- **Al3:** Similar trend with features pushed into even more higher temperatures.

[3]With regards to the frequency window that was used, we can imagine that having arbitrarily large frequency window could have dispersion that persists to the lowest temperatures measured.

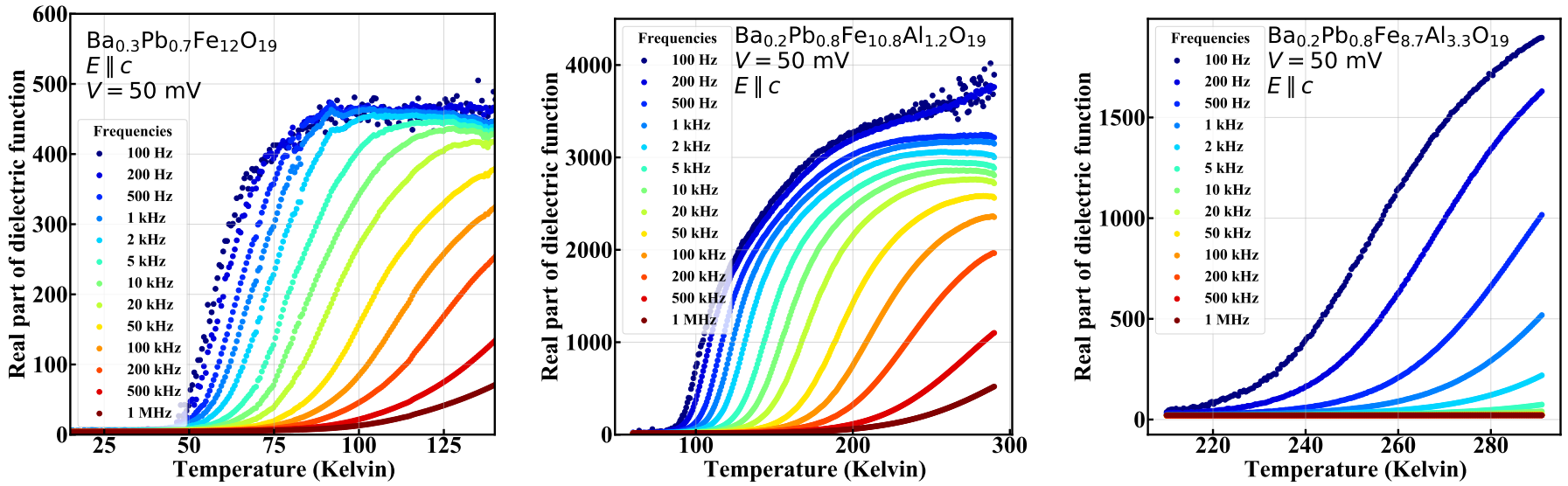


(a) (b) (c)

Figure 4.5: Real part of the dielectric function ($\varepsilon'$) as a function of temperature and frequency for three $Ba_xPb_{1-x}Fe_{12-y}Al_yO_{19}$ samples. Plots represent measurement for different samples: (a) Al0 ($Ba_{0.3}Pb_{0.7}Fe_{12}O_{19}$), (b) Al1 ($Ba_{0.2}Pb_{0.8}Fe_{10.8}Al_{1.2}O_{19}$), and (c) Al3 ($Ba_{0.2}Pb_{0.8}Fe_{8.7}Al_{3.3}O_{19}$). Measurements were conducted over a frequency range from 100 Hz to 1 MHz, and the temperature range for each sample is displayed only where the dispersion exists.

To quantify these results frequency dependent spectra at fixed temperatures are taken, and the data are fitted with Cole-Cole model (analogous procedure as in previous Section 4.1, Figure 4.2, additionally employing data analysis techniques described in subsection 3.3.3):

$$\varepsilon^*(\omega) = \varepsilon_\infty + \frac{\Delta\varepsilon}{1 + (i\omega\tau)^{1-\alpha}}, \tag{4.2}$$

where $\Delta\varepsilon = \varepsilon_0 - \varepsilon_\infty$ represents the relaxation strength, $\tau$ is again the mean relaxation time, and $\alpha$ is the broadening parameter. Fitting the Cole Cole model on the whole temperature interval of the dispersion we obtain a temperature dependence of parameters shown on Figure 4.6.

The behavior of parameters is as follows:

- **Relaxation Strength ($\Delta\varepsilon$):** In all samples, the property remains approximately independent of temperature. The magnitude of $\Delta\varepsilon$ differs slightly between the samples.

- **Mean relaxation time ($\tau$):** Exhibits Arrhenius-type temperature dependence, $\tau(T) = \tau_0 e^{E_a/T}$. Activation energies of $E_a = 700 \pm 100$ K, $E_a = 1300 \pm 100$ K, and $E_a = 3000 \pm 100$ K were determined for samples Al0, Al1, and Al3, respectively.

- **Broadening Parameter ($\alpha$):** Close to 1 for all samples, indicating a single dominant relaxation process without significant distribution of relaxation times.

The dielectric dispersion reported here should be evaluated in the context of the possible extrinsic effects discussed in Section 1.5. The initial argument is that all three samples exhibit qualitatively similar dispersion. In addition, repeated measurements on Al0 and Al3 samples performed with different contact geometries ($\perp c$) and different contact resistances yielded quantitatively similar relaxation behavior. Further support for an intrinsic contribution is provided by independent dielectric spectroscopy measurements on $Ba_{1-x}Pb_xFe_{12}O_{19}$ reported in reference [54]. Taken together, these results indicate that the relaxation is robust across samples and measurement configurations.

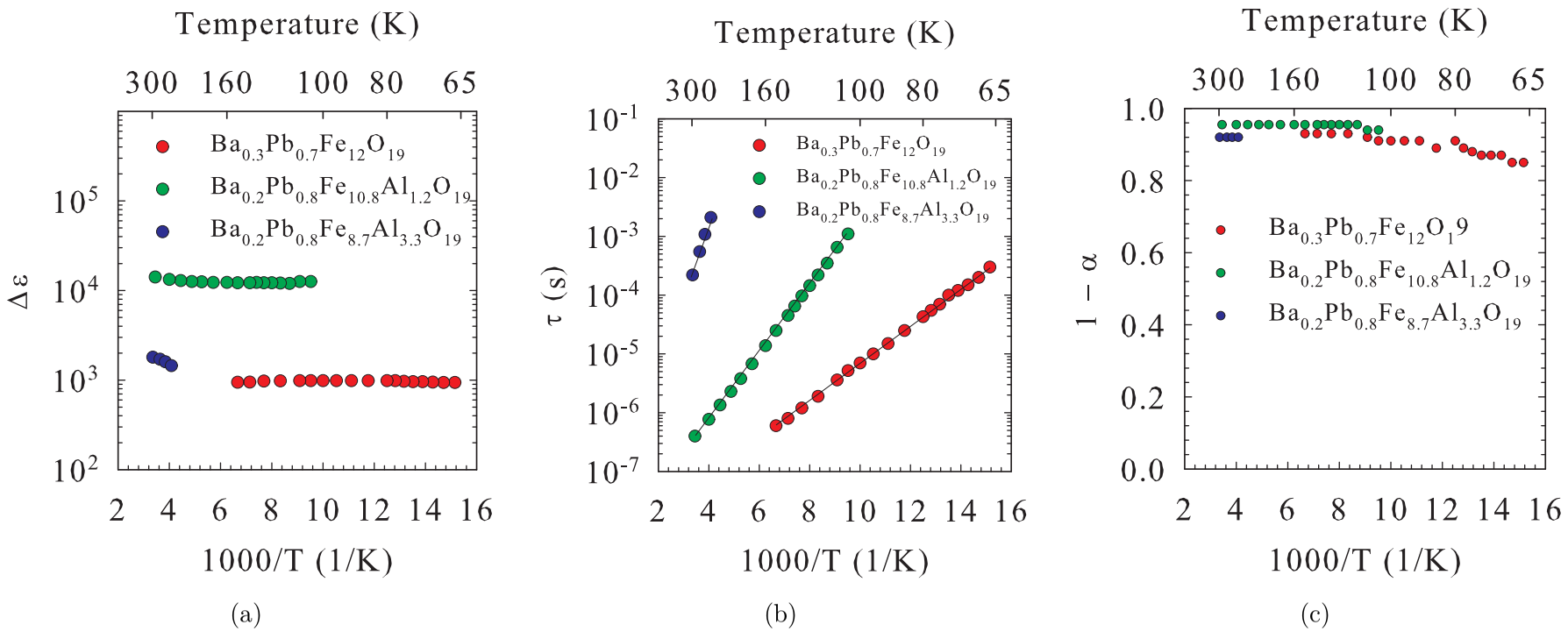


Figure 4.6: Cole–Cole model parameters for dielectric spectroscopy: (a) Relaxation strength $\Delta\varepsilon$, (b) Mean relaxation time $\tau$, and (c) Broadening $1 - \alpha$. Black lines in panel (b) represent guides for the eye of Arrhenius behavior.

## 4.3 DC Transport

DC resistivity was measured using both four-point and two-point setups. In the four-point setup, the current source Keithley K6221 [61] was used in combination with a nanovoltmeter Keithley 2182A [95]. The two-point setup employed the Keithley 487 picoammeter/voltage source [96]. Measurements were performed over a temperature range from 4.2 K to 300 K. Results are shown in Figure 4.7.

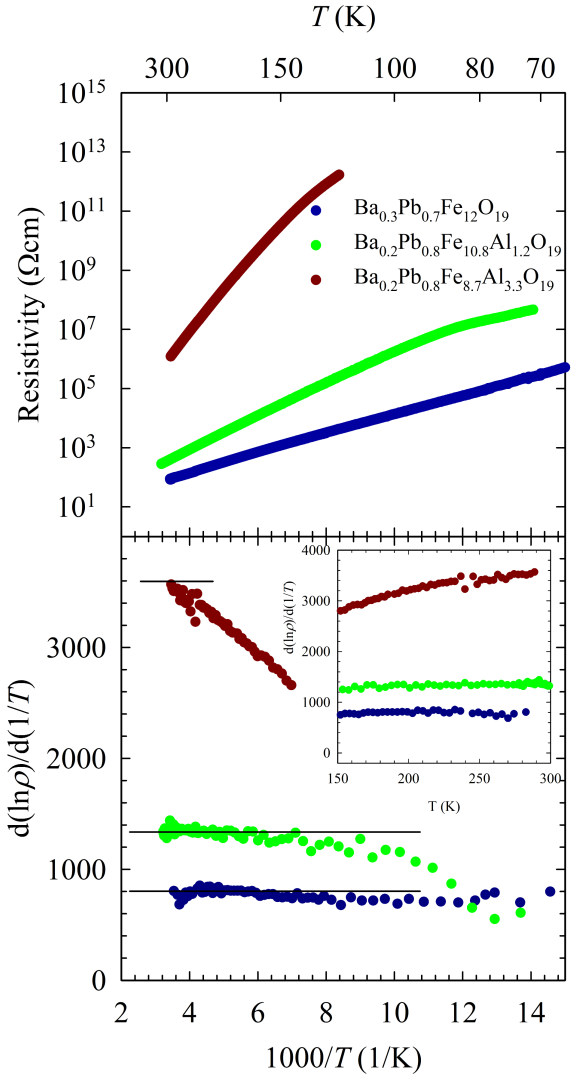


Figure 4.7: Temperature dependence of resistivity for samples Al0, Al1, and Al3. The $x$-axis shows the inverse temperature ($1000/T$), with the upper axis displaying the corresponding temperature scale. The bottom panel shows the logarithmic derivative of resistivity. The inset compares the temperature dependence of the logarithmic derivative of resistivity with the linear temperature scale. Black lines indicate the activated behavior ($\frac{E_g}{2k_B}$) as guides for the eye.

The resistivity increases with decreasing temperature for all samples, showing an

exponential dependence indicative of semiconductor behavior. This is evident from the logarithmic derivative,

$$\frac{d(\ln \rho)}{d(1/T)} = \frac{E_g}{2k_B}, \tag{4.3}$$

where $E_g/2k_B$ represents half of the energy gap, expressed in temperature units (Kelvin). For this thesis, $E_g/2k_B$ is referred to as the activation energy for ease of comparison. The logarithmic derivative is shown in the bottom panel of Figure 4.7.

Samples Al0 and Al1 closely follow semiconductor behavior, as indicated by a flat logarithmic derivative across almost the entire temperature range. The activation energies for these samples are $800 \pm 100$ and $1400 \pm 100$ K, respectively. Sample Al3, however, exhibits high resistivity even at 300 K ($\approx 1\,\mathrm{M\Omega\,cm}$) and shows temperature-dependent logarithmic derivatives. This behavior could arise from extrinsic effects such as contact resistance in the 2-point measurements. The transition from 4-point to 2-point measurements occurs at approximately 250K, $\approx 10\,\mathrm{M\Omega}$. At high temperatures, the logarithmic derivative flattens (as seen in the inset of Figure 4.7), which is more reliable due to 4-point measurements. Additionally, the flattening appears more pronounced when plotted on a linear temperature scale because the inverse temperature scale is disproportionately sensitive to lower temperatures. In other words, the data point distribution causes low-temperature measurements to be overemphasized in $1/T$ plots. Extrapolating the high-temperature data for Al3 yields an activation energy of $3600 \pm 100$ K.

## 4.4 X-ray absorption spectroscopy

To investigate the influence of the local structure on the spectral characteristics of absorber atoms, the experimental technique of X-ray absorption spectroscopy (XAS later in text) was used. Energy range of L-edge Iron ($\approx 690 - 730$ eV) was chosen for this specific investigation by its relevance to the phenomena being studied. Measurements of absorption were done with polarization in horizontal and vertical direction the x-ray beam oriented approximately in crystallographic c-direction of the Al0 hexaferrite, $Ba_{0.3}Pb_{0.7}Fe_{12}O_{19}$ at 300K. The difference of horizontal and vertical polarization is expected for crystalline material, so these measurements are additionally useful to check whether the material is crystalline in the probing volume of the applied x-rays. To understand the measurements simulations are performed. The measurements were simulated by ligand field theory (see section 1.6) using a program Crispy [89] which we discussed in experimental subsection 3.4.3. Initial

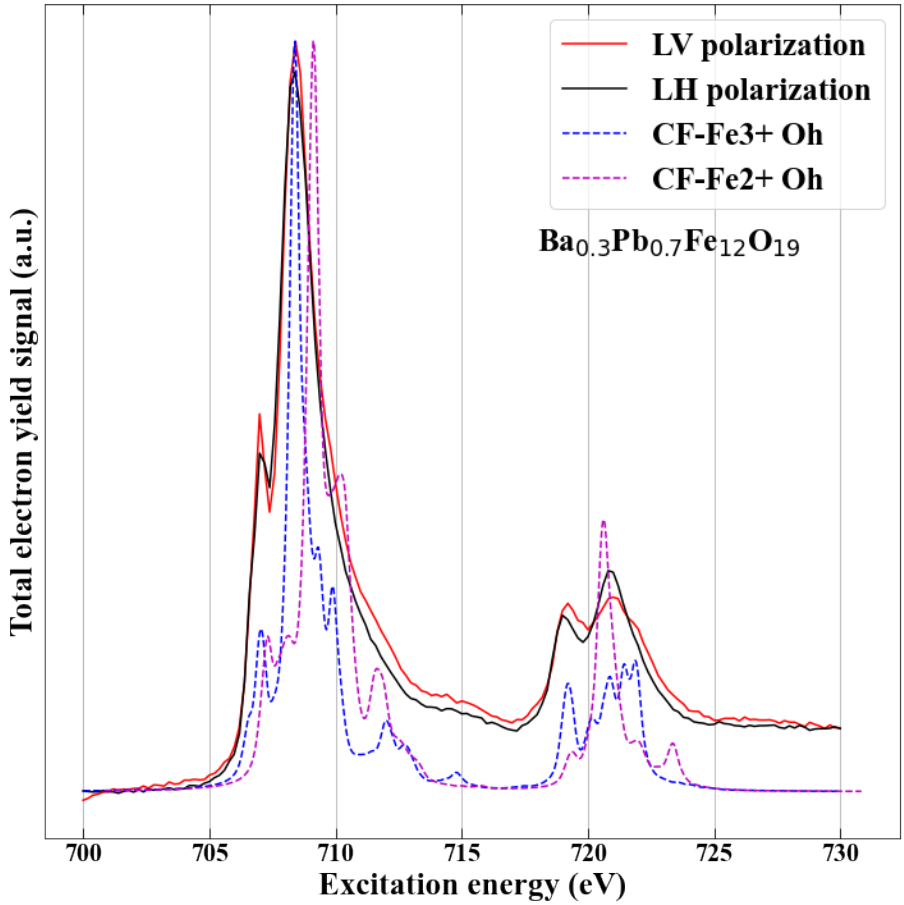


Figure 4.8: Measurements of x-ray absorption spectroscopy on iron L3,2 edge on sample $Ba_{0.3}Pb_{0.7}Fe_{12}O_{19}$. Red solid line is the measurement with vertical polarization of light, while black solid line is the measurement with horizontal polarization. Wave vector of light is oriented in the $c$ direction. The anisotropy of absorption is due to crystal anisotropy in ab plane of the crystal. Blue dashed line is the simulation of absorption using crystal field theory of $Fe^{3+}$ sites in octahedral geometry, while magenta dashed line is the simulation of the same geometry with $Fe^{2+}$ valency.

parameters[4] for the simulated spectra were taken from the literature [93, 94]. Results of the measurements and simulations are shown on Figures 4.8 and 4.9.

Figure 4.8 presents the experimental data and crystal field simulations of the horizontal and vertical polarization x-ray absorption in a Al0 sample. The measurements of horizontal and vertical polarization are shown as black and red full lines, respectively. Measurements display the difference between the polarizations i.e. linear dichroism. This phenomenon is indicative of the sample's crystalline na-

[4]The following parameters were used for the calculations. $10Dq_{(\text{octahedral})} = 1.1\,\text{eV}$, $10Dq_{(\text{tetrahedral})} = -0.5\,\text{eV}$, with Slater parameters reduced to 72% of the HF values. For the trigonal bipyramidal sites the $C_{3v}$ symmetry was used with $10Dq = 0.8\,\text{eV}$, $D_\tau = -0.08\,\text{eV}$ and $D_\sigma = 0.01\,\text{eV}$.

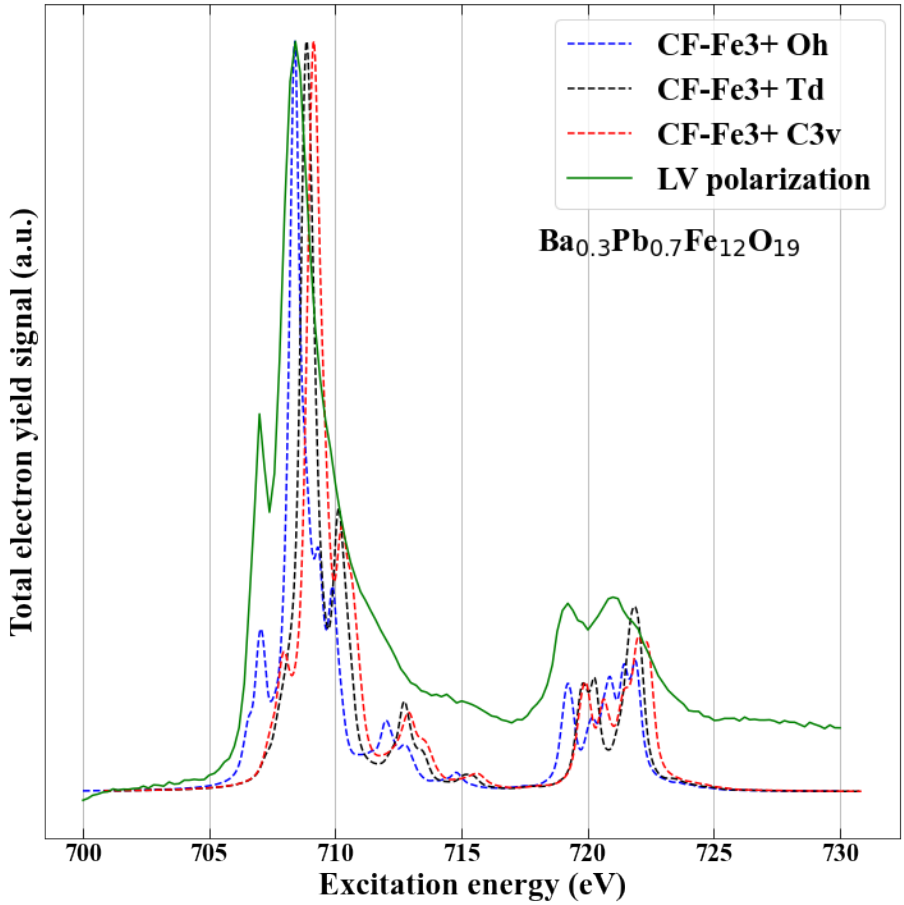


Figure 4.9: Measurements and simulations of x-ray absorption spectroscopy on iron L3,2 edge on sample $Ba_{0.3}Pb_{0.7}Fe_{12}O_{19}$. Green solid line is the measurement with vertical polarization of light. Wave vector of light is oriented in the $c$ direction. Blue dashed line is the simulation of $Fe^{3+}$ sites in octahedral geometry, black dashed line is the simulation of $Fe^{3+}$ sites in tetrahedral geometry and red dashed is the simulation of $Fe^{3+}$ sites in bi-pyramidal geometry.

ture, as it suggests ordered state of probed orbitals. Crystal field simulations are represented by blue and magenta dashed lines. The blue dashed line is a simulation for the $Fe^{3+}$ octahedral site, while magenta dashed line represents simulations the same octahedral site with the same splitting in $Fe^{2+}$ state.

The simulations show dominant contribution of $Fe^{3+}$ octahedral sites in the experimental data. This aligns with expectations, because the octahedral site is the most numerous site in crystal structure, and thus it is expected for it to have major contribution in experimental absorption spectral characteristics. In Figure 4.9, 4 curves are shown. The green full line is the experimental vertical polarization absorption data, while blue, magenta and red dashed lines are simulations of different crystallographic sites expected for M-type hexaferrite. Again the octahedral $Fe^{3+}$ site describes the most of the spectral feature, in this case due to prepeak at $\approx 707$

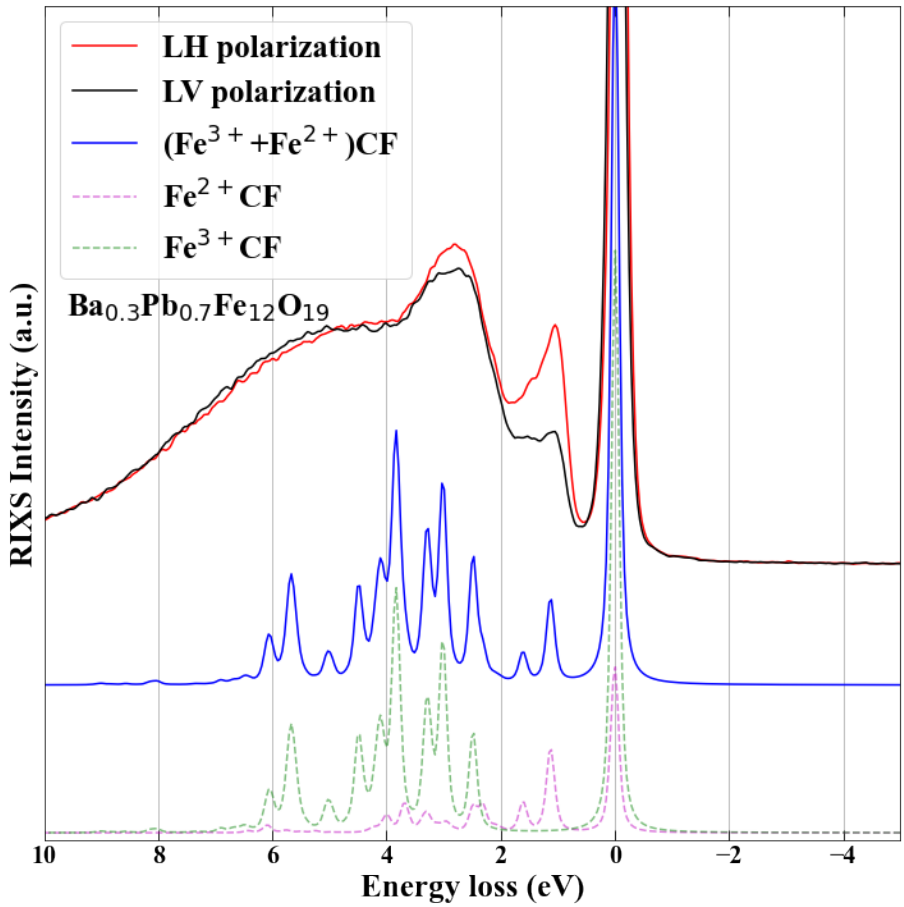


Figure 4.10: Measurements of resonant inelastic x-ray scattering on sample $Ba_{0.3}Pb_{0.7}Fe_{12}O_{19}$. Wave vector of light is oriented in the c direction. Black line indicates measurement with right hand circular polarization, green and magenta dashed lines represent crystal field simulations for iron in $Fe^{3+}$ and $Fe^{2+}$ oxidation states respectively. Blue line is superposition of the two simulations.

eV. The contribution of other sites cannot be determined because the resolution of the experiment is lower than the resolution of the simulation. In principle we could fit the data using principal component analysis [97], and this was done, but undetermined parameters such as the shape/choice of the background that needs to be subtracted from the experimental data and the amount of Gaussian broadening for every simulation significantly influenced the fit results, thereby making the technique ineffective and potentially deceiving.

## 4.5 Resonant inelastic x-ray spectroscopy - RIXS

Resonant inelastic X-ray spectroscopy (RIXS) measurements were conducted on the Al0 sample with x-ray photon energy corresponding to the L3 edge maximum 708 eV. The measurements were performed at 300K. The first set of measurements

were performed using linear horizontal and vertical polarization. The orientation of the X-ray beam was aligned approximately along the $c$ crystallographic axis of the sample. The measurements are shown on Figure 4.10 as red and black lines. Additionally these measurements are supported by crystal field simulations with the same parameters used in X-ray absorption spectroscopy (XAS). The simulations are as follows: green dashed line is the simulation of $Fe^{3+}$ in octahedral symmetry, magenta dashed line is the simulation $Fe^{2+}$ in octahedral symmetry and and blue line is superposition of the two aliovalent simulations.

Measurements in Figure 4.10 reveal dichroism, especially pronounced in the 1 eV range. This dichroism is attributed to the orbital ordering in the crystalline structure, which leads to a polarization dependent absorption phenomena. The spectral features are separated into two distinct regions: a narrow peak observed at 1 eV, and a broader spectral distribution beginning at 2 eV. Amplitude of the narrow peak at 1 eV is suppressed under by photons with horizontal polarization.

Simulations of RIXS spectra, which we discussed in subsection 3.4.3, were performed using Crispy [89]. Parameters for the RIXS simulations are kept the same as for XAS in Section 4.4. Analysis of the simulations confirm the contrast between spectral features. Distribution occurring at 2 eV and above can be attributed to $Fe^{3+}$ ions situated primarily within the octahedral crystal field. The crystal field simulations were unable to simulate low-energy 1 eV peak with the $Fe^{3+}$ ions in any coordination environment. The simulation of $Fe^{2+}$ ions in an octahedral setting successfully simulated the observed peak at 1 eV.

In this chapter an experimental dataset was presented. The experimental data of AC susceptibility, dielectric spectroscopy, dc resistivity, X-ray absorption (XAS) and resonant inelastic X-ray scattering (RIXS) was obtained on M-type hexaferrite samples in which the Al content was systematically varied. In the next chapter we will attempt to combine these complementary results, using shared activation energy scales, local structure insights and relaxation models to build a description of how Al substitution affects the magnetic and electric properties.

# Chapter 5

# Discussion

This chapter synthesizes the results of our investigation into the magnetic, dielectric, and electronic transport properties of (Pb,Al)-substituted M-type hexaferrites. The focus is to understand the interplay between these properties and the mechanisms underlying them.

Relaxation phenomena in magnetic and dielectric subsystems, revealed through AC susceptibility and dielectric spectroscopy, show how aluminum substitution modulates dynamics. Complementary dc transport measurements highlight the coupling between magnetic and dielectric processes. Activation energies for resistivity and dielectric relaxation correlate strongly, suggesting a shared mechanism. Advanced spectroscopic techniques, including XAS and RIXS, provide insights into local structures and electronic states, emphasizing the role of $Fe^{2+}$ ions and structural distortions.

The chapter proposes charged magnetic domain walls as a unifying framework for these observations. Broader implications include parallels with other systems, such as organic charge transfer salts and antiferromagnetic materials, where similar behaviors are linked to domain wall dynamics. Alternative hypotheses, including Jahn-Teller centers and $Fe^{2+}$ ion diffusion, are also considered.

This discussion integrates experimental observations with theoretical models to elucidate the complex behavior of Al-substituted M-type hexaferrites, highlighting how structural and electronic modifications shape their properties.

## 5.1 Magnetic and dielectric relaxation

Magnetic relaxation of samples Al0 and Al1, Figures 4.1 and 4.3, exhibit characteristics consistent with overdamped magnetic domain wall dynamics, discussed in 3.1.3. These dynamics are inferred from the temperature-dependent relaxation parameters and the magnetic properties discussed in section 3.1.3, particularly the mean relaxation time $\tau$, which follows an Arrhenius behavior $\tau = \tau_0 e^{E_a/kT}$, Figure 4.3b. The activation energies for Al0 and Al1 are $1100 \pm 100$ K and $1700 \pm 100$ K. The relaxation strength of AC susceptibility, $\Delta\chi$, is approximately temperature independent, Figure 4.3a, in the measured temperature range for both samples. Equation $\chi_w = \frac{4M_s^2}{\alpha D}$, which we discussed in section 3.1.3, connects the relaxation strength to properties such as saturation magnetization, anisotropy and domain wall width and separation. This means that in the measured temperature interval those parameters are approximately independent of temperature. The broadening parameter ($\alpha$) has a slight temperature dependence (see Figure 4.3c) meaning that the distribution of mean relaxation times slightly changes. We document this observation here, though its detailed interpretation remains beyond the scope of this thesis.

In contrast, sample Al3 shows features indicative of superparamagnetic relaxation. The change of susceptibility dispersion and distinct curve shapes in the susceptibility suggest a transition from domain wall dynamics to a superparamagnetic-like state. This transition is attributed to increased disorder introduced by aluminum substitution, which likely reduces domain size or particle size to a scale where thermal energy is comparable to the anisotropy barrier (Figure 3.4), leading to superparamagnetic behavior. The activation energy of Al3 sample of $3700 \pm 100$ K has been obtained.

From our analysis of these three samples, we find that increasing the aluminum content in the structure raises the activation energy of the relaxation process (even though obtained by different phenomenologies). In other words, as the aluminum concentration grows, the slowing down phenomena appear at higher temperatures, at which the system becomes effectively unresponsive to external driving field, showing a substantial reduction in magnetic susceptibility.

The dielectric relaxation of samples Al0, Al1, and Al3, shown in Figure 4.5, exhibits characteristics consistent with overdamped motion, as described in Section 3.3.4. This behavior is similar to the AC susceptibility measurements of Al0 and Al1 discussed in Section 5.1. The dielectric relaxation is characterized by temperature-dependent relaxation parameters, particularly the mean relaxation time $\tau$, which follows Arrhenius behavior: $\tau = \tau_0 e^{E_a/kT}$ (Figure 4.6b). The activation energies for Al0, Al1, and Al3 are $700 \pm 100$ K, $1300 \pm 100$ K, and $3000 \pm 100$ K, respectively.

The relaxation strength ($\Delta\varepsilon$) remains nearly constant across the measured temperature range for all samples (Figure 4.6a), with a relatively large value of approximately $10^3$ to $10^4$, compared to the other materials ( $10^1$ to $10^2$) see Reference

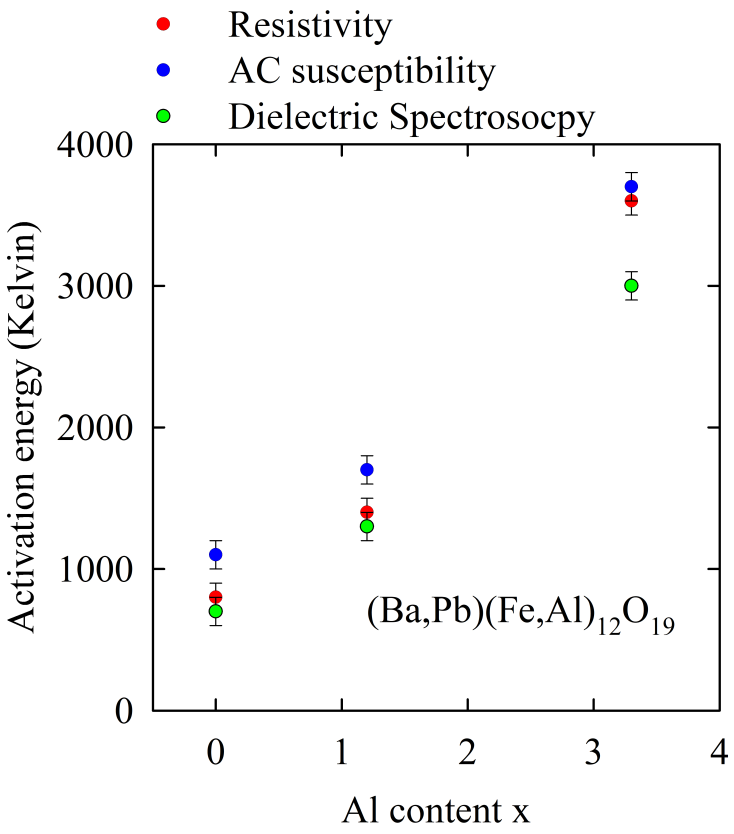


Figure 5.1: Activation energies of magnetic and dielectric subsystems as a function of Aluminium content.

[66](TABLE 5 Dielectric constants of crystals), although there exist states with larger values [98]). Additionally, the broadening of the mean relaxation times is close to 1 (Figure 4.6c) and remains constant over the measured temperature interval for all three samples.

In these three samples, we observe that the increasing aluminum content affects the relaxation dynamics in a manner similar to its influence on AC susceptibility, having the activation energy increase with aluminum content. Even more striking is the observation that the activation energies of dielectric and magnetic relaxation are of comparable magnitude. This similarity suggests a potential common underlying mechanism. To further explore this hypothesis, we will first analyze dc transport before delving deeper into the discussion.

As discussed in results section 4.3, all samples have resistivity behavior similar to that of semiconductors (considering temperature dependence). Fitting the data to semiconducting behavior $\rho = \rho_0 e^{E_a/kT}$ we obtain transport activation energy $E_a$ with values $800 \pm 100$ K, $1400 \pm 100$ K and $3600 \pm 100$ K for samples Al0, Al1 and Al3 respectively.

It seems that dc transport measurements provide further evidence for the cou-

pling between magnetic and dielectric relaxation. The similarity in activation energies for resistivity and dielectric relaxation supports the hypothesis that both processes are governed by the same fundamental mechanism. All of the activation energies are shown on Figure 5.1, with respect to aluminum content. The figure reveals a significant correlation between the activation energies governing magnetic relaxation and electrical transport across three different Al substitutions.

## 5.2 Interpretation of Charged Domain Walls

The hypothesis of charged magnetic domain walls is proposed to unify the observed phenomena. This hypothesis was first mentioned in paper on sample Al0 [7], where a similarity in relaxation energies was observed. This thesis builds upon on that idea, and probes it's validity from more experimental directions. The hypothesis presupposes domain walls which carry charges due to dielectric anomalies within the crystal structure, potentially linked to distortions in the bi-pyramidal sites. Spin inhomogeneities in the domain walls (Figure 1.5) are generally reminiscent of spontaneous spin distributions that lead to dipole moment in multiferroics [4, 33]. This means that domain walls could posses dipole moments that give rise to charged magnetic domain walls. This interpretation is supported by independent imaging work on M-type barium hexaferrite, where combined magnetic and electrostatic force microscopy revealed electrical polarity localized at magnetic domain boundaries, providing direct experimental support for electrically active domain walls in this material family [54].

Pinning centers, attributed to aliovalent defects such as $Fe^{2+}$ ions, interact with these charged domain walls. The introduction of activated charge carriers screens these interactions, reducing pinning and facilitating domain wall motion.

Illustration of the hypothesis on the Figure 5.2.

### 5.2.1 Role of $Fe^{2+}$ and Local Structure

XAS measurements and simulations, Figures 4.8 and 4.9, do not show any evidence of $Fe^{2+}$ ions, while the local structure that contributes to the measured signal comes primarily from octahedral sites, which was found in similar hexaferites in literature [93]. However, RIXS measurements and simulation, shown on Figure 4.10, reveal the presence of $Fe^{2+}$ ions, which could be linked to oxygen vacancies or electron lone pairs in $Pb^{2+}$ ions [7]. Still, RIXS is not able to resolve between local environments, but the low-energy excitation at 1 eV has been linked to $Fe^{2+}$ ions.

The key difference between XAS and RIXS lies in their spectral resolving power. In XAS, it is challenging to credibly disentangle the contribution of the $Fe^{2+}$ spectrum from other overlapping components, as seen in Figure 4.8. Conversely, RIXS

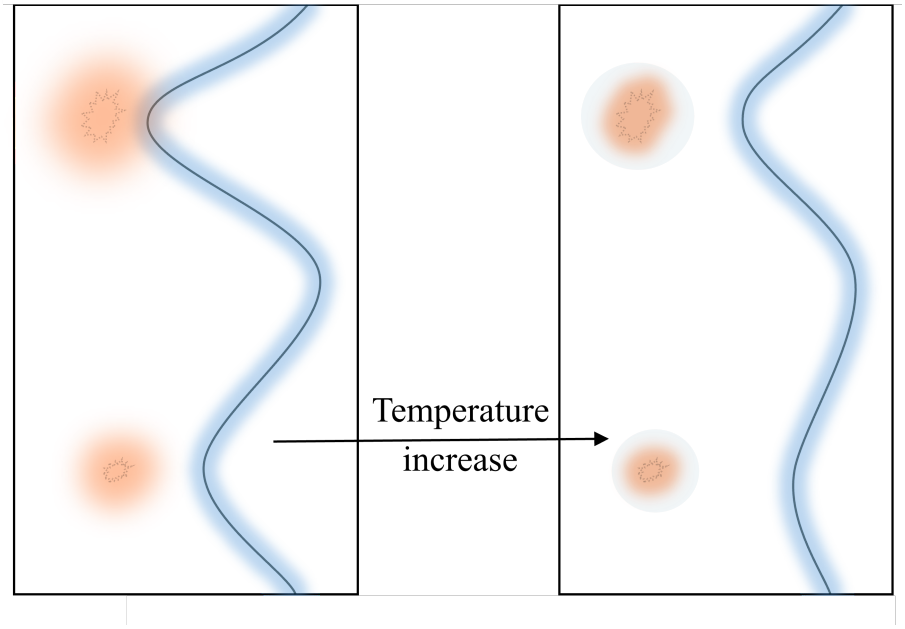


Figure 5.2: Illustration of charged magnetic domain walls. Black curves represent the domain walls, each with a soft blue glow representing their electrical charge. Charged defects appear as closed discontinuous loops enveloped in a reddish halo that represents their charge. The walls are attracted toward these charged defects. The two panels correspond to different temperatures. Additionally, in the right-hand panel a faint blue halo around the defect illustrates charge screening by activated charge carriers at higher temperatures.

provides a distinct advantage: the low-energy 1 eV peak serves as a marker of $Fe^{2+}$, which is not achievable under reasonable assumptions for $Fe^{3+}$ coordination environments. This low energy peak corroborates the idea that charge defects are present in a material, thereby providing additional evidence and insight for the hypothesis.

A Pb-specific route toward $Fe^{2+}$ formation is further supported by terahertz spectroscopy on $Ba_{1-x}Pb_xFe_{12}O_{19}$, where narrow THz absorption lines were attributed to electronic transitions within the fine-structure components of tetrahedrally coordinated $Fe^{2+}$ [54]. In that work, $Fe^{2+}$ occurrence in BaM and Pb-substituted BaM is discussed in terms of growth-related oxygen vacancies and an additional electronic contribution from $Pb^{2+}$ (sharing of the outer $6s^2$ electron pair with $Fe^{3+}$) [54]. This provides an explicit microscopic pathway by which Pb substitution can influence the density of aliovalent defects that are central to pinning/screening scenarios for electrically active domain walls.

### 5.2.2 Domain Wall Dynamics and Superparamagnetism-like behaviour

Although Al0 and Al1 exhibit domain wall dynamics and Al3 shows superparamagnetic behavior, both processes share a common feature: the association of a timescale with a relaxation process. In domain wall dynamics, this timescale is the mean relaxation time $\tau$, while in superparamagnetic relaxation, it corresponds to the inverse of the switching frequency (discussed in subsection 3.1.3).

The energy barrier for spin reversal in these systems, estimated as $E_a = KV$, depends on the magnetocrystalline anisotropy energy ($K$) and a characteristic volume ($V$). In domain wall dynamics, $V$ represents the switching volume related to domain walls, whereas in superparamagnetic relaxation, it corresponds to the single-domain particle volume[1] [99].

### 5.2.3 Comparison with other systems exhibiting slow relaxations

Because well-characterized materials that exhibit slow-relaxation phenomena in more than one subsystem are rare outside glassy or otherwise disordered contexts, finding truly comparable references is challenging. Nevertheless, in this thesis we compare our hexaferrite data and working hypothesis with a few crystalline[2] compounds that display similar phenomenology and relaxation dynamics in either their magnetic or their dielectric subsystems.

The observed relaxation behavior in $(Ba,Pb)(Fe,Al)_{12}O_{19}$ has similarities with previous research of organic charge transfer salt $\kappa$-(BEDT-TTF)$_2$Cu[N(CN)$_2$]Cl, which exhibit long-range canted antiferromagnetic order. In this organic system, a similar relaxation process was identified within the dielectric subsystem, characterized by an activation energy of mean relaxation times comparable to the semiconductor transport gap [100, 101]. The broad dielectric relaxation in $\kappa$-(BEDT-TTF)$_2$Cu[N(CN)$_2$]Cl was attributed to the motion of charged domain walls separating magnetic domains. These domain walls are pinned by impurities, which are screened by free charge carriers. As temperature decreases, the concentration of free charge carriers diminishes, reducing the screening efficiency and consequently slowing the relaxation dynamics of the pinned domain walls [100–102].

Furthermore, analogous phenomena have been reported in the organic spin-liquid

[1] From the point of view of domain energetics (Equation 1.9, Section 1.1.2), we are only concerned with the anisotropy term $F_{\text{an}}(\mathbf{m})dV$ and the external field term $-\mathbf{H}_{\text{ex}} \cdot \mathbf{M}dV$, as their switching phenomenology does not change with domains or clusters.

[2] Crystalline is emphasized because one could devise a disordered composite that reproduces similar AC susceptibility or dielectric-spectroscopy signatures. These systems would not be able to interact as the crystalline would so we omit them in a discussion.

compound $\kappa$-(BEDT-TTF)$_2$Cu$_2$(CN)$_3$ [103], where a relaxor-ferroelectric-like dielectric response was attributed to charge defects localized at interfaces between frustration-induced magnetic domains. The formation of these domains is driven by the loss of local inversion symmetry.

Lastly, we remind that the AC susceptibility of our uniaxial ferrimagnet hexaferrite (see experimental data in 4.4) behaves qualitatively as dc susceptibility of an antiferromagnet (Figure 1.4). Building on these similarities, our results reveal that the hexaferrites exhibit an anisotropic response resembling the response observed in antiferromagnetic materials.

### 5.2.4 Evaluation of Current and Alternative Hypotheses

Current hypothesis is supported by independent research on broadband electrodynamic work on Pb-substituted BaM single crystals, where intrinsic radio-frequency dielectric relaxations were linked to the dynamics of electrically polar magnetic domain walls [54]. In this broader context, Pb substitution can be viewed as an enabling parameter (via polar lattice tendencies and defect chemistry conducive to $Fe^{2+}$-type charge centers), while Al substitution predominantly tunes magnetic disorder and thereby shifts the relaxation and transport activation energies of the charged magnetic domain walls. This interpretation is partly supported by the scanning-probe results reported in the same study, where $BaFe_{12}O_{19}$ showed a clear electrostatic polarization at magnetic domain boundaries. However, no comparable electrostatic response was detected in the Pb-doped crystal, which indicates that the domain-wall polarity is either suppressed, modified, or below the detection limit of the technique in that composition [54].

In that regard, we anticipated magnetoelectric features to manifest in our experimental observations. Specifically, we searched for magnetoelectric features by measuring AC susceptibility under the application of an electric field (10 kV/cm), but no evidence of a magnetoelectric effect was observed. Additionally, dielectric spectroscopy measurements conducted under a magnetic field of 5 T revealed no measurable changes. However, it is important to note that these measurements do not directly probe the magnetoelectric effect ($P \propto H$ or $M \propto E$) but rather examine the magnetoelectric coupling via "cross-susceptibility" effects ($\chi \propto E$ or $\varepsilon \propto H$). The absence of measurable coupling may be attributed to insufficient field strengths or a small intrinsic effect. Based on literature, the degree of domain alignment at 5 T should suffice to fully magnetically polarize hexaferrites [7], which suggests that the concept of charged magnetic domain walls may not apply under these conditions.

One alternative hypothesis is that the observed effects might be coincidental. To test this, additional samples with varying (Ba,Pb) and (Fe,Al) compositions would be required to map out a phase diagram of the behavior, but such samples were unavailable in this study. Another possibility is the involvement of a third

variable influencing both magnetic and dielectric subsystems. For instance, a sublattice of Jahn-Teller centers could be associated with the transport and relaxation of magnetism [102, 104]. Previous studies on titanium-doped hexaferrites identified such a sublattice [104], with structural relaxations occurring in a similar temperature interval and comparable activation energies. Furthermore, magnetic aftereffect measurements in hexaferrites provide evidence for $Fe^{2+}$ ion diffusion, which could impact transport through hopping mechanisms between $Fe^{2+}$ sites [14, 49, 102]. From experimental point of view adding pressure to already performed experiments should reveal whether there are structural features we can influence that enhance this effect. Additionally magnetoelectric measurements should be performed to see whether the correlation produces magnetoelectric effect, because within the scope of this hypothesis the magnetoelectric effect is expected.

## 5.3 Conclusion

Throughout this thesis we explored $Ba_xPb_{1-x}Fe_{12-y}Al_yO_{19}$ hexaferrites from several experimental points of view. We tracked how Al substitution modifies the magnetic properties in AC susceptibility, how does the dispersion of dielectric function change in dielectric spectroscopy, how the charge carriers move in dc-transport measurements and finally we probed the local structure using XAS and RIXS. All of the non-local experimental data point toward a new phenomenological effect which correlates behavior of magnetic and dielectric subsystems.

Interpretation of the experiments is done by introducing hypothesis of charged magnetic domain walls. These domain walls are proposed to pin on charged impurities and are subsequently screened by free carriers. This interpretation is supported by a detailed analysis of the magnetic and dielectric relaxation processes and dc transport measurements. Signatures of charge imbalance can be traced on the local level by XAS and RIXS, which support the interpretation. When the energies of the electromagnetic waves are considered, supporting evidence for the interpretation are found at nearly opposite ends of the spectrum—from low-energy radio waves to high-energy X-rays.

The primary outcome of this work concerns the activation energies associated with a priori unrelated subsystems, magnetic and dielectric. The observed alignment in activation energies suggests a coupling between magnetic and dielectric relaxation dynamics, which is linear with increase in magnetic disorder (Aluminum). This insight contributes to the broader understanding of how domain walls (charged) interact with their environment and are influenced by structural and electronic properties of the material.

The analysis and evaluation of these results have allowed us to assess alternative explanations and test the robustness of our hypothesis. While no direct magne-

toelectric coupling was observed under the applied experimental conditions, the consistency between the activation energies of a priori unconnected subsystems remains a significant finding. This correlation implies a shared underlying mechanism between the spin and charge regions in researched M-type hexaferrites.

# Appendix A

# Additional measurements

## A.1 Additional AC susceptibility

In the appendix, additional measurements of the AC susceptibility $\chi'$ and $\chi''$ for $Ba_{0.2}Pb_{0.8}Fe_{10.8}Al_{1.2}O_{19}$ and $Ba_{0.2}Pb_{0.8}Fe_{8.7}Al_{3.3}O_{19}$ are presented under varying experimental conditions. Measurements were performed with magnetic fields applied both perpendicular ($H \perp c$) and parallel ($H \parallel c$) to the $c$-axis. The frequency dependence was investigated over a range of $f = 7$ Hz to 777 Hz, and amplitude dependence was measured for AC magnetic field values from $H = 49$ mOe to 876 mOe across a temperature range of 50 K to 400 K.

The $H \perp c$ measurements serve as a complement to the results presented in the main text. Measurements of amplitude and frequency dependence (in $H \parallel c$) at high fields reveal additional features that demonstrate the complex response of the material. These features, which emerge under high fields, may be related to behavior observed at low fields; however, no clear interpretation is currently available. Further analysis is required to understand the underlying mechanisms responsible for these observations.

### A.1.1 Frequency dependence of $\perp$ c direction

Figure A.1 presents the real part of the AC susceptibility, $\chi'$, as a function of temperature $T$ for $Ba_{0.2}Pb_{0.8}Fe_{10.8}Al_{1.2}O_{19}$ under a magnetic field $H = 0.1$ Oe applied perpendicular to the $c$-direction ($H \perp c$). The measurements extend the results shown in Figure 4.4, demonstrating a frequency-dependent peak shift as the applied AC field frequency increases from 11 Hz to 111 Hz. The reduction in noise at higher frequencies results from the signal magnitude increasing with frequency, as described by Equation 3.11. The imaginary part of the susceptibility, $\chi''$, not shown here, remains effectively zero across the entire temperature range.

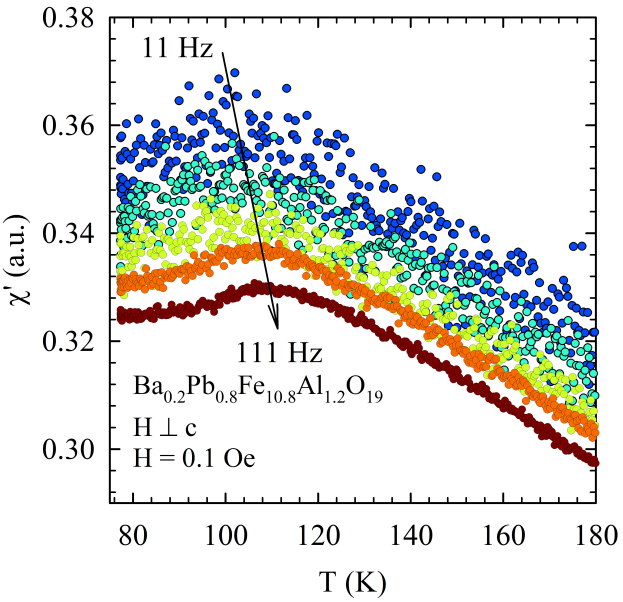


Figure A.1: The real part of the AC susceptibility, $\chi$' (a.u.), is plotted as a function of temperature $T$ for $Ba_{0.2}Pb_{0.8}Fe_{10.8}Al_{1.2}O_{19}$. The measurements were performed in a magnetic field $H = 0.1\,\mathrm{Oe}$, applied perpendicular to the $c$-direction ($H \perp c$). Different colored data points correspond to different frequencies of the applied AC magnetic field, ranging from 11 Hz (top curve) to 111 Hz (bottom curve). The arrow and the indicate the direction of increasing frequency, and also additionally serve as a guide for the eye of the peak shift with frequency.

### A.1.2 Amplitude dependence

Figure A.2 shows the temperature dependence of the real ($\chi'$) and imaginary ($\chi''$) components of the AC susceptibility for $Ba_{0.2}Pb_{0.8}Fe_{8.7}Al_{3.3}O_{19}$. Measurements were performed at an applied frequency $f = 111$ Hz under various magnetic fields $H \parallel c$, including 49 mOe (red), 282 mOe (orange), 452 mOe (light green), 594 mOe (cyan), 736 mOe (blue), and 876 mOe (purple), with the temperature range spanning from 77 K to 400 K. An increase in the applied AC field leads to a nonlinear response. At fields of 452 mOe and higher, noise begins to appear at low temperatures in both real and imaginary parts of the signal. This noise is attributed to the Barkhausen effect, which is discussed in Section 1.1.5. Furthermore, the imaginary part of the susceptibility, $\chi''$, appears to split into two distinct temperature peaks, while the real part, $\chi'$, consistently exhibits a single peak across all measurements.

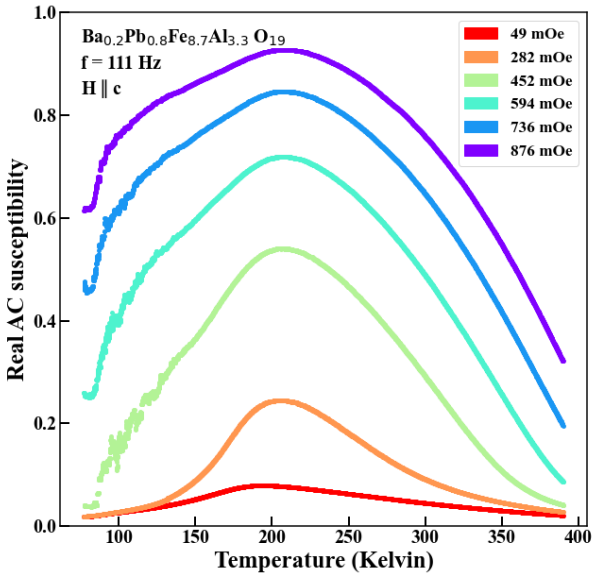


(a) Real part of AC susceptibility

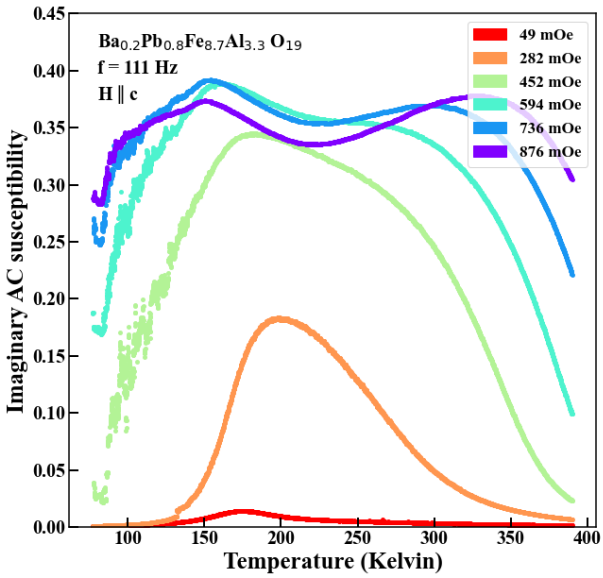


(b) Imaginary part of AC susceptibility

Figure A.2: Temperature dependence of the real (a) and imaginary (b) components of the AC susceptibility ($\chi''$ and $\chi'$) for $Ba_{0.2}Pb_{0.8}Fe_{8.7}Al_{3.3}O_{19}$. Measurements were conducted at a frequency $f = 111\,\text{Hz}$ under various applied magnetic fields ($H \parallel c$): 49 mOe (red), 282 mOe (orange), 452 mOe (light green), 594 mOe (cyan), 736 mOe (blue), and 876 mOe (purple). The temperature range extends from 50 K to 400 K, showing clear field-dependent peaks in both susceptibility components.

### A.1.3 High field frequency dependence

Figure A.3 shows the temperature dependence of the real ($\chi'$) and imaginary ($\chi''$) components of the AC susceptibility for $Ba_{0.2}Pb_{0.8}Fe_{8.7}Al_{3.3}O_{19}$ under an applied magnetic field of $H = 876$ mOe with $H \parallel c$. Measurements were conducted at three distinct frequencies: 7 Hz (red), 111 Hz (orange), and 777 Hz (light green), over a temperature range of 50 K to 400 K. Both susceptibility components exhibit frequency-dependent behavior. Specifically, $\chi'$ shows a single peak that shifts with increasing frequency, while $\chi''$ exhibits two peaks. The behavior of both real and imaginary part is complex and other than the Barkhausen effect, we do not try to interpret results.

A peculiar feature is observed in the real part of the susceptibility: at temperature of $\approx 150$ K, where the three frequency curves intersect, in other words where the dispersion disappears, a noisy part of the signal begins to appear for all frequencies. This behavior is not currently understood within the existing theoretical framework of the material. Further investigation is required to clarify the underlying physical mechanisms responsible for this observation.

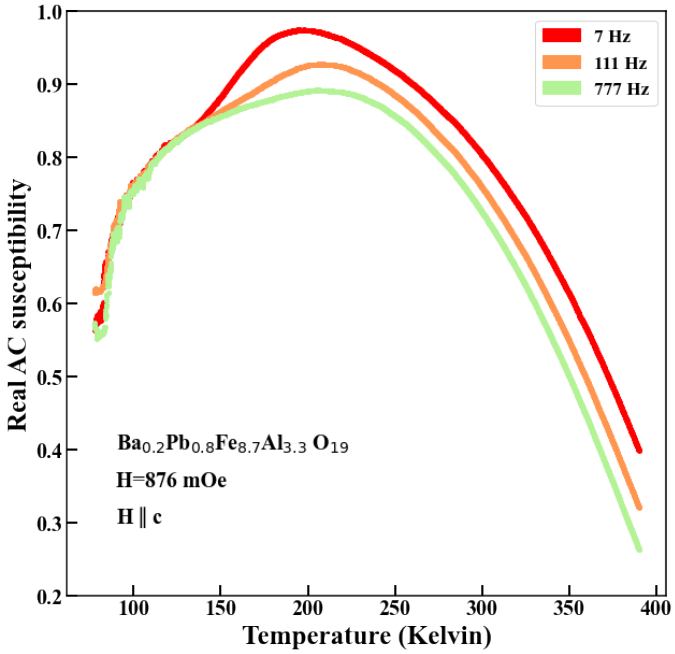


(a) Real part of AC susceptibility

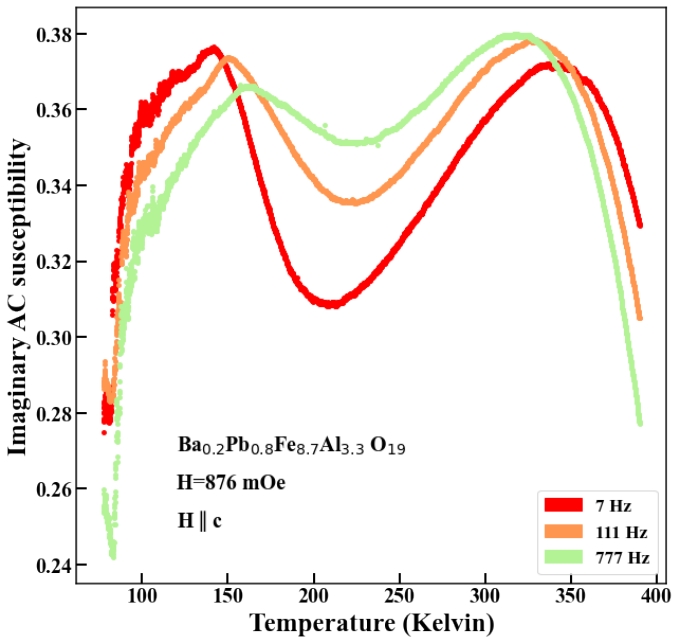


(b) Imaginary part of AC susceptibility

Figure A.3: Temperature dependence of the real (top) and imaginary (bottom) components of the AC susceptibility ($\chi'$ and $\chi''$) for $Ba_{0.2}Pb_{0.8}Fe_{8.7}Al_{3.3}O_{19}$ under an applied magnetic field of $H = 876\,\text{mOe}$ with $H \parallel c$. The measurements were conducted at three distinct frequencies:7 Hz(red), 111 Hz(orange), and 777 Hz(light green), over a temperature range of 50 K to 400 K. Both susceptibility components exhibit frequency-dependent features, indicating the dynamic response of the material.

## A.2 Additional RIXS

Additionally we performed four sets of measurements with circular right and circular left polarization. These measurements were performed under a magnetic field of 0.45 Tesla, with the incident X-ray photon energy set at 708 eV corresponding again to L3 edge, and at temperature of 300 Kelvin. Orientation of the magnetic field was along the c and -c crystallographic directions of the sample. Measurements are shown on Figure A.4. The measurements are separated by the orientation of the magnetic field. In both orientations dichroism is observed. This dichroism exhibits a reversal when the direction of the magnetic field is inverted. It is observable both in the low-energy peak at 1 eV and at 3 eV.

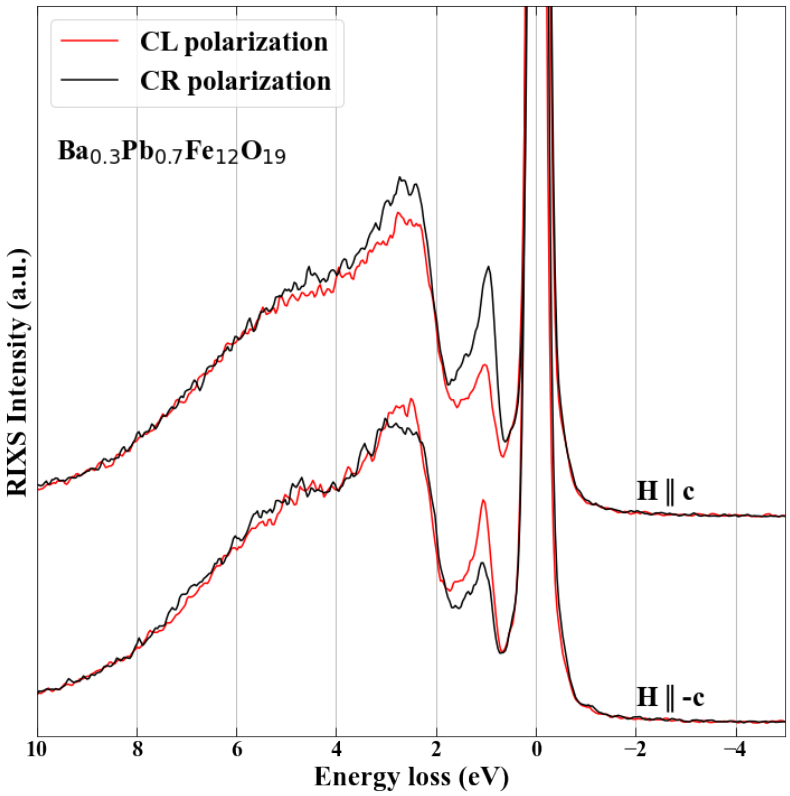


Figure A.4: Measurements of resonant inelastic x-ray scattering circular dichroism on sample $Ba_{0.3}Pb_{0.7}Fe_{12}O_{19}$. Wave vector of light is oriented in the c direction. Red line represents measurement made with left-hand circular polarization while black represents measurements with right-hand circular polarization. Two sets of measurements were done with magnetic field parallel to c-axis with amplitude of 0.45T.

The origin of the observed dichroism in the RIXS spectra can be interpreted in two ways. The primary explanation, which aligns with the main storyline discussed in earlier sections, connects the RIXS-MCD signal to changes occurring at the bi-pyramidal sites, particularly near domain walls. This interpretation, while

reasonable, remains somewhat qualitative. Alternatively, the origin of the dichroism could relate to findings reported by Miyawaki et al. [105], where the low-energy peak was attributed to spin-flip excitations. Specifically, in $\alpha$-$Fe_2O_3$, the low-energy peak A is primarily associated with spin-flip excitations involving transitions between localized $t_{2g}$ and $e_g$ orbitals of $Fe^3+$ ions. Based on ab initio charge-transfer multiplet calculations and experimental observations, this peak corresponds to $t_{2g} \rightarrow e_g$ transitions. Notably, in the case of $\alpha$-$Fe_2O_3$, the absence of a RIXS-MCD signal is expected due to its antiferromagnetic nature, which contrasts with the ferromagnetic or ferrimagnetic conditions necessary for dichroism to emerge.

Both interpretations remain qualitative at this stage. To resolve this issue, it is essential to study crystals free of deficiencies or substitutions, as such imperfections introduce changes in both the crystal and magnetic structures that are difficult to account in computation (ab-intio, crystal field ...), which is already non-trivial for RIXS-MCD. Nevertheless, the mere existence of RIXS-MCD in a $d - d$ transition within hexaferrites is significant and may prove useful for future investigations into their electronic and magnetic properties.

# Bibliography


[1] Robert C. Pullar. "Hexagonal ferrites: A review of the synthesis, properties and applications of hexaferrite ceramics". *Progress in Materials Science* 57.7 (2012), pp. 1191–1334. ISSN: 0079-6425. DOI: https://doi.org/10.1016/j.pmatsci.2012.04.001. URL: https://www.sciencedirect.com/science/article/pii/S0079642512000369.

[2] Tianyu Li et al. "Insights into Strain Engineering: From Ferroelectrics to Related Functional Materials and Beyond". *Chemical Reviews* 124.11 (2024), pp. 7045–7105. DOI: 10.1021/acs.chemrev.3c00767.

[3] Stephan Krohns and Peter Lunkenheimer. "Ferroelectric polarization in multiferroics". *Physical Sciences Reviews* 4.9 (July 2019). DOI: 10.1515/psr-2019-0015. URL: https://doi.org/10.1515/psr-2019-0015.

[4] Tsuyoshi Kimura. "Magnetoelectric Hexaferrites". *Annual Review of Condensed Matter Physics* 3.1 (Mar. 2012), pp. 93–110. ISSN: 1947-5462. DOI: 10.1146/annurev-conmatphys-020911-125101. URL: http://dx.doi.org/10.1146/annurev-conmatphys-020911-125101.

[5] J.-P. Rivera. "A short review of the magnetoelectric effect and related experimental techniques on single phase (multi-) ferroics". *The European Physical Journal B* 71.3 (Oct. 2009), pp. 299–313. ISSN: 1434-6036. DOI: 10.1140/epjb/e2009-00336-7. URL: http://dx.doi.org/10.1140/epjb/e2009-00336-7.

[6] Zi-lin Yuan et al. "A review of ultra-thin ferroelectric films". *Journal of Physics: Condensed Matter* 33.40 (July 2021), p. 403003. DOI: 10.1088/1361-648X/ac145c. URL: https://doi.org/10.1088/1361-648X/ac145c.

[7] Liudmila N Alyabyeva et al. "Influence of chemical substitution on broadband dielectric response of barium-lead M-type hexaferrite". *New Journal of Physics* 21.6 (June 2019), p. 063016. DOI: 10.1088/1367-2630/ab2476. URL: https://doi.org/10.1088/1367-2630/ab2476.

[8] P. S. Wang and H. J. Xiang. "Room-Temperature Ferrimagnet with Frustrated Antiferroelectricity: Promising Candidate Toward Multiple-State Memory". *Phys. Rev. X* 4 (1 Mar. 2014), p. 011035. DOI: 10.1103/PhysRevX.4.011035. URL: https://link.aps.org/doi/10.1103/PhysRevX.4.011035.

[9] S. Blundell. *Magnetism in Condensed Matter*. Oxford Master Series in Condensed Matter Physics. OUP Oxford, 2001. ISBN: 9780191586644. URL: https://books.google.hr/books?id=zP9QEAAAQBAJ.

[10] Charles Kittel. "Physical Theory of Ferromagnetic Domains". *Reviews of Modern Physics* 21.4 (Oct. 1949), pp. 541–583. ISSN: 0034-6861. DOI: 10.1103/revmodphys.21.541. URL: http://dx.doi.org/10.1103/RevModPhys.21.541.

[11] N.A. Spaldin. *Magnetic Materials: Fundamentals and Applications*. Cambridge University Press, 2010. ISBN: 9781139491556. URL: https://books.google.hr/books?id=vnrOE8pQUgIC.

[12] J.B. Goodenough. *Magnetism and the Chemical Bond*. Inorganic Chemistry Section / Interscience monographs on chemistry. Interscience Publishers, 1963. URL: https://books.google.hr/books?id=ljtRAAAAMAAJ.

[13] A. Isalgu et al. "Exchange interactions in $BaFe_{12}O_{19}$". *Applied Physics A Solids and Surfaces* 39.3 (Mar. 1986), pp. 221–225. ISSN: 1432-0630. DOI: 10.1007/bf00620738. URL: http://dx.doi.org/10.1007/BF00620738.

[14] E.P. Wohlfarth and K.H.J. Buschow. *Ferromagnetic Materials: A Handbook on the Properties of Magnetically Ordered Substances*. Ferromagnetic Materials: A Handbook on the Properties of Magnetically Ordered Substances s. 4. North-Holland Publishing Company, 1988. ISBN: 9780444871060. URL: https://books.google.hr/books?id=JN7vAAAAMAAJ.

[15] B.D. Cullity and C.D. Graham. *Introduction to Magnetic Materials*. Wiley, 2011. ISBN: 9781118211496. URL: https://books.google.hr/books?id=fh_F0G9KuSgC.

[16] Pierre Weiss. "L'hypothèse du champ moléculaire et la propriété ferromagnétique". *Journal de Physique Théorique et Appliquée* 6.1 (1907), pp. 661–690. ISSN: 0368-3893. DOI: 10.1051/jphystap:019070060066100. URL: http://dx.doi.org/10.1051/jphystap:019070060066100.

[17] Jean-Michel Lasry and Pierre-Louis Lions. "Mean field games". *Japanese Journal of Mathematics* 2.1 (Mar. 2007), pp. 229–260. ISSN: 1861-3624. DOI: 10.1007/s11537-007-0657-8. URL: http://dx.doi.org/10.1007/s11537-007-0657-8.

[18] Jean-Yves Le Boudec, David McDonald, and Jochen Mundinger. "A Generic Mean Field Convergence Result for Systems of Interacting Objects". *Fourth International Conference on the Quantitative Evaluation of Systems (QEST 2007)*. 2007, pp. 3–18. DOI: 10.1109/QEST.2007.8.

[19] C. Kittel. *Kittel's Introduction to Solid State Physics*. Wiley, 2018. ISBN: 9781119456186. URL: https://books.google.hr/books?id=WHP2DwAAQBAJ.

[20] R. Kubo et al. *Statistical Mechanics*. North-Holland Personal Library. Elsevier Science, 1990. ISBN: 9780444871039. URL: https://books.google.hr/books?id=MNHmzgEACAAJ.

[21] Ž. Rapljenović. *Antiferomagnetski uređeno stanje u sustavu spinskih tetramera $SeCuO_3$(Diplomski rad)*. https://urn.nsk.hr/urn:nbn:hr:217:374556. Zagreb: Sveučilište u Zagrebu, Prirodoslovno-matematički fakultet, 2017.

[22] K Dey et al. "Magnetic phase diagram and magnetoelastic coupling of $NiTiO_3$". en. *Phys. Rev. B.* 101.19 (May 2020).

[23] A. Hubert and R. Schäfer. *Magnetic Domains: The Analysis of Magnetic Microstructures*. Springer, 1998. ISBN: 9783540641087. URL: https://books.google.hr/books?id=pBE42lLYs-MC.

[24] L. LANDAU and E. LIFSHITZ. "On the theory of the dispersion of magnetic permeability in ferromagnetic bodies". *Perspectives in Theoretical Physics*. Elsevier, 1992, pp. 51–65. ISBN: 9780080363646. DOI: 10.1016/b978-0-08-036364-6.50008-9. URL: http://dx.doi.org/10.1016/B978-0-08-036364-6.50008-9.

[25] P J Metaxas et al. "Creep and flow regimes of magnetic domain-wall motion in ultrathin Pt/Co/Pt films with perpendicular anisotropy". en. *Phys. Rev. Lett.* 99.21 (Nov. 2007), p. 217208.

[26] Wolfgang Haase and Stanislaw Wróbel, eds. *Relaxation Phenomena*. Springer Berlin Heidelberg, 2003. DOI: 10.1007/978-3-662-09747-2. URL: https://doi.org/10.1007/978-3-662-09747-2.

[27] M. Bałanda. "AC Susceptibility Studies of Phase Transitions and Magnetic Relaxation: Conventional, Molecular and Low-Dimensional Magnets". *Acta Physica Polonica A* 124.6 (Dec. 2013), pp. 964–976. DOI: 10.12693/aphyspola.124.964. URL: https://doi.org/10.12693/aphyspola.124.964.

[28] C V Topping and S J Blundell. "A.C. susceptibility as a probe of low-frequency magnetic dynamics". *Journal of Physics: Condensed Matter* 31.1 (Nov. 2018), p. 013001. DOI: 10.1088/1361-648x/aaed96. URL: https://doi.org/10.1088/1361-648x/aaed96.

[29] A.H. Morrish. *The Physical Principles of Magnetism*. Wiley series on the science and technology of materials. R. E. Krieger Publishing Company, 1980. ISBN: 9780882756707. URL: https://books.google.hr/books?id=ZjUbAQAAIAAJ.

[30] Terunobu Miyazaki and Hanmin Jin. *The Physics of Ferromagnetism*. Springer Berlin Heidelberg, 2012. ISBN: 9783642255830. DOI: 10.1007/978-3-642-25583-0. URL: http://dx.doi.org/10.1007/978-3-642-25583-0.

[31] D. C. Jiles. "Dynamics of domain magnetization and the barkhausen effect". *Czechoslovak Journal of Physics* 50.8 (2000), pp. 893–924. ISSN: 0011-4626. DOI: 10.1023/a:1022846128461. URL: http://dx.doi.org/10.1023/A:1022846128461.

[32] R Hornreich and S Shtrikman. "Statistical mechanics and origin of the magnetoelectric effect in$Cr_2O_3$". *Phys. Rev.* 161.2 (Sept. 1967), pp. 506–512.

[33] Manfred Fiebig. "Revival of the magnetoelectric effect". *Journal of Physics D: Applied Physics* 38.8 (Apr. 2005), R123. DOI: 10.1088/0022-3727/38/8/R01. URL: https://doi.org/10.1088/0022-3727/38/8/R01.

[34] Friedrich Kremer and Andreas Schönhals. *Broadband Dielectric Spectroscopy*. Springer Berlin Heidelberg, 2003. ISBN: 9783642561207. DOI: 10.1007/978-3-642-56120-7. URL: http://dx.doi.org/10.1007/978-3-642-56120-7.

[35] L.P. Gor'kov and G. Grüner. *Charge Density Waves in Solids*. Modern Problems in Condensed Matter Sciences. North Holland, 2012. ISBN: 9780444600738. URL: https://books.google.hr/books?id=3cu2QIeL0J4C.

[36] P. B. Littlewood. "Screened dielectric response of sliding charge-density waves". *Physical Review B* 36.6 (Aug. 1987), pp. 3108–3116. ISSN: 0163-1829. DOI: 10.1103/physrevb.36.3108. URL: http://dx.doi.org/10.1103/PhysRevB.36.3108.

[37] Roberto Garrappa, Francesco Mainardi, and Guido Maione. "Models of Dielectric Relaxation Based on Completely Monotone Functions". *Fractional Calculus and Applied Analysis* 19.5 (Oct. 2016), pp. 1105–1160. ISSN: 1314-2224. DOI: 10.1515/fca-2016-0060. URL: http://dx.doi.org/10.1515/fca-2016-0060.

[38] M. Samet et al. "Electrode polarization vs. Maxwell-Wagner-Sillars interfacial polarization in dielectric spectra of materials: Characteristic frequencies and scaling laws". *The Journal of Chemical Physics* 142.19 (May 2015). ISSN: 1089-7690. DOI: 10.1063/1.4919877. URL: http://dx.doi.org/10.1063/1.4919877.

[39] P. Lunkenheimer et al. "Origin of apparent colossal dielectric constants". *Physical Review B* 66.5 (Aug. 2002). ISSN: 1095-3795. DOI: 10.1103/physrevb.66.052105. URL: http://dx.doi.org/10.1103/PhysRevB.66.052105.

[40] Tomislav Ivek. "Charge orderings in strongly correlated systems". PhD thesis. Department of Physics, Faculty of Science, University of Zagreb, 2011.

[41] F. de Groot and A. Kotani. *Core Level Spectroscopy of Solids*. Advances in Condensed Matter Science. CRC Press, 2008. ISBN: 9781420008425. URL: https://books.google.hr/books?id=HGHzu66i1yoC.

[42] P. Zimmermann. "Crystal field multiplet calculations and the Magnetic circular dichroism of $CrO_2$ in Resonant inelastic Xray scattering". English. Doctoral thesis 1 (Research UU / Graduation UU). Universiteit Utrecht, May 2018. ISBN: 978-94-6233-930-9.

[43] Frank de Groot. "High-Resolution X-ray Emission and X-ray Absorption Spectroscopy". *Chemical Reviews* 101.6 (May 2001), pp. 1779–1808. DOI: 10.1021/cr9900681. URL: https://doi.org/10.1021/cr9900681.

[44] Muhammad Umar Shafi et al. "A review on advances in synthesis, composition, structural and microwave properties of U-type hexaferrites nanoparticles". *Journal of Materials Science* 59.35 (Sept. 2024), pp. 16383–16410. ISSN: 1573-4803. DOI: 10.1007/s10853-024-10180-y. URL: http://dx.doi.org/10.1007/s10853-024-10180-y.

[45] J. J. Went et al. "Ferroxdure, a class of new permanent magnet materials". *Philips Technical Review* 13.7 (Jan. 1952), pp. 194–208. URL: https://pearl-hifi.com/06_Lit_Archive/02_PEARL_Arch/Vol_16/Sec_53/Philips_Tech_Review/PTechReview-13-1951_52-194.pdf.

[46] Anubhav Jain et al. "Commentary: The Materials Project: A materials genome approach to accelerating materials innovation". *APL Materials* 1.1 (July 2013), p. 011002. DOI: 10.1063/1.4812323. URL: https://doi.org/10.1063/1.4812323.

[47] Koichi Momma and Fujio Izumi. "VESTA 3 for three-dimensional visualization of crystal, volumetric and morphology data". *Journal of Applied Crystallography* 44 (2011), pp. 1272–1276. DOI: 10.1107/S0021889811038970. URL: https://doi.org/10.1107/S0021889811038970.

[48] Cesar de Julian Fernandez et al. "Topical Review: Progress and Prospects of Hard Hexaferrites for Permanent Magnet Applications". *Journal of Physics D: Applied Physics* (Dec. 2020). DOI: 10.1088/1361-6463/abd272. URL: https://doi.org/10.1088/1361-6463/abd272.

[49] K. Závêta. "Anisotropy of the Electrical Conductivity of Ferrites with the Magnetoplumbite Structure". *physica status solidi (b)* 3.11 (1963), pp. 2111–2118. DOI: https://doi.org/10.1002/pssb.19630031115. URL: https://onlinelibrary.wiley.com/doi/abs/10.1002/pssb.19630031115.

[50] A. Collomb, P. Wolfers, and X. Obradors. "Neutron diffraction studies of some hexagonal ferrites: $BaFe_{12}O_{19}$, $BaMg_2$-W and $BaCo_2$-W". *Journal of Magnetism and Magnetic Materials* 62.1 (Nov. 1986), pp. 57–67. DOI: 10.1016/0304-8853(86)90734-1. URL: https://doi.org/10.1016/0304-8853(86)90734-1.

[51] S. P. Marshall and J. B. Sokoloff. "Phonon spectrum for barium ferrite". *Physical Review B* 44.2 (July 1991), pp. 619–627. DOI: 10.1103/physrevb.44.619. URL: https://doi.org/10.1103/physrevb.44.619.

[52] Shi-Peng Shen et al. "Quantum electric-dipole liquid on a triangular lattice". *Nature Communications* 7.1 (Feb. 2016). DOI: 10.1038/ncomms10569. URL: https://doi.org/10.1038/ncomms10569.

[53] Shi-Peng Shen et al. "Magnetic-ion-induced displacive electric polarization in $FeO_5$ bipyramidal units of $(Ba, Sr)Fe_{12}O_{19}$ hexaferrites". *Phys. Rev. B* 90 (18 Nov. 2014), p. 180404. DOI: 10.1103/PhysRevB.90.180404. URL: https://link.aps.org/doi/10.1103/PhysRevB.90.180404.

[54] L N Alyabyeva et al. "Lead-substituted barium hexaferrite for tunable terahertz optoelectronics". en. *NPG Asia Mater.* 13.1 (Dec. 2021).

[55] Denis A. Vinnik. "Resistive furnace for single crystals growth". *Butlerov Communications* 39.9 (2014), pp. 153–154.

[56] Asmaa Ahmed et al. "Terahertz-infrared electrodynamics of single-crystalline $Ba_{0.2}Pb_{0.8}Al_{1.2}Fe_{10.8}O_{19}$ M-type hexaferrite". *Journal of Alloys and Compounds* 836 (Sept. 2020), p. 155462. DOI: 10.1016/j.jallcom.2020.155462. URL: https://doi.org/10.1016/j.jallcom.2020.155462.

[57] Asmaa Ahmed et al. "Terahertz-infrared dielectric properties of lead-aluminum double-cation substituted single-crystalline barium hexaferrite". *Journal of Alloys and Compounds* 898 (Mar. 2022), p. 162761. DOI: 10.1016/j.jallcom.2021.162761. URL: https://doi.org/10.1016/j.jallcom.2021.162761.

[58] D. Drobac et al. "The role of lock-in phase setting in ac susceptibility measurement". *Review of Scientific Instruments* 84.5 (May 2013), p. 054708. DOI: 10.1063/1.4807752. URL: https://doi.org/10.1063/1.4807752.

[59] David J. Griffiths. *Introduction to Electrodynamics*. Cambridge University Press, June 2017. DOI: 10.1017/9781108333511. URL: https://doi.org/10.1017/9781108333511.

[60] *Cryobind*. http://www.cryobind.com/. (Accessed on 12/31/2021).

[61] *Keithley Ultra-sensitive Current Sources Series 6200 | Tektronix*. https://www.tek.com/en/products/keithley/low-level-sensitive-and-specialty-instruments/series-6200. (Accessed on 01/05/2022).

[62] *7265 Dual Phase DSP Lock-in Amplifier | Signal Recovery*. https://www.ameteksi.com/support-center/legacy-products/signal-recovery-legacy/lock-in-amplifier-legacy/7265-dual-phase-lock-in-amplifier. (Accessed on 01/05/2022).

[63] C. Kittel and J.K. Galt. "Ferromagnetic Domain Theory". *Solid State Physics*. Elsevier, 1956, pp. 437–564. DOI: 10.1016/s0081-1947(08)60136-8. URL: https://doi.org/10.1016/s0081-1947(08)60136-8.

[64] H.A. Groenendijk, A.J. van Duyneveldt, and R.D. Willett. "Experimental study of the effect of domains on the A.C. susceptibility of the weak ferromagnet $(C_3H_7NH_3)_2MnCl_4$". *Physica 101B* 101.3 (Sept. 1980), pp. 320–328. DOI: 10.1016/0378-4363(80)90031-5. URL: https://doi.org/10.1016/0378-4363(80)90031-5.

[65] William Fuller Brown. "Thermal Fluctuations of a Single-Domain Particle". *Physical Review* 130.5 (June 1963), pp. 1677–1686. DOI: 10.1103/physrev.130.1677. URL: https://doi.org/10.1103/physrev.130.1677.

[66] J.F. Nye. *Physical Properties of Crystals: Their Representation by Tensors and Matrices*. Oxford science publications. Clarendon Press, 1985. ISBN: 9780198511656. URL: https://books.google.hr/books?id=ugwql-uVB44C.

[67] H. C. Montgomery. "Method for Measuring Electrical Resistivity of Anisotropic Materials". *Journal of Applied Physics* 42.7 (June 1971), pp. 2971–2975. ISSN: 1089-7550. DOI: 10.1063/1.1660656. URL: http://dx.doi.org/10.1063/1.1660656.

[68] Nevill Francis Mott and Edward Arthur Davis. *Electronic processes in non-crystalline materials*. Oxford Classic Texts in the Physical Sciences. London, England: Oxford University Press, Feb. 2012.

[69] Shklovskii, B.I. and Efros, A.L. *Electronic Properties of Doped Semiconductors*. Solid-State Sciences Series. Springer-Verlag, 1984. ISBN: 9783540129950. URL: https://books.google.hr/books?id=o8PvAAAAMAAJ.

[70] https://www.keysight.com/us/en/assets/9018-05655/user-manuals/9018-05655.pdf?success=true. [Accessed 16-05-2025].

[71] https://www.keysight.com/us/en/product/E4980AL/precision-lcr-meter-20-hz-300-khz-500-khz-1-mhz.html. [Accessed 27-11-2024].

[72] https://www.keysight.com/us/en/product/4294A/precision-impedance-analyzer-40-hz-to-110-mhz.html. [Accessed 27-11-2024].

[73] https://www.keysight.com/us/en/product/4284A/precision-lcr-meter-20-hz-to-1-mhz.html. [Accessed 27-11-2024].

[74] E. Barsoukov and J.R. Macdonald. *Impedance Spectroscopy: Theory, Experiment, and Applications*. Wiley, 2005. ISBN: 9780471716228. URL: https://books.google.hr/books?id=8hNkOWO_DLwC.

[75] Keysight. *Impedance Measurement Handbook — keysight.com*. https://www.keysight.com/us/en/assets/7018-06840/application-notes/5950-3000.pdf. [Accessed 24-01-2025].

[76] https://www.keysight.com/us/en/assets/9018-05655/user-manuals/9018-05655.pdf?success=true. [Accessed 22-01-2025].

[77] F. Schrettle et al. "Switching the ferroelectric polarization in the $S = 1/2$ chain cuprate $LiCuVO_4$ by external magnetic fields". *Phys. Rev. B* 77 (14 Apr. 2008), p. 144101. DOI: 10.1103/PhysRevB.77.144101. URL: https://link.aps.org/doi/10.1103/PhysRevB.77.144101.

[78] Peter Lunkenheimer et al. "Multiferroicity in an organic charge-transfer salt that is suggestive of electric-dipole-driven magnetism". *Nature Materials* 11.9 (Aug. 2012), pp. 755–758. DOI: 10.1038/nmat3400. URL: https://doi.org/10.1038/nmat3400.

[79] Surya M. Gupta et al. "A comparative dielectric relaxation study of PMN–PT and PMN–PZ ceramics using impedance spectroscopy". *Materials Science and Engineering: B* 120.1 (2005). The 8th International Symposium on Ferroic Domains (ISFD-8, 2004), pp. 194–198. ISSN: 0921-5107. DOI: https://doi.org/10.1016/j.mseb.2005.02.013. URL: https://www.sciencedirect.com/science/article/pii/S0921510705001108.

[80] F. Schrettle et al. "Relaxor ferroelectricity and the freezing of short-range polar order in magnetite". *Phys. Rev. B* 83 (19 May 2011), p. 195109. DOI: 10.1103/PhysRevB.83.195109. URL: https://link.aps.org/doi/10.1103/PhysRevB.83.195109.

[81] Anna Palau et al. "Encoding Magnetic States in Monopole-Like Configurations Using Superconducting Dots". *Advanced Science* 3.11 (Sept. 2016), p. 1600207. DOI: 10.1002/advs.201600207. URL: https://doi.org/10.1002/advs.201600207.

[82] *Sextants*. URL: https://www.wayforlight.eu/beamline/20926.

[83] M Sacchi et al. "The SEXTANTS beamline at SOLEIL: a new facility for elastic, inelastic and coherent scattering of soft X-rays". *Journal of Physics: Conference Series* 425.7 (Mar. 2013), p. 072018. DOI: 10.1088/1742-6596/425/7/072018. URL: https://doi.org/10.1088/1742-6596/425/7/072018.

[84] M. Abbate et al. "Probing depth of soft x-ray absorption spectroscopy measured in total-electron-yield mode". *Surface and Interface Analysis* 18.1 (Jan. 1992), pp. 65–69. DOI: 10.1002/sia.740180111. URL: https://doi.org/10.1002/sia.740180111.

[85] Reshmi Kurian et al. "Intrinsic deviations in fluorescence yield detected x-ray absorption spectroscopy: the case of the transition metal L2, 3 edges". *Journal of Physics: Condensed Matter* 24.45 (Oct. 2012), p. 452201. DOI: 10.1088/0953-8984/24/45/452201. URL: https://doi.org/10.1088/0953-8984/24/45/452201.

[86] Akio Kotani and Shik Shin. "Resonant inelastic x-ray scattering spectra for electrons in solids". *Reviews of Modern Physics* 73.1 (Feb. 2001), pp. 203–246. DOI: 10.1103/revmodphys.73.203. URL: https://doi.org/10.1103/revmodphys.73.203.

[87] Luuk J. P. Ament et al. "Resonant inelastic x-ray scattering studies of elementary excitations". *Reviews of Modern Physics* 83.2 (June 2011), pp. 705–767. DOI: 10.1103/revmodphys.83.705. URL: https://doi.org/10.1103/revmodphys.83.705.

[88] Sorin G. Chiuzbăian et al. "Design and performance of AERHA, a high acceptance high resolution soft x-ray spectrometer". *Review of Scientific Instruments* 85.4 (Apr. 2014). ISSN: 1089-7623. DOI: 10.1063/1.4871362. URL: http://dx.doi.org/10.1063/1.4871362.

[89] Marius Retegan. *Crispy: v0.8.0*. 2024. DOI: 10.5281/zenodo.1008184. URL: https://dx.doi.org/10.5281/zenodo.1008184.

[90] Maurits W. Haverkort et al. *Quanty - a quantum many body script language — Quanty*. [Online; accessed 27-January-2025]. URL: https://www.quanty.org/doku.php?id=index.html&rev=1560456998.

[91] O Bunău and Y Joly. "Self-consistent aspects of x-ray absorption calculations". *Journal of Physics: Condensed Matter* 21.34 (Aug. 2009), p. 345501. ISSN: 1361-648X. DOI: 10.1088/0953-8984/21/34/345501. URL: http://dx.doi.org/10.1088/0953-8984/21/34/345501.

[92] *Team - The FDMNES project — fdmnes.neel.cnrs.fr*. https://fdmnes.neel.cnrs.fr/team/. [Accessed 27-01-2025].

[93] G. D. Soria et al. "Strontium hexaferrite platelets: a comprehensive soft X-ray absorption and Mössbauer spectroscopy study". *Scientific Reports* 9.1 (Aug. 2019). ISSN: 2045-2322. DOI: 10.1038/s41598-019-48010-w. URL: http://dx.doi.org/10.1038/s41598-019-48010-w.

[94] J. E. Beevers et al. "Enhanced magnetoelectric effect in M-type hexaferrites by Co substitution into trigonal bi-pyramidal sites". *Applied Physics Letters* 112.8 (Feb. 2018). ISSN: 1077-3118. DOI: 10.1063/1.5017683. URL: http://dx.doi.org/10.1063/1.5017683.

[95] *Keithley Nanovoltmeter Model 2182A — tek.com*. https://www.tek.com/en/products/keithley/low-level-sensitive-and-specialty-instruments/nanovoltmeter-model-2182a. [Accessed 09-12-2024].

[96] *testequipmenthq.com*. https://www.testequipmenthq.com/datasheets/KEITHLEY-487-Datasheet.pdf. [Accessed 09-12-2024].

[97] I. T. Jolliffe. *Principal Component Analysis*. Springer-Verlag, 2002. ISBN: 0387954422. DOI: 10.1007/b98835. URL: http://dx.doi.org/10.1007/b98835.

[98] Pierre Monceau. "Electronic crystals: an experimental overview". *Advances in Physics* 61.4 (Aug. 2012), pp. 325–581. ISSN: 1460-6976. DOI: 10.1080/00018732.2012.719674. URL: http://dx.doi.org/10.1080/00018732.2012.719674.

[99] M. Prester et al. "Slow magnetic dynamics and hysteresis loops of the bulk ferromagnet $Co_7(TeO_3)_4Br_6$". *Physical Review B* 84.6 (Aug. 2011). DOI: 10.1103/physrevb.84.064441. URL: https://doi.org/10.1103/physrevb.84.064441.

[100] S Tomić et al. "Magnetic ordering and charge dynamics in $\kappa$-(BEDT-TTF)$_2$Cu[N(CN)$_2$]Cl". *Journal of Physics: Condensed Matter* 25.43 (Oct. 2013), p. 436004. ISSN: 1361-648X. DOI: 10.1088/0953-8984/25/43/436004. URL: http://dx.doi.org/10.1088/0953-8984/25/43/436004.

[101] M. Pinterić et al. "Magnetic anisotropy and low-frequency dielectric response of weak ferromagnetic phase in $\kappa$-(BEDT-TTF)$_2$Cu[N(CN)$_2$]Cl, where BEDT-TTF is Bis(ethylenedithio)tetrathiafulvalene". *The European Physical Journal B* 11.2 (Sept. 1999), pp. 217–225. ISSN: 1434-6036. DOI: 10.1007/bf03219166. URL: http://dx.doi.org/10.1007/BF03219166.

[102] Željko Rapljenović et al. "Persisting correlation between electrical transport and magnetic dynamics in M-type hexaferrites". *Journal of Alloys and Compounds* 895 (2022), p. 162660. ISSN: 0925-8388. DOI: https://doi.org/10.1016/j.jallcom.2021.162660. URL: https://www.sciencedirect.com/science/article/pii/S0925838821040706.

[103] M. Pinterić et al. "Anisotropic charge dynamics in the quantum spin-liquid candidate $\kappa$-(BEDT-TTF)$_2$Cu$_2$(CN)$_3$". *Physical Review B* 90.19 (Nov. 2014). ISSN: 1550-235X. DOI: 10.1103/physrevb.90.195139. URL: http://dx.doi.org/10.1103/PhysRevB.90.195139.

[104] V. V. Gudkov et al. "Sub-lattice of Jahn-Teller centers in hexaferrite crystal". *Scientific Reports* 10.1 (Apr. 2020). ISSN: 2045-2322. DOI: 10.1038/s41598-020-63915-7. URL: http://dx.doi.org/10.1038/s41598-020-63915-7.

[105] Jun Miyawaki et al. "Dzyaloshinskii-Moriya interaction in $\alpha$-Fe$_2$O$_3$ measured by magnetic circular dichroism in resonant inelastic soft x-ray scattering". *Physical Review B* 96.21 (Dec. 2017). ISSN: 2469-9969. DOI: 10.1103/physrevb.96.214420. URL: http://dx.doi.org/10.1103/PhysRevB.96.214420.

# List of Figures

# List of Tables